Title

Synaptic heterogeneity and the underlying molecular mechanisms at the Drosophila neuromuscular junction.

Permalink

https://escholarship.org/uc/item/29s2t2wc

Author

Bakshinska, Dariya

Publication Date

2023

Synaptic heterogeneity and the underlying molecular mechanisms at the *Drosophila* neuromuscular junction.

by

Dariya Bakshinska

A dissertation submitted in partial satisfaction of the

requirements for the degree of

Doctor of Philosophy

in

Neuroscience

in the

Graduate Division of the

University of California, Berkeley

Committee in charge:

Professor Ehud Isacoff, Chair
Professor Kristin Scott
Professor Marla B. Feller
Professor Daniel E. Feldman

Summer 2023

Abstract

Synaptic heterogeneity and the underlying molecular mechanisms at the *Drosophila* neuromuscular junction.

by

Dariya Bakshinska

Doctor of Philosophy in Neuroscience

University of California, Berkeley

Professor Ehud Isacoff, Chair

Synapses are the fundamental units of communication in the nervous system and reliable synaptic transmission is central to key nervous system processes such as learning, memory, and sensory adaptation. Moreover, due to dysfunctions at the synapse, many neurological diseases may develop. While electrophysiological studies of synaptic transmission have been around for a long time, only the recent development of optical quantal analysis (OQA) tools has made possible to correlate morphological and structural elements to transmission properties of individual synapses. Studies using OQA have revealed a much larger diversity in synaptic transmission, even among neighboring synapses, than was previously thought. The advent of higher-resolution OQA, such as the one developed in **Chapter 2** of this thesis, called “QuaSOR”, and super-resolution structural imaging methods opens up an exciting frontier of being able to investigate how neural activity shapes (and is shaped by) synaptic diversity, what are the molecular determinants and mechanisms the set this diversity, and how do these molecular determinants shape synaptic diversity.

By using OQA, we’ve shown that synaptic diversity, as measured by difference in synaptic strength (i.e., probability of action potential evoked transmission; *Pr*) is extremely heterogeneous (*Pr*: 0.01–0.62) within a single neuron synapsing onto a single target cell. This high degree of heterogeneity leads us to the central hypothesis of my thesis which is that synaptic strength is set by a very precise, local distribution of key proteins. To test this hypothesis I used the model glutamatergic synapse–*Drosophila melanogaster* larval neuromuscular junction (NMJ)– where I will investigated hundreds of synapses in parallel, *in vivo*, and addressed synaptic heterogeneity from both functional and structural perspectives at single synapse resolution (50-100nm).

In **Chapter 2** of this thesis, using a combination of QuaSOR and super-resolution structural imaging methods, we found that essential active zone (AZ) proteins such as Bruchpilot (Brp) and the Ca^{2+}-channel Cacophony (Cac) vary greatly among synapses and can explain ~31% of the diversity that we observe in basal P_r. Moreover, when investigating complexin, which acts as a break on release, we found that it suppresses both spontaneous and evoked release but in different ways. Taking the functional-structural tools developed in Chapter 2, I then wanted to ask how the neuromodulator octopamine, which is released from type II motor neurons (MNs) impacts synaptic release at type I MNs. In **Chapter 3**, I was able to show that OA affects release at type I MN in an input-specific manner (increasing release at type Ib MNs but having no effect at type Is MNs). Then, combining the QuaSOR method with structural imaging, I was able to show that the effect of modulation by OA on a single-synapse level is at least partially due to the amount of Unc13A at the synapse and interestingly, is dependent on the PLC pathway.

To the brave, resilient, and fearless people of Ukraine.

Acknowledgements

I have many people to thank for completing this dissertation. As they say, “It takes a village” and my story starts in the Ukrainian village of Pidhorodyshche (Lviv region) where my maternal grandparents lived. My grandfather Stepan Pankiv taught me to be curious from a very young age. He had an incredibly difficult life due to Stalin’s repressive policies towards Ukraine and many of his family members were killed by the NKVD (Soviet police) simply for being Ukrainian. He quite frequently risked his life to stand up for our Ukrainian heritage, culture and language (all of which were highly repressed at the time). He taught all of us that access to knowledge and education should not be taken for granted. My grandmother Sophia Pankiv, orphaned at the young age of 15 (also because of Stalin’s policies), became the primary provider for her household. She wasn’t able to go to university herself but she always valued education and taught all of her kids to read at very young ages. Despite coming from very humble means, all five of my grandparents’ children grew up to get college degrees, which was a huge point of pride for my grandparents. They passed down this love of knowledge and the value of education to all of their kids, grandkids and great-grandkids.

I would be absolutely nowhere without my mom, Olga Pankiv. I owe everything to her. She has been my number one supporter, always cheering me on. She is the hardest working person I’ve ever met and despite being a doctor in Ukraine, started her journey in America cleaning houses. Carrying the importance of education with her across continents, she worked hard to requalify herself as a Nurse Practitioner and is now running a successful practice in Manhattan, NY. In fact, the year that I was starting graduate school, my mom was finishing graduate school at the age of 48. Throughout my graduate school journey, whenever I’ve had doubts, she has always been there to remind me of my inner strength.

My dad Eduard’s words are always with me “If someone else can do it, why not you?”. He helped foster a wonderful learning environment and, when I was young, always supported my Barnes and Noble bargain books addiction. His parents, my grandparents, are currently living in village in the Luhansk region (East of Ukraine) which is unfortunately occupied. It would’ve been much easier (and safer) to flee their village but they wanted to defend everything that they spent a lifetime building. I hope that very soon their home is liberated and we can all get together again.

Even though I am an only child, I come from a very large family, especially on my mom’s side. Most of our family has immigrated to America over the past 20 years and we can always count on each other for support. A special shout out goes to my cousin Rostyslav, his wife Ashley and baby Liam (the newest addition to the family). Rostyk is like a brother to me and we grew up tinkering around, building stuff, riding bikes and just being each other’s confidants. He’s also an extremely humble and smart person. I feel grateful that after all these years, and across multiple countries, we are still thick as thieves.

Now onto my scientific journey. Growing up I always wanted to be a medical doctor. Both of my parents were doctors and dinner conversations often surrounded weird medical cases or some other fascinating thing about the human body. Out of all the things

that came up in medicine, I thought that the brain was by far the coolest organ ever. Digging deeper into psychology and psychiatry turned into a deep love of neuroscience. Eventually, I became much more passionate about understanding the brain at a deeper level — the underlying causes of things — as opposed to treating people directly.

I didn't really know that graduate school was a possibility until my junior year of college in the US. My first science mentor, Dr. Alice Liu took a chance on me. Thank you Dr. Liu for your unending patience when dealing with undergraduate researchers such as myself and for giving us our first exposure to research in a lab. After college, I knew that I really wanted to go to graduate school but wanted to get more experience in systems neuroscience specifically. Dr. Sam Wang believed in me and I went from not really knowing much about systems neuroscience to independently running experiments. I'd love to thank the Wang lab lunch crew (Tom Pisano, Jess Verpeut, and Kelly Seagraves) for always being a wonderful support system throughout my two years as a lab tech and especially throughout the graduate school application process.

My whole scientific journey brought me to Udi Isacoff's lab. Where to begin? This is the best lab with the best people I could ever imagine working with. Udi always somehow manages to recruit the most fun, personable, intelligent, and kind scientists. We're an amalgam of very different personalities but are always there for each other. I'd love to thank Udi himself who is an incredible mentor and always adapts to the needs of his students. He's not only a fantastic scientist but also a wonderful person. I'd also like to thank Zach Newman, my first postdoc mentor in the lab, who taught me all about flies and optical quantal analysis. He also always gave me some of the best recommendations for local food spots to try. I'd also like to thank Ryan Schultz who joined the lab at the same time as I did. We've witness each other go from baby rotation students into full-fledged scientists and I can always count on him to be very insightful and provide caffeine. To Adam Hoagland, who I often share a few laughs with at the fly bench and who is also one of the most technically savvy people in the lab. Our fly team continues to grow and I'd like to thank Susan Younger, Maya Feldthouse, Zerong Cai, and William Liu for keeping our weekly fly meetings fun, insightful, and for being wonderful lab mates. We can always count on each other for virgining or crossing (if you know, you know). There are also a few members of the fly group who have moved on to other places. I'd like to thank Krisha Aghi, who when she wasn't being a computational and statistics mentor was always incredibly supportive and made sure I prioritized my own mental health before anything. To Caroline Cypranowska who was a wonderful office mate, an inspiring scientist, and continues to be an amazing friend.

Some of the other members of the lab include Phil Mendonça who has been incredible to bounce ideas off of. He flipped the entire Chapter 3 of this thesis on its head and we ended up with a much better story in the end. Amy Winans who is also always there for scientific guidance and who has sat with me through many meetings helping me refine my hypotheses and logic about my project. Cherise Stanley has been an incredible office mate and is one of the people I look forward to seeing most at the start of my work days. I can always count on Cherise to share a story or two, a piece of chocolate (or two) and to just be a good friend. Irene Grossrubatscher graduated from the lab a few years ago but continues to be a wonderful friend. I look forward to our weekly climbing sessions and to hearing about her adventures. She inspires me to be my most adventurous and fearless self.

I would also like to thank my committee members: Marla Feller, Kristin Scott and Dan Feldman. They've witnessed my scientific journey and have always provided the most caring and astute advice. It's unlikely that this dissertation would've happened in a timely manner without them and I am extremely grateful for all their guidance.

I've also been fortunate to also have really strong friendships outside the lab as well. During grad school Christiane Voufo and I were each other's support systems. She pushed me to be a better scientist and continues to inspire with her work outside of grad school as well. Kyle Tucker and I are both finishing up our dissertations at the same time and we can always count on each other for a few brief words of encouragement or a catch-up coffee that ends up lasting many hours.

To my Ukrainian gal pals: Yelena Kulik, Anna Brockway, Vira Iefremova, and Oleksandra Kepple. We came into each other's lives because of the brutal and unjust attack of our beloved Ukraine. Through one of the most painful times in all of our lives we've grown incredibly close and are now like an extended family. We teach each other about our own Ukrainian traditions (we're all from different regions), have gone on many trips together and continue to support one another personally and professionally. They have become a source of comfort during one of the most stressful times in all of our lives. I'd like to particularly thank Vira and Oleksandra. Together we co-founded a non-profit, ReImagine Ukraine Foundation, and are constantly working on making sure that we are doing the most that we can for Ukraine. They are my dream team and I feel incredibly lucky that we keep turning our ideas into realities.

To my friends who are now far away. Raphael who is the first friend I made in college and the most talented chef I know. Justine, who is always there for me and a super talented musician. Cornelius and Nina who have moved to Switzerland and now give us a wonderful excuse to get into mountaineering. Doing epic treks with them has become a yearly tradition.

To my husband, my love, and my partner of 9.5 years, Chris Kaplan. I count my lucky stars that we joined the same research club back when we were undergraduates at Rutgers. Who knew that meeting at the Aresty Research Center would lead to almost 10 years with the kindest, smartest person I know? Chris inspires me to be a better version of myself and brings out the best in me. He has been by my side through my lowest lows and my highest highs. I'm so grateful for all the adventures that we've had so far and I'm excited to see what our future holds.

Chris and I are lucky to have some of our closest friends in the Bay Area. Steven, Liz and Scott are like our extended family. We have been there for each other through Covid, losing loved ones, the full-scale invasion of Ukraine, but also many wonderful things such as weddings, engagements and promotions. I know that no matter where we are in the world, we'll always be up for adventures together.

Finally, this dissertation is dedicated to the brave people of Ukraine. And that includes many of my friends and family members. Their bravery, resilience and grace will never cease to amaze me. They continue to inspire me and the whole world. I finished high school in Ukraine and that is where my heart currently is. In fact, I'm writing this on my way to my home city of Lviv. I'd like to highlight one of my best friends from high school, Taras who is an extremely talented architect, recently got married and had a baby but is now fighting on the front lines. During the first days of the full-scale invasion, when media in the US was saying "Kyiv will fall in three days.", Taras — already on his way to the front lines — would tell me “We got this. We’re ready.” He inspires me to be brave. I am forever grateful to him and to all the members of the Armed Forces of Ukraine, Territorial Defense groups, and volunteers who are risking their lives daily to make sure that our families, homes, cultures, language, heritage, and our land are safe from invaders. I know that very soon we will all celebrate Ukrainian Victory.

Table of Contents

CHAPTER 1: Introduction to synaptic heterogeneity and the *Drosophila* neuromuscular junction.

The human brain is the most complicated organ in our bodies with as many as 86 billion neurons[1] working in concert to perform functions ranging from the most basic/reflexive ones such as removing the hand touching a hot plate to the most complicated ones such as compiling years of research into a single dissertation. While neurons themselves are mostly static with a few exceptions, the points of contacts between neurons (i.e., synapses) are very dynamic[2] and are the fundamental units of the nervous system that direct the flow of activity through neural circuits.

Almost every function that the brain performs, from learning and memory to sensory adaptation, relies on changes at the level of the synapse [3,4]. Moreover, a number of neurodevelopmental (such as Autism Spectrum Disorder and Schizophrenia) as well as neurodegenerative (such as Parkinson's Disease) disorders are known to be the result of the dysfunction of these connections between neurons [5]. In order to truly understand neuronal function, we must be able to understand synapses.

The synapse

Synapses come in two forms: electrical (via gap-junctions) and chemical, which release neurotransmitter. Most of the neuron–neuron connections are via chemical synapses and those will be the focus of this dissertation. Back in the 1950s, Katz and colleagues proposed a new framework for understanding synaptic function[6]. While studying the frog neuromuscular junction (NMJ), their work determined that synaptic release is composed of multiple, additive, miniature release events (minis or spontaneous events)[6,7]. A few decades later, Heuser et al., showed that these individual miniature release events were correlated with the presence of individual synaptic vesicles fusing to the membrane during electrical stimulation, consistent with the release of neurotransmitter in quantized units thus rounding out the quantal framework of synaptic transmission[8]**.** Combining all of these factors including the binomial model of transmission[9], synaptic strength can be mathematically described as the following product

$$Synaptic\ Strength = n * P_r * q \qquad (1)$$

where n is the number of release sites or Active Zones (AZs), P_r is their probability of releasing neurotransmitter in response to an action potential (AP), and q is the size of the postsynaptic depolarization caused by neurotransmitter release from a single quantum.

In addition to being critical to nervous system function, synapses are highly heterogeneous and can vary greatly in their transmission properties, both between neurons and—surprisingly—within a single neuron synapsing onto the same cell.[2,11] Synapses can vary in the likelihood of releasing neurotransmitter, the amount of neurotransmitter released and/or how sensitive the receiving cell is to the neurotransmitter[3]. Synapses are also highly dynamic and can undergo changes in synaptic strength on the timescales of milliseconds, minutes, and even days[8–13]. This diversity in synaptic structures and the dynamic regulation in synaptic strength [12] are thought to underlie the nervous system's ability to reliably transmit information between cells despite extremely different patterns of neural activity. In particular, the P_r of a synapse is thought to be an important factor in determining the variations of synaptic strength[10]. The higher the P_r, the stronger the synapse.

Even with the recognition that heterogeneity in synaptic strength is critical to nervous system function, due to the molecular complexity of synapses and technological limitations, very little is known about the molecular mechanisms that regulate synaptic strength *in vivo.*

Models and methods for studying synaptic function

Given that P_r is so central in defining synaptic strength and the synapse's dynamic adaptation to activity, it's important to be able to measure P_r in a reliable way, across many synapses simultaneously and *in vivo.* To accomplish this goal, we turn to the *Drosophila* larval neuromuscular junction (NMJ) as a model system.

The *Drosophila* NMJ

The *Drosophila* larval NMJ receives input from a few different types of motoneurons (MNs). Type I are the primary glutamatergic inputs, provide the drive for muscle contraction, and can be divided into Ib(big) and Is(small) (**Fig 1.1A**). Type II MNs release neuromodulators, such as octopamine—the invertebrate analog of norepinephrine—from small clear vesicles. Finally, type III release neuropeptides from dense core vesicles and are usually activated at much higher frequencies that the other two types[17]. Almost every muscle cell receives input from the two type I MNs and a type II MN, which have been shown to be linked both functionally[18] and spatially[19].

Within the NMJ, both type I and type II have synapses marked by multiple release sites, (i.e., active zones (AZs)), which are identified by the presence of the AZ-scaffolding protein Bruchpilot (Brp) (**Fig 1.1A, B**) (type II not shown). In particular, the two type I MNs have hundreds of AZs which synapse onto the muscle cell. A single AZ is only about 200-300 nm across and is the site from which synaptic transmission occurs. It is also the clustering site for many of the essential proteins which participate in synaptic release (**Fig. 1.1C**) and will be discussed in greater detail below as well as in Chapters 2 and 3 of this dissertation.

Overall, the *Drosophila* larval NMJ is an ideal model for synaptic transmission for many reasons. Just like the mammalian central nervous system (CNS), the fly NMJ utilizes glutamate as its primary neurotransmitter. Moreover, the majority of the proteins that play a role in synaptic transmission in the mammalian brain have homologs in the fly. The model system is also highly accessible experimentally and tractable because we can measure the activity of the same type I MNs synapsing onto the same muscle cells (in our case we investigate muscle 4) across animals. Finally, flies are a useful model system because of the incredible array of existing genetic tools that allow probing the molecular machinery underlying synaptic transmission. All of these factors combined have made the fly NMJ an incredibly powerful model to study synaptic development, diversity and transmission while also being able to relate the findings to other organism [17,20–24].

Optical quantal analysis and synaptic heterogeneity

In order to investigate transmission at single synapses, our lab employs optical quantal analysis (OQA) along with an optical sensor that detects postsynaptic calcium entry through glutamate receptors (most recent published iteration: SynapGCaMP6f)[25–27]. We were able to identify individual release sites located within 400-500nm of each other by measuring individual synaptic release events. Specifically, we measure the quantal size (q) as the amplitude of the postsynaptic calcium response, the number and location of independent functional synaptic sites (n), and finally the probability of release (P_r) as the fraction of action potentials (APs) that evoke transmission at each site. Using OQA, our lab has shown that there's a heterogeneous distribution in P_r (.01 to .62), up to a 50-fold (5,000%) variation in active zones emerging from a single axon, and sometimes between active zones as close as a couple of hundred of nanometers from each other [25–27](**Fig 1.2**).

Previous OQA led to significant discoveries about synaptic heterogeneity, defined as the variations in synaptic strength. However, due to the size of synapses (<1μm), the spacing between synapses (<500nm) (see **Fig.1.1A** showing densely packed synapses and **Fig1.2A,B** for a schematic), and Ca^{2+} diffusing from the point of release, the method lacked sufficient spatial resolution to distinguish activity at different sites and was prone to merging events from neighboring synapses

To overcome this, we developed an innovative, super-resolution method of OQA called Quantal Synaptic Optical Reconstruction (QuaSOR), which improved our resolution 5-10x (see **Fig. 1.1D** for comparison between methods), and allows us to unambiguously detect transmission at every synapse. QuaSOR analysis relies on similar methods used in super-resolution microscopy such as STORM in which we fit our $\Delta F/F$ signals (from SynapGCaMP6f) to 2D-Gaussian functions[28]. We can then define the release origin as the maxima of the Gaussian function, similar to strategies used with pHluorin-based SV indicators[29,30]. Importantly, this gives us the ability to separate out events even when the Ca^{2+} responses are overlapping, which was a limiting factor in previous OQA methods[31,32].

Molecular basis for synaptic heterogeneity

Considering the large degree of synaptic heterogeneity across the active zones that comprise the overall synaptic connections between a single neuron and a single muscle, the central hypothesis of our previous work and this dissertation is that synaptic strength and its heterogeneity is set by a very precise distribution of proteins at single synapses.

Molecular determinants

Our understanding of the molecular correlates and determinants of synaptic heterogeneity remain poorly understood because many molecules must operate together for effective transmitter release [2,] and because of the technological limitations allowing functional–structural correlation at single synapse resolution [5–12]. However, by combining QuaSOR with super-resolution structural imaging methods: Airy(**Chapters 2** and **3** of this dissertation**)** and Stochastic Optical Reconstruction Microscopy (STORM) (**Chapter 2**), we were able to obtain both super-resolution functional *and* structural data across hundreds of single synapses and *in vivo*.

Decades of prior research state that the differences in P_r could be attributed to many different presynaptic factors including: differences in the number of readily releasable (RRP) vesicles[40], amount of presynaptic Ca^{2+} influx[41], size of the AZ[42], clustering of voltage-gated calcium channels (VGCCs)[43], synaptic vesicle (SV)-VGCC coupling [44], and the molecular state of SV release machinery[45].

Moreover, differences in synaptic strength could be due to differing amounts of essential proteins at the synapse (**Fig. 1.3, top panel**) or different biophysical states of essential proteins such as Unc13A (**Fig. 1.3, bottom panel**). Using the *Drosophila* larva NMJ model, along with the high resolution functional data from QuaSOR with super-resolution structural analysis (confocal Airy and STORM) at hundreds of synapses in parallel we can begin to understand what are some of the molecular determinants that underlie synaptic heterogeneity (**Chapters 2 and 3**).

Neuromodulation at the *Drosophila* NMJ

In addition to having a very large heterogeneity in basal synaptic strength, synapses at the NMJ also undergo varying degrees of potentiation by essential neuromodulators (released from type II MNs(**Fig 1.2A**)). This variation in synaptic potentiation is also true for synapses with similar basal synaptic strength (i.e., basal P_r and amount of Brp at the synapse) (**Chapter 3**). Octopamine (OA) is the invertebrate counterpart of norepinephrine and is an important physiological regulator which controls and modulates locomotion, circadian rhythm, learning and memory among other functions[46]. Previous studies have shown that optogenetic activation of type II MNs— which release OA— increases locomotion in *Drosophila* larvae and leads to OA-dependent increase in the number of boutons in type I MNs[18]. Studies have also shown that acute application of OA (10 μM), increases the excitatory junction potentials (EJPs) in the muscle . However, it was not clear whether this effect was due to pre- or postsynaptic action since OA receptors are found on both sides of the synapse[18,47].

In this dissertation, using the tools we develop in **Chapter 2**, we're able to investigate not only differences in basal synaptic strength, but also the molecular underpinnings of differential response to neuromodulators both at NMJ overall and locally at the synapse (**Chapter 3**).

Figures

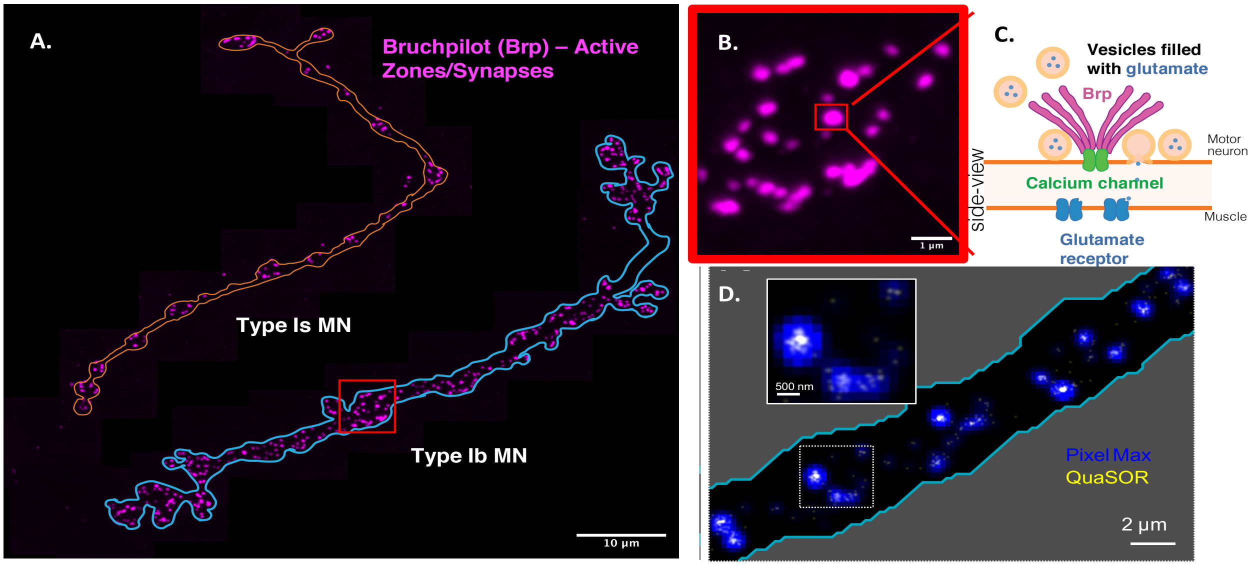

Figure 1.1: *Drosophila* NMJ as a model glutamatergic synapse.
A) Airyscan confocal image showing the two type I motor neuron (MN) inputs to the muscle: Ib (blue outline) and Is(orange outline). Stained for the presynaptic active zone scaffolding protein Bruchpilot, Brp. Scale bar = 10 μm
B) Zoomed in Ib bouton (red box in (A)). Every magenta spot is a synpase/AZ. Scale bar = 1 μm
C) Schematic side-view of the AZ depicting some of the essential proteins participating in release.
D) Comparison of AP-evoked pixel-maxima and QuaSOR mapping methods for the Ib NMJ (pixel-maxima blue, 211.6 nm/px, σ = 211.6 nm; QuaSOR yellow, 21.2 nm/px, σ = 42.3 nm; overlap white). 5-10x improvement in spatial resolution.

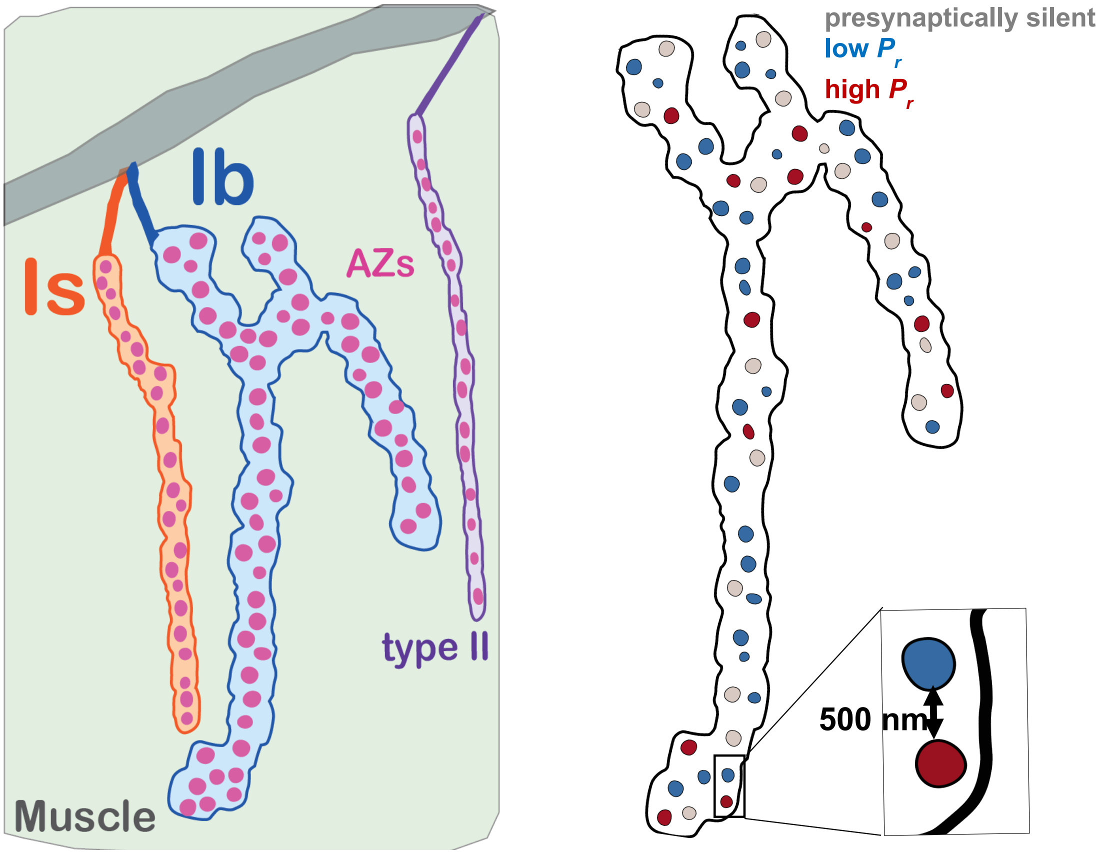

Figure 1.2. Schematic of the diversity within a single Ib MN
A) Schematic depicting the *Drosophila* NMJ illustrating type II MN (purple), type I MNs: Ib (blue) and Is MN (orange) synapsing onto the same muscle. Individual Active Zones (AZs) are shown in magenta.
B) Schematic of the same Ib MN as in (A). AZs are colored by their likelihood of releasing neurotransmitter (P_r). Beige-colored AZs are presynaptically silent (~20%). Blue AZs are low-P_r synapses and red are high-P_r. Inset: zoomed in schematic of neighboring AZs which can have up to a 50-fold (5,000%) difference in P_r.

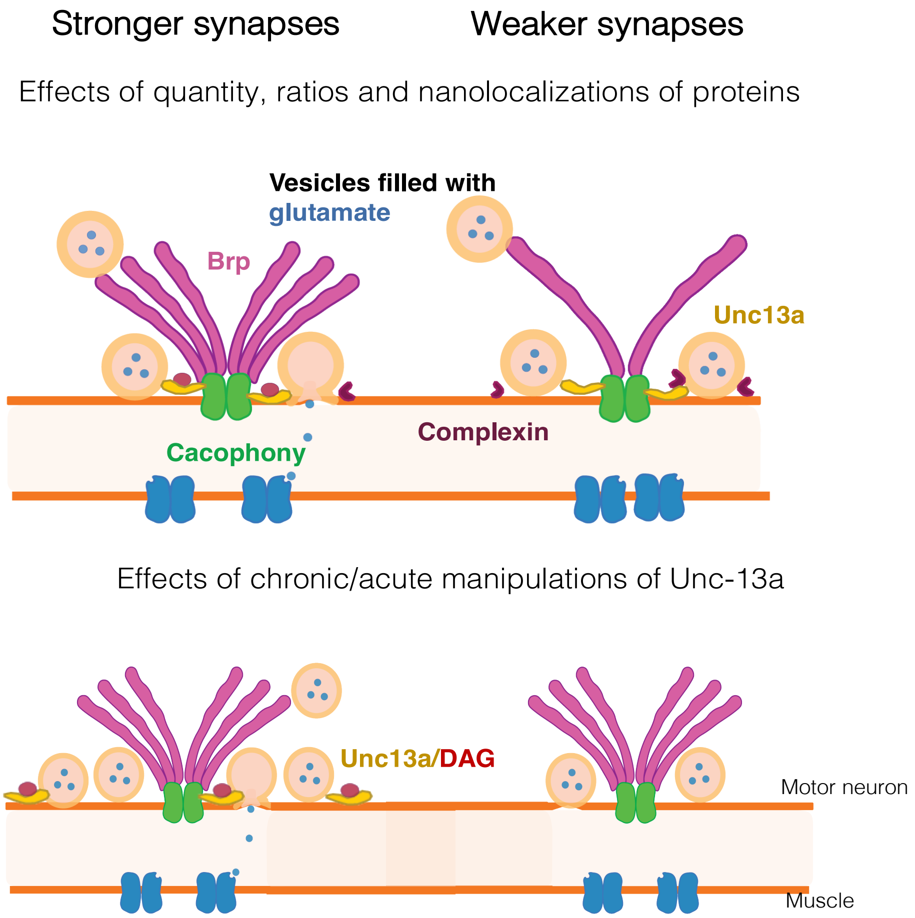

Figure 1.3: Hypotheses for the molecular basis of variation in synaptic strength.
Top panel: differences in local quantities of synapes and/or relative abundances set synaptic strength. Cacophony is the *Drosophila* Ca^{2+} channel. Complexin is a small protein that acts as a break on release.
Bottom panel: Unc13a binding DAG increases synaptic strength(left) or Unc-13a KD(right) decreases synaptic strength.

References

1. Azevedo FAC, Carvalho LRB, Grinberg LT, et al. Equal numbers of neuronal and nonneuronal cells make the human brain an isometrically scaled-up primate brain. *J Comp Neurol*. 2009;513(5):532-541. doi:10.1002/cne.21974

2. Branco T, Staras K. The probability of neurotransmitter release: variability and feedback control at single synapses. *Nat Rev Neurosci*. 2009;10(5):373-383. doi:10.1038/nrn2634

3. Citri A, Malenka RC. Synaptic Plasticity: Multiple Forms, Functions, and Mechanisms. *Neuropsychopharmacology*. 2008;33(1):18-41. doi:10.1038/sj.npp.1301559

4. Regehr WG. Short-Term Presynaptic Plasticity. *Cold Spring Harb Perspect Biol*. 2012;4(7):a005702-a005702. doi:10.1101/cshperspect.a005702

5. Lepeta K, Lourenco MV, Schweitzer BC, et al. Synaptopathies: synaptic dysfunction in neurological disorders - A review from students to students. *J Neurochem*. 2016;138(6):785-805. doi:10.1111/jnc.13713

6. del Castillo J, Katz B. Quantal components of the end-plate potential. *J Physiol*. 1954;124(3):560-573. doi:10.1113/jphysiol.1954.sp005129

7. Fatt P, Katz B. Spontaneous subthreshold activity at motor nerve endings. *J Physiol*. 1952;117(1):109-128. doi:10.1113/jphysiol.1952.sp004735

8. Synaptic vesicle exocytosis captured by quick freezing and correlated with quantal transmitter release. *J Cell Biol*. 1979;81(2):275-300.

9. Walmsley B, Edwards F, Tracey D. The probabilistic nature of synaptic transmission at a mammalian excitatory central synapse. *J Neurosci*. 1987;7(4):1037-1046. doi:10.1523/JNEUROSCI.07-04-01037.1987

10. Dürst CD, Wiegert JS, Schulze C, Helassa N, Török K, Oertner TG. Vesicular release probability sets the strength of individual Schaffer collateral synapses. *Nat Commun*. 2022;13(1):6126. doi:10.1038/s41467-022-33565-6

11. Branco T, Staras K, Darcy KJ, Goda Y. Local Dendritic Activity Sets Release Probability at Hippocampal Synapses. *Neuron*. 2008;59(3):475-485. doi:10.1016/j.neuron.2008.07.006

12. Atwood HL, Karunanithi S. Diversification of synaptic strength: presynaptic elements. *Nat Rev Neurosci*. 2002;3(7):497-516. doi:10.1038/nrn876

13. Éltes T, Kirizs T, Nusser Z, Holderith N. Target Cell Type-Dependent Differences in Ca $^{2+}$ Channel Function Underlie Distinct Release Probabilities at Hippocampal

Glutamatergic Terminals. *J Neurosci*. 2017;37(7):1910-1924. doi:10.1523/JNEUROSCI.2024-16.2017

14. Koester HJ, Johnston D. Target Cell-Dependent Normalization of Transmitter Release at Neocortical Synapses. *Science*. 2005;308(5723):863-866. doi:10.1126/science.1100815

15. O'Rourke NA, Weiler NC, Micheva KD, Smith SJ. Deep molecular diversity of mammalian synapses: why it matters and how to measure it. *Nat Rev Neurosci*. 2012;13(6):365-379. doi:10.1038/nrn3170

16. Reyes A, Lujan R, Rozov A, Burnashev N, Somogyi P, Sakmann B. Target-cell-specific facilitation and depression in neocortical circuits. *Nat Neurosci*. 1998;1(4):279-285. doi:10.1038/1092

17. Ruiz-Cañada C, Budnik V. Introduction on The Use of The Drosophila Embryonic/Larval Neuromuscular Junction as A Model System to Study Synapse Development and Function, and A Brief Summary of Pathfinding and Target Recognition. In: *International Review of Neurobiology*. Vol 75. The Fly Neuromuscular Junction: Structure and Function Second Edition. Academic Press; 2006:1-31. doi:10.1016/S0074-7742(06)75001-2

18. Koon AC, Ashley J, Barria R, et al. Autoregulatory and paracrine control of synaptic and behavioral plasticity by octopaminergic signaling. *Nat Neurosci*. 2011;14(2):190-199. doi:10.1038/nn.2716

19. Stocker B, Bochow C, Damrau C, et al. Structural and Molecular Properties of Insect Type II Motor Axon Terminals. *Front Syst Neurosci*. 2018;12:5. doi:10.3389/fnsys.2018.00005

20. Broadie KS, Richmond JE. Establishing and sculpting the synapse in Drosophila and C. elegans. Published online 2002.

21. Collins CA, DiAntonio A. Synaptic development: insights from Drosophila. *Curr Opin Neurobiol*. 2007;17(1):35-42. doi:10.1016/j.conb.2007.01.001

22. Frank CA, Wang X, Collins CA, et al. New Approaches for Studying Synaptic Development, Function, and Plasticity Using *Drosophila* as a Model System. *J Neurosci*. 2013;33(45):17560-17568. doi:10.1523/JNEUROSCI.3261-13.2013

23. Hallermann S, Heckmann M, Kittel RJ. Mechanisms of short-term plasticity at neuromuscular active zones of *Drosophila*. *HFSP J*. 2010;4(2):72-84. doi:10.2976/1.3338710

24. Keshishian H, Broadie K, Chiba A, Bate M. The Drosophila Neuromuscular Junction: A Model System for Studying Synaptic Development and Function. Published online 1996.

25. Peled ES, Newman ZL, Isacoff EY. Evoked and Spontaneous Transmission Favored by Distinct Sets of Synapses. *Curr Biol*. 2014;24(5):484-493. doi:10.1016/j.cub.2014.01.022

26. Peled ES, Isacoff EY. Optical quantal analysis of synaptic transmission in wild-type and rab3-mutant Drosophila motor axons. *Nat Neurosci*. 2011;14(4):519-526. doi:10.1038/nn.2767

27. Newman ZL, Hoagland A, Aghi K, et al. Input-Specific Plasticity and Homeostasis at the Drosophila Larval Neuromuscular Junction. *Neuron*. 2017;93(6):1388-1404.e10. doi:10.1016/j.neuron.2017.02.028

28. Small AR, Parthasarathy R. Superresolution Localization Methods. *Annu Rev Phys Chem*. 2014;65(1):107-125. doi:10.1146/annurev-physchem-040513-103735

29. Maschi D, Klyachko VA, Maschi D, Klyachko VA. Spatiotemporal Regulation of Synaptic Vesicle Fusion Sites in Central Synapses Report Spatiotemporal Regulation of Synaptic Vesicle Fusion Sites in Central Synapses. *Neuron*. 94(1):65-73.e3. doi:10.1016/j.neuron.2017.03.006

30. Tang AH, Chen H, Li TP, Metzbower SR, MacGillavry HD, Blanpied TA. A trans-synaptic nanocolumn aligns neurotransmitter release to receptors. *Nature*. 2016;536(7615):210-214. doi:10.1038/nature19058

31. Kim N, Heo M, Fleysher R, Branch CA, Lipton ML. A Gaussian Mixture Model Approach for Estimating and Comparing the Shapes of Distributions of Neuroimaging Data: Diffusion-Measured Aging Effects in Brain White Matter. *Front Public Health*. 2014;2. doi:10.3389/fpubh.2014.00032

32. Bilmes JA. A Gentle Tutorial of the EM Algorithm and its Application to Parameter Estimation for Gaussian Mixture and Hidden Markov Models.

33. Südhof TC. The Presynaptic Active Zone. *Neuron*. 2012;75(1):11-25. doi:10.1016/j.neuron.2012.06.012

34. Südhof TC. THE SYNAPTIC VESICLE CYCLE. *Annu Rev Neurosci*. 2004;27(1):509-547. doi:10.1146/annurev.neuro.26.041002.131412

35. Sudhof TC. Calcium Control of Neurotransmitter Release. *Cold Spring Harb Perspect Biol*. 2012;4(1):a011353-a011353. doi:10.1101/cshperspect.a011353

36. Kittel RJ, Heckmann M. Synaptic Vesicle Proteins and Active Zone Plasticity. *Front Synaptic Neurosci*. 2016;8. doi:10.3389/fnsyn.2016.00008

37. Ackermann F, Waites CL, Garner CC. Presynaptic active zones in invertebrates and vertebrates. *EMBO Rep*. 2015;16(8):923-938. doi:10.15252/embr.201540434

38. Ariel P, Ryan TA. New Insights Into Molecular Players Involved in Neurotransmitter Release. *Physiology*. 2012;27(1):15-24. doi:10.1152/physiol.00035.2011

39. Ribrault C, Sekimoto K, Triller A. From the stochasticity of molecular processes to the variability of synaptic transmission. *Nat Rev Neurosci*. 2011;12(7):375-387. doi:10.1038/nrn3025

40. Holderith N, Lorincz A, Katona G, et al. Release probability of hippocampal glutamatergic terminals scales with the size of the active zone. 2015;15(7). doi:10.1038/nn.3137

41. Schneggenburger R, Neher E. Presynaptic calcium and control of vesicle fusion. *Curr Opin Neurobiol*. 2005;15(3):266-274. doi:10.1016/j.conb.2005.05.006

42. Holderith N, Lorincz A, Katona G, et al. Release probability of hippocampal glutamatergic terminals scales with the size of the active zone. *Nat Neurosci*. 2012;15(7):988-997. doi:10.1038/nn.3137

43. Keller D, Babai N, Kochubey O, Han Y, Markram H. An Exclusion Zone for Ca 2 + Channels around Docked Vesicles Explains Release Control by Multiple Channels at a CNS Synapse. Published online 2015:1-21. doi:10.1371/journal.pcbi.1004253

44. Wadel K, Neher E, Sakaba T. The Coupling between Synaptic Vesicles and Ca 2 + Channels Determines Fast Neurotransmitter Release. Published online 2007:563-575. doi:10.1016/j.neuron.2007.01.021

45. Lou X, Scheuss V, Schneggenburger R. Allosteric modulation of the presynaptic Ca 2 1 sensor for vesicle fusion. 2005;435(May):497-501. doi:10.1038/nature03568

46. Balfanz S, Strünker T, Frings S, Baumann A. A family of octapamine receptors that specifically induce cyclic AMP production or Ca2+ release in Drosophila melanogaster. *J Neurochem*. 2005;93(2):440-451. doi:10.1111/j.1471-4159.2005.03034.x

47. Koon AC, Budnik V. Inhibitory Control of Synaptic and Behavioral Plasticity by Octopaminergic Signaling. *J Neurosci*. 2012;32(18):6312-6322. doi:10.1523/JNEUROSCI.6517-11.2012

CHAPTER 2: Determinants of synapse diversity revealed by super-resolution quantal transmission and active zone imaging

Zachary L. Newman[1], **Dariya Bakshinskaya[2]**, Ryan Schultz[2], Samuel J. Kenny[4], Seonah Moon[4], Krisha Aghi[2], Cherise Stanley[1], Nadia Marnani[1], Rachel Li[1], Julia Bleier[2], Ke Xu[2,4,5] and Ehud Y. Isacoff[1,2,3,5,*]

[1] Department of Molecular and Cell Biology, University of California Berkeley, Berkeley, California 94720

[2] Helen Wills Neuroscience Institute, University of California Berkeley, Berkeley, California 94720

[3] Weill Neurohub, University of California Berkeley, Berkeley, California 94720

[4] Department of Chemistry, University of California, Berkeley, CA 94720, USA

[5] Molecular Biophysics and Integrated BioImaging Division, Lawrence Berkeley National Laboratory, Berkeley, California 94720

This work was published in *Nature Communications* in January, 2022

Author contributions: Z.L.N. conceived and performed experiments, analyzed data and co-wrote the manuscript. S.J.K. and S.M. performed STORM imaging and assisted in STORM analysis. D.B. assisted in STORM analysis. R.S., N.M., and R.L. performed immunohistochemistry, confocal, and Airyscan imaging. D.B., R.S., S.J.K., J.B., and C.S. assisted in active zone matching analysis and cross-platform alignments. K.A. and J.B. assisted in functional analysis. K.X. helped conceive the project and supervised the STORM analysis. E.Y.I. conceived and supervised the project and co-wrote the manuscript.

Abstract

To understand the mechanisms that set presynaptic strength in the nervous system, we developed a super-resolution optical quantal analysis to relate transmission at thousands of excitatory glutamatergic synapses of the *Drosophila* larval neuromuscular junction (NMJ) to super-resolution 3D molecular reconstructions of presynaptic active zones (AZs). The probability of action potential evoked release (P_r) varied over a remarkable 100-fold range, suggesting substantial molecular diversity between AZs. Two key AZ proteins, scaffolding protein Bruchpilot and Ca^{2+} channel Cacophony, varied greatly, correlated to P_r in both quantity and nanoscale distribution, but accounted for only a minority of P_r variance. Complexin suppressed both spontaneous and evoked transmission, but differentially: completely blocking spontaneous transmission at the site of maximal evoked transmission to generate a spatial and quantitative mismatch between release modes. Thus, our new methodology demonstrates that transmission strength and spatial organization is regulated by the balance between, and nanoscale distribution of, release-enhancing and suppressing presynaptic proteins, together generating a high signal-to-noise for evoked release.

Introduction

The operation of neural circuits depends on the synaptic connections between neurons. To understand how neural circuits process and store information, one needs to understand the molecular mechanisms that govern synaptic transmission and distribute synaptic weights across large numbers of connections. While determinants of postsynaptic strength (e.g. dendritic spine size, postsynaptic scaffold size, number of postsynaptic receptors) are well characterized[1–4], the presynaptic determinants are not as clear. The relationship between synapse morphology and presynaptic action potential (AP)-evoked neurotransmitter release probability (P_r) is weak[5–10] as is the dependence of P_r on specific elements of the transmitter release apparatus, the active zone (AZ)[11–18].

To understand how presynaptic machinery governs quantal transmission, one needs to measure P_r at identified synapses whose molecular constituents and organization can be analyzed directly. Three approaches have been used to measure transmission at multiple identified synapses. Postsynaptic quantal (i.e. single synaptic vesicle resolution) imaging with Ca^{2+} indicators detects flux through ionotropic receptors as a proxy for the excitatory postsynaptic response[19,20,29–34,21–28], biosensors detect released neurotransmitters[35] and presynaptic synaptopHluorins detect vesicle fusion[36–38]. However, the diffraction-limited nature of these imaging paradigms makes it difficult to assign transmission events to particular synapses when AZs are densely arrayed.

To overcome these limitations, we developed a combination of super-resolution imaging modalities to precisely relate quantal transmission to synaptic architecture at the glutamatergic model synapse of the *Drosophila* NMJ. We used the logic of stochastic single molecule super-resolution localization microscopy to develop Quantal Synaptic Optical Reconstruction ("QuaSOR"), analogous to recent super-resolution imaging of transmission in neuronal culture with synaptopHluorin and iGluSnFR[37,51,52]. QuaSOR resolved both action potential evoked and spontaneous quantal transmission events to individual synapses, even in regions where the synapses are crowded. QuaSOR allowed us to map locations of quantal transmission, quantify P_r using failure analysis and measure the frequency of spontaneous transmission (F_s) at hundreds of synapses simultaneously throughout the NMJ, under physiological conditions. QuaSOR analysis was followed by super-resolution molecular imaging of presynaptic AZ proteins, enabling spatial averaging of protein and transmission localizations that revealed new aspects of synaptic mechanism.

We found that P_r has a high power dependence on the quantity of the presynaptic voltage-gated Ca^{2+} channel Cacophony (Cac)[39], consistent with the power dependence of quantal content on Ca^{2+} [40–43]. P_r also had a strong dependence on the scaffolding protein Bruchpilot (Brp), which organizes the AZ and anchors synaptic vesicles near the site of release[44–46]. However, Cac and Brp together accounted for only a minor fraction of the variance in P_r, indicating that other important factors control and diversify AP-evoked release. A clue about one additional contributor came from an observation that evoked and spontaneous transmission modes are mismatched spatially and quantitatively. This led us to investigate Complexin (Cpx), whose *Drosophila* homolog is a powerful inhibitor of spontaneous transmitter release[47] and which contains subdomains that both facilitate and inhibit evoked release[48]. As the Cpx/Brp ratio increased, P_r declined. When Cpx was knocked down, the mismatch between spontaneous and evoked transmission disappeared. Additionally, P_r was higher compared to control synapses with the same Brp content. We conclude that the interplay between release-promoting Cac and Brp and release-suppressing Cpx sets presynaptic transmission strength, generates synapse-to-synapse diversity and enhances quantal signal-to-noise by suppressing spontaneous release at the site of maximal evoked release. The results demonstrate how super-resolution structure/function imaging can reveal the mechanisms of regulation of synaptic function.

Results

Super-resolution mapping of synaptic transmission sites and quantification of presynaptic strength

Postsynaptic receptors at the *Drosophila* NMJ are Ca^{2+} permeable[49], enabling detection of quantal, single synaptic vesicle transmission with the postsynaptically targeted genetically-encoded Ca^{2+} indicator SynapGCaMP6f[28]. However, diffusion of Ca^{2+} in the postsynaptic cytoplasm (**Suppl. Fig. 2.1a-f**) makes it challenging to separate quantal events arising at nearby synapses. Our earlier optical quantal analysis assigned transmission events to maximal fluorescence pixels and did not anchor these measurements to molecular maps of synapse location with sufficient resolution to resolve all synapses[28,33,34]. This resulted in events from neighboring synapses sometimes becoming conflated. We overcame this by developing QuaSOR, an analysis method that combines the fitting logic of single-molecule localization microscopy[50], with the naturally low probability and stochastic nature of vesicle fusion at the NMJ to enhance spatial resolution. Similar strategies have been applied in neuronal culture for super-resolution synaptopHluorin and iGluSnFR imaging at single synapses[37,51,52]. We fitted two-dimensional (2D) asymmetric Gaussian functions to the Ca^{2+} signal for spontaneous and AP-evoked events (**Fig. 2.1a-h** and **Suppl. Fig. 2.1g-j**). With AP-evoked transmission, fitting was more challenging because events sometimes occurred synchronously at neighboring synapses (**Fig. 2.1e,f**). However, these responses were separated and resolved with 2D Gaussian mixture models (**Figs. 2.1f-h** and **Suppl. Fig. 2.1i,j**).

We measured synaptic release probability (P_r) as the number of postsynaptic Ca^{2+} events evoked at each synapse by a train of motor nerve stimuli (evoked events / number of stimuli). This is the same as classical failure analysis, but performed at individual synapses (rather than groups) and at physiological Ca^{2+} (i.e. at normal quantal content, rather than artificially lowered levels), where each stimulus evoked an event of failed to evoke an event. Comparing QuaSOR to our previous method of pixel-maxima mapping (**Fig. 2.1i-k; Suppl. Fig. 2.1n-w**), QuaSOR resolved evoked events with 3.8-fold higher spatial resolution (average half max cluster area for pixel-maxima = 0.171 ± 0.006 μm^2 and for QuaSOR = 0.045 ± 0.002 μm^2; n = 45 NMJs; see **Methods**).

Most body wall muscles of *Drosophila* larvae are innervated by two glutamatergic motor axons, Type Ib and Is, which perform distinct functions during locomotion[28]. By overlaying QuaSOR maps of AP-evoked and spontaneous quantal transmission locations, we found a spatial mismatch between site4s of spontaneous and evoked transmission (**Suppl. Fig. 2.2a-c**). QuaSOR analysis confirmed that Type Is synapses have an ~2.5-fold higher P_r than Ib synapses (**Suppl. Fig. 2.2d,e**)[28].

3D-STORM of AZ molecular nanostructure

Next, in order to anchor sites of transmission to molecular maps of synapse locations, we followed QuaSOR with two-color 3D-STORM[53–56]. We initially focused on two key components of the presynaptic AZ: Brp, the CASK/ELKS-type scaffolding protein[44,45], and Cac, the voltage-gated Ca^{2+} channel of the presynaptic release site[39,57]. To avoid potential mislocalization due to over-expression and/or fluorescent tags, we utilized antibodies to the native proteins (**Suppl. Fig. 2.3**). As shown previously with single-color 2D-STORM[58], simultaneous two-color, 3D-STORM resolved AZs throughout the depth of the NMJ (**Fig. 2.2a**), providing a complete AZ map for multiple boutons, each containing many synapses (**Suppl. Fig. 2.4a-d**). For a large number of AZs, Brp molecules were found to be arrayed in small clusters forming rings (**Fig. 2.2a**)[58], whereas Cac in AZs was concentrated in small puncta[59], often near Brp clusters, and embedded within Brp rings (**Fig. 2.2a**).

The relative positions of Brp and Cac within the AZ and 3D location of the AZ within the bouton, combined with the fact that the epitope for the Brp antibody lies at the Brp C-terminal, opposite from the plasma membrane end[46], enabled us to identify *en face* oriented AZs (**Fig. 2.2b-g**), which aligns the maximal spatial *x*-*y* resolution of 3D-STORM imaging with the plane of the membrane. Following a strategy of STORM particle averaging[60–62], we generated AZ-aligned localization density averages and radial density profiles for *en face* AZs (**Fig. 2.2h**). Consistent with earlier STED observations[59,63], Brp was distributed as an annulus around Cac, with a maximum density ~100 nm from the Cac center (**Fig. 2.2i**). In order to validate the quantitative output of our STORM imaging, we first compared AZ architecture between Is and Ib inputs to the same muscle. Type Is AZs were slightly smaller than Ib AZs (**Suppl. Fig. 2.4a,b**), as observed previously[58]. Is AZs, had similar numbers of Cac localizations (**Suppl. Fig. 2.4c,d**) and very slightly fewer Brp localizations (**Suppl. Fig. 2.4e,f**). Because Is AZs were generally more compact, their Cac density was higher (**Suppl. Fig. 2.4g,h**), although their Brp density did not differ (**Suppl. Fig. 2.4i,j**). This suggests that the density of Ca^{2+} influx within the AZ may contribute to the higher P_r of Is synapses, as described in the calyx of Held[12].

Transmission diversity

Having established QuaSOR for mapping transmission site localizations and measuring P_r and F_s, along with two-color 3D-STORM reconstruction of AZs, we could now relate transmission at identified synapses to the molecules of their release apparatus (**Fig. 2.3** and **Suppl. Fig. 2.6**). Low frequency (0.2 Hz) motor nerve stimulation evoked transmission at only ~5% of synapses per stimulus (**Suppl. Fig. 2.7a,b**). P_r varied between synapses over a remarkable range of ~100-fold ($P_r = 0.005 - 0.610$) and half of the synapses (49.8 ± 1.8%; 2233 AZs from 16 NMJs) had a very low P_r (≤ 0.02) (**Fig. 2.3e**). Spontaneous transmission occurred at low rates (**Suppl. Fig. 2.7c**) with a maximal local spontaneous release frequency (F_s) of < 0.07 Hz, so that only ~0.5% of Ib synapses had a spontaneous event each second (**Suppl. Fig. 2.7d**). This extremely low spontaneous transmission frequency is consistent with findings in the intact, restrained animal[28]. We confirmed the large representation of low F_s and low P_r synapses in a second set of experiments, where we employed an alternative live imaging protocol (intermingling 100 stimuli to assess P_r with a total of 10 min of continuous imaging of spontaneous transmission) and replaced STORM with 3D Airyscan imaging[64] to also exceed diffraction-limited resolution and also image larger fields, thereby capturing larger numbers of synapses (**Suppl. Fig. 2.8**). Again, approximately half of the synapses had a $P_r \leq 0.02$ (56.4 ± 5.0%). The longer period of continuous imaging provided a better measure of spontaneous transmission, revealing a maximal F_s of 0.063 Hz at WT Ib synapses with an average F_s of 0.0042 ± 0.00011 Hz (2209 synapses from 7 NMJs).

In a previous study[33], we observed areas of the NMJ that lacked evoked transmission but showed spontaneous transmission, but, without a corresponding high-resolution view of synapse organization, we could not distinguish if these were individual AZs, clusters of AZs or non-synaptic sites where passing synaptic vesicle fuse spontaneously. Our current matching of AZ locations to QuaSOR transmission sites solved this problem and showed that 15.2 ± 1.5 % of AZs had no evoked transmission (during 200 APs; n = 2233 AZs from 16 Ib NMJs; QuaSOR-STORM matched). Our second experimental paradigm, which provided much longer observation time for spontaneous transmission (100 stimuli and 10 min spontaneous; n = 2209 AZs from 7 Ib NMJs; QuaSOR-Airyscan matched), showed that 24.8 ± 4.2% of AZs had no spontaneous activity. The majority of synapses with no evoked activity (over 100 stimuli) had spontaneous activity (67.4 ± 4.6%), indicating presence of functional postsynaptic glutamate receptors, and suggesting that these synapses have an extremely low P_r.

Dependence of AP-evoked transmission on Brp and Cac

To understand the presynaptic mechanisms that set transmission strength, we examined the relationship between AP-evoked transmission and the Brp/Cac content of the presynaptic AZ. We grouped synapses into five bins: evoked-undetected ($P_r < 0.005$) and four sets of evoked-active sites spanning the range of P_r ($P_r = 0.005\text{-}0.02$, $P_r = 0.02\text{-}0.035$, $P_r = 0.035\text{-}0.08$, and $P_r = 0.08\text{-}0.61$) (**Fig. 2.3e**). We found that P_r had a 5th power dependence on the normalized number of Cac localizations per AZ (**Fig. 2.3f**), consistent with the power dependence of quantal content on Ca^{2+} concentration[40,41]. P_r also had a super-linear dependence on Brp content (**Fig. 2.3g**) and Cac was sub-linearly dependent on Brp (**Fig. 2.3h**).

Beyond differences in the quantity of proteins at the AZ, differences in their nano-distribution may be an important diversifier of synaptic strength. *En face* synapses, binned according to P_r, were aligned to generate function-grouped spatial density averages (**Fig. 2.3i,j**). The densities of Cac and Brp increased with P_r (**Fig. 2.3k,l**), but the relative shape of their radial profiles remained remarkably constant (**Fig. 2.3m,n**). P_r had the same 5th power dependence on Cac within the 40 nm radius of the AZ core (**Suppl. Fig. 2.9a**) as seen for total Cac content across all AZ orientations (**Fig. 2.3f**).

We observed a strikingly large scatter in the 3-way relationship between Cac and Brp and P_r (**Fig. 2.3o**). Active synapses with very different P_r sometimes had similar levels of Cac and/or Brp, and synapses with no detected evoked transmission showed a wide range of Cac and/or Brp. Together Cac and Brp only explained ~31% of the variance in P_r (**Fig. 2.3o**). Thus, P_r depends on the quantities of Cac and Brp, but additional factors must also contribute as there remains a large scatter that is not accounted for by these two molecules.

In earlier work[28], before we increased the resolution of quantal transmission imaging with QuaSOR, we reduced the difficulty of resolving transmission at individual synapses by using a mutant of Rab3 (Rab3^{up}) that redistributes Brp into a smaller number of enlarged AZs, separated by greater distance. We now asked whether the altered Brp architecture in Rab3^{up} would influence the dependence of synaptic transmission on Brp and Cac. STORM imaging confirmed that the Rab3^{up} mutant has enlarged AZs (**Suppl. Fig. 2.5a, b**), with more Brp and more Cac at both Ib and Is AZs (**Suppl. Fig. 2.5c, d)** and a greater number of Cac clusters (**Suppl. Fig. 2.5a, b**). QuaSOR/STORM alignment between transmission sites and AZs was readily done in Rab3^{up} (**Suppl. Fig. 2.10a, b)**. We found that Rab3^{up} synapses have a higher average P_r and a broader P_r range than wildtype (**Suppl. Fig. 2.10c)**. As seen in wildtype, the F_s-P_r relation of Rab3^{up} was shallow, with little difference in spontaneous transmission frequency over a very wide range of P_r (**Suppl. Fig. 2.10e)**. Also as in wildtype, in Rab3^{up}, spontaneous transmission sites often lay between evoked sites (**Suppl. Fig. 2.10a)**. We found that, although it was spread over the wider P_r range, the relationship between P_r and Cac in Rab3^{up} had a similar power dependence to that seen in WT (**Suppl. Fig. 2.10d**). These observations are consistent with a mechanism that tunes Pr by regulating the size of the Brp scaffold and number of Cac channels and clusters.

Spontaneous and evoked quantal transmission are decoupled

Spontaneous and evoked transmission at individual synapses were positively related, but the relationship was extremely weak, with small changes in F_s over a wide range of P_r (**Suppl. Fig. 2.9b**). F_s depended on the quantity of both Cac (**Suppl. Fig. 2.9c**) and Brp (**Suppl. Fig. 2.9d**), but these relations were also shallow, in contrast to the steep power dependence of P_r on these proteins (**Fig. 2.3f,g**). These observations suggested differential molecular regulation of these two modes of release. To analyze this further, we compared the relative locations of spontaneous and evoked transmission events at *en face* synapses, across the P_r range (**Fig. 2.4a**). Radial profile analysis for evoked and spontaneous event densities showed that over an ~20-fold range in P_r, there were modest differences in spontaneous transmission density (**Fig. 2.4b-d**). In fact, the highest density of spontaneous activity was observed at very low P_r synapses (**Fig. 2.4d**). Beyond this quantitative mismatch, we also observed a striking spatial mismatch between sites of evoked and spontaneous transmission. Sites of spontaneous transmission were displaced to the periphery of sites of evoked transmission, with complete suppression of spontaneous transmission at evoked transmission maxima (**Fig. 2.4a-d**) and, consequently, a weak cross-correlation between radial profiles of spontaneous and evoked transmission (**Fig. 2.4e**).

To obtain an unbiased estimate of the degree of overlap between the locations of spontaneous and evoked transmission events throughout the NMJ, across synapse orientations, we performed a global QuaSOR event location pattern analysis. Based on previous analyses of spatial point processes[65], this provides a test for whether two sets of coordinates are statistically distinct spatially (see Methods). It is not an analysis of individual synapses, which would require longer stimulus trains, but a gestalt analysis of regions of the NMJ, which takes an event and computes a cumulative probability of another event within multiple radii. We found that coordinates of AP-evoked transmission events differed greatly from coordinates of spontaneous transmission events (**Fig. 2.4g,h**), confirming the spatial mismatch. In contrast, release patterns did not differ significantly between the first and second halves of the evoked stimulus train (**Fig. 2.4f,h**).

Thus, so far, we were able to align super-resolution QuaSOR maps of spontaneous and evoked transmission dynamics onto super-resolution STORM maps of AZ location, nanoarchitecture and protein content and thereby assess the possible contribution of AZ proteins to transmitter release. We observe a striking mismatch between sites of evoked and spontaneous transmission. We next sought to identify additional proteins that contribute to P_r diversity and spatial decoupling of transmission modes.

Complexin nano-distribution and transmission regulation

Our observation that Brp and Cac account for only part of P_r diversity suggested the involvement of other regulators of evoked release and the suppression of spontaneous transmission at the site of maximal evoked transmission suggested that one of these players could be a protein that inhibits spontaneous release. We therefore turned to Complexin (Cpx), which affects both modes of release across species, and strongly inhibits spontaneous release in *Drosophila*[48]. Cpx was found to be broadly distributed in both the Ib and Is axon (**Suppl. Fig. 2.11**) and enriched at the AZ, with Brp-associated Cpx levels 2-3 fold higher at Ib AZs relative to the AZs of Is axons that co-innervated the muscle (**Figs. 2.5a,b** and **Suppl. Fig. 2.12**). The widespread distribution throughout the bouton is consistent with partitioning of prenylated Cpx into endomembranes, including synaptic vesicles[66–69], which are more abundant in Ib boutons[70]. Analysis of 3D-STORM spatially-averaged *en face* AZs, showed that Cpx density was maximal at the Brp annular center (**Fig. 2.5c-f**), where Cac is concentrated (**Figs. 2.2** and **2.3**) and where electron tomography has shown that synaptic vesicles dock[71].

To determine the contribution of Cpx to transmission diversity, we performed QuaSOR imaging in conjunction with Brp/Cpx 3D-STORM. We took advantage of the 3D-STORM to focus on Cpx in the AZ by counting Cpx localizations within ~80 nm of the 3D distribution of Brp. Although Cpx acts as a brake on spontaneous fusion, we found that Cpx localizations in the AZ were weakly but positively correlated with F_s (**Suppl. Fig. 2.13a**). This may be accounted for by the association of Cpx with synaptic vesicles[66,67] and evidence that Cpx links vesicles to Brp[69]. Indeed, Cpx localizations were linearly related to Brp localizations (**Suppl. Fig. 2.13b**). Consistent with this observation, P_r increased supra-linearly with Cpx localizations (**Suppl. Fig. 2.13c**), as did P_r with Brp (**Fig. 2.3g**).

In an attempt to further isolate the effect of Cpx on the release machinery, we wanted to focus on the fraction of molecules that most likely interact with SNAREs. We therefore, further analyzed Cpx molecules located within the core 40 nm radius of the Brp annulus of *en face*-oriented AZs, the location where AP-evoked fusion most likely takes place[72]. Cpx in the AZ core was ~40% higher in Ib synapses compared to Is synapses (**Fig. 2.5g**), as was the Cpx/Brp ratio (**Fig. 5h**), suggesting that excess Cpx in the SNARE complex may inhibit evoked release.

We next asked whether differences in Cpx content of the AZ core could account for P_r differences between Ib synapses of the same axon (**Fig. 2.5i-m**). As seen in our experiments on Brp and Cac, where we measured total Brp at the AZ (**Fig. 2.3g**), Brp in the AZ core increased with P_r (**Suppl. Fig. 2.13d**). In contrast, Cpx in the AZ core was relatively constant across the wide range of P_r values (**Suppl. Fig. 2.13d**). In these *en* *face*-oriented AZs, both in the *x-y* plane (**Fig. 2.5m**) and along the *z*-axis (**Fig. 2.5n-q**), core Cpx/Brp ratio was *highest* in the weakest synapses (**Fig. 2.5r**).

Together, these results suggest that Cpx exerts two opposing effects on transmitter release, neither of which would be apparent with previous methodologies. On one hand, bulk Cpx appears to promote both spontaneous and evoked release, perhaps by interacting with Brp and synaptic vesicles near the release machinery. On the other hand, Cpx in the Brp annular core, where vesicles dock and fuse, appears to inhibit both spontaneous and evoked release. The spatial disconnect between spontaneous and evoked release (**Fig. 2.4a-d**) implies that the inhibition of spontaneous release is more potent, with complete suppression at the site of maximal evoked release where Cpx density is highest. We tested this notion next by knocking down Cpx.

Complexin suppresses both spontaneous and evoked transmission

To test the model that Cpx suppresses both evoked and spontaneous release and causes their spatial mismatch, we knocked-down Cpx in the motor neurons by expression of a Cpx^{RNAi} construct (UAS-Cpx^{RNAi} driven by the motor neuron-specific OK6-Gal4; “CpxKD”) (**Suppl. Fig. 2.11**). We imaged these NMJs continuously while stimulating the motor nerve electrically at 0.2 Hz (**Fig. 2.6; Suppl. Fig. 2.16b,c,e,f)**. As expected, given the known role of Cpx in *Drosophila*, there was a large increase in spontaneous transmission in CpxKD NMJs (**Fig. 2.6a-d**; **Suppl. Figs. 2.16a,d and 2.17c,d**). AP-evoked AZ participation **(Suppl. Fig. 2.12a-b**) was similar to that seen in WT Ib NMJs (**Suppl. Fig. 2.17b**). However, in the highly spontaneously active CpxKD Ib NMJs, ~7% of AZs had a spontaneous transmission event every second (**Suppl. Fig. 2.17d**), considerably above the frequency seen in control animals (**Suppl. Fig. 2.7d**). Alignment of spontaneous and evoked events with 3D-STORM (**Fig. 2.6g-n**) or 3D-Airyscan maps of Brp location provided a robust 1-1 mapping of synaptic properties.

This analysis was made possible by our ability to detect individual events because of their spatial segregation to different synapses. Electrophysiological measurement of transmission events in Cpx mutant animals is made difficult by the high frequency of spontaneous release, which is summed for the hundreds of synapses of the NMJ, and by the blending of transmission from Ib and Is synapses (**Fig. 2.6c and d, black traces**). In contrast, quantal imaging of transmission followed by QuaSOR analysis makes it possible to study Ib synapses one by one, where individual spontaneous transmission events are well separated in time, and in isolation from events at Is synapses. We recorded mEPSPs and EPSPs (bridge mode) or mEPSCs and EPSCs (two-electrode voltage clamp mode) simultaneously with imaging of quantal transmission, followed by QuaSOR analysis to compare WT to CpxKD. While, compared to WT, aggregate spontaneous transmission measured electrophysiologically in the CpxKD, occurred at a high frequency which made it difficult to distinguish and measure individual events (**Fig. 2.6a-d, black traces; Suppl. Fig. 2.14c, d**), transmission at individual sites measured optically was low enough (**Fig. 2.6g-n**) to allow individual transmission events to be readily resolved (**Fig. 2.6c and d, color traces**). We observed that average F_s was 10.7-fold higher at Ib synapses and 65.8-fold higher at Is synapses (**Fig. 2.7a** and **Suppl. Fig. 2.18a**). The number of synapses with no detected spontaneous events declined to almost zero in both Ib and Is axons of CpxKD animals (**Suppl. Fig. 2.18b**).

In contrast to the large increase in spontaneous transmission in the CpxKD, evoked quantal output (optical quantal density) and P_r at Ib synapses were similar to control (**Fig. 2.7b** and **Suppl. Fig. 2.18c,d**). We find that, compared to control, the CpxKD has a smaller amplitude EPSC (**Suppl. Fig. 2.14e, f**). We wondered if this were due to a reduction in the number of synapses, quantal size or P_r. Our analysis revealed no effect of the CpxKD at either Ib or Is synapses on either AZ density (**Suppl. Fig. 2.18e**) or P_r (**Fig. 2.7b; Suppl. Fig. 2.18d**). However, the CpxKD had smaller amplitude spontaneous single synapse optical events at both Ib and Is synapses (**Suppl. Fig. 2.15**). Thus, reduced quantal size appears to contribute to the reduction in EPSC amplitude in the CpxKD.

Therefore, the lack of an effect on P_r, in light of the reduction in levels of the release-promoting Brp, suggested that knockdown of Cpx had an offsetting effect, i.e. that Cpx generally suppresses evoked release. We tested this idea by examining the effect of the CpxKD on the dependence of P_r on Brp. Strikingly, the P_r-Brp relation shifted to the left in the CpxKD Ib NMJ (**Fig. 7c**), yielding higher P_r for the same Brp levels. This also meant that AZs with low Brp, which were had no detected evoked transmission in control animals, were active in CpxKD animals. Thus, Cpx appears to suppress evoked release and this inhibitory effect in Cpx mutants and KDs may have not been recognized earlier because of a compensatory reduction in the Brp content of AZs.

Knockdown of Complexin eliminates the mismatch between spontaneous and evoked transmission

We wondered whether knockdown of Cpx would eliminate the quantitative mismatch between AP-evoked and spontaneous release. We found that the very shallow relation between F_s and P_r in WT and Rab3 mutant NMJs (**Suppl. Figs. 2.9b** and **2.10e**) was increased to near unity in slope in CpxKD animals (**Fig. 2.7d,e; Suppl. Fig. 2.19c**). Moreover, the very weak dependence of F_s on Brp in WT and control Ib synapses (**Suppl. Figs. 2.8c** and **2.14b**) increased greatly in the CpxKD (**Fig. 2.7f** and **Suppl. Fig. 2.19d**). Together, these observations suggest that, in the absence of Cpx, the AZ scaffold functions as a common, powerful determinant of both spontaneous and evoked release.

Strikingly, we found that knock-down of Cpx eliminated the spatial mismatch between transmission modes. The suppression of spontaneous transmission at the site of maximal evoked transmission disappeared, yielding similar spatial profiles in the CpxKD across P_r for *en face*-oriented AZs (**Fig. 2.7h-j**) and the highly significant difference between the spatial distribution of spontaneous and evoked QuaSOR events of WT Ib NMJs (**Fig. 2.4e**) gave way to statistically indistinguishable global spatial distributions of spontaneous and evoked QuaSOR events in CpxKD Ib NMJs (**Fig. 2.7k-m**). Thus, Cpx appears to suppress both spontaneous and evoked release, but to more strongly suppress spontaneous release, and this unequal suppression results in a quantitative and spatial mismatch between spontaneous and evoked transmission within the wildtype AZ.

Discussion

To understand the mechanisms that regulate synaptic strength and generate synapse diversity, we set out to develop a new set of super-resolution imaging tools that together would allow us to relate quantal transmission to presynaptic molecular composition in an intact model synapse. Imaging of Ca^{2+} influx through ionotropic glutamate receptors, with a postsynaptically-targeted reporter, provided a quantal-resolution proxy for the EPSC, and QuaSOR analysis increased spatial resolution sufficiently to resolve synapses even in dense areas of the *Drosophila* NMJ. QuaSOR makes it possible to determine P_r directly by failure analysis under physiological Ca^{2+}, i.e. at physiological P_r, avoiding reliance on estimation based on the ratio between evoked and spontaneous EPSC amplitudes (problematic in view of our finding that the sites of evoked and spontaneous transmission are segregated within the synapse), fits of amplitude distributions or analysis of variance[73,74]. *Post-hoc* super-resolution presynaptic axon reconstructions enabled us to correlate transmission to the molecular composition and nano-architecture of the presynaptic AZ for thousands of synapses.

Earlier work suggested that, despite a common history of activity and postsynaptic target, transmission varies greatly between the synapses of a single Ib motor axon[28–31,33,34]. QuaSOR assignment of transmission events to identified synapses showed this to be the case across thousands of synapses and revealed that the heterogeneity is even greater than previously thought, with P_r ranging over at least 100-fold, from <0.005 to 0.6. Half of the synapses are very weak ($P_r < 0.02$) and AP-evoked transmission is dominated by a small fraction of higher P_r synapses during low levels of activity. This large pool of low-P_r synapses could operate as a reserve that would be recruited to sustain transmission during long, high frequency AP bursts, such as occur during locomotion[28,75].

Previous studies at the NMJ demonstrated a positive relationship between P_r and both Cac[29,30] and Brp[32–34]. The ability to relate quantal transmission to multi-color 3D-STORM clarifies the nature of this relationship, by showing that P_r increases with the ~5th power of Cac, both in wildtype synapses and in synapses of a Rab3 mutant whose AZs are enlarged, consistent with the power-dependence of release on Ca^{2+} [41,42,76]. Cac and Brp levels were also correlated with one another, consistent with Brp recruiting Cac to the AZ[44]. Although they are strong determinants, Cac and Brp only account for a fraction of the variance of P_r, indicating that other factors are at play. When AZs were expanded by the Rab3 mutant to include more Brp and Cac, P_r increased to higher values, while maintaining the shallow F_s-P_r relation, the displacement of spontaneous transmission to locations outside the sites of evoked and the high power dependence of P_r on Cac. These observations are consistent with a mechanism that tunes P_r by regulating the size of the Brp scaffold and number of Cac channels.

In considering other potential regulators of presynaptic strength, we remarked on an almost complete lack of correspondence between evoked and spontaneous transmission in WT animals. Most startlingly was a complete suppression of spontaneous transmission at the site of maximal evoked transmission. This segregation is only possible to detect with these analysis tools and agrees with evidence from use-dependent block that spontaneous and evoked release activate distinct populations of glutamate receptors in hippocampal neurons[78] and the *Drosophila* NMJ[33]. Our observations reveal that this separation arises not only from synapse specialization, as proposed in earlier studies, but from physical segregation of evoked and spontaneous transmission *within* the synapse. This spatial mismatch is remarkably consistent with recent iGluSnFR mapping of spontaneous and evoked transmission events in cultured hippocampal synapses[52], suggesting that segregation of transmission modes within the synapse may be a general phenomenon.

We considered that a factor that regulates both spontaneous and evoked release could be responsible for their spatial mismatch. We turned to Cpx, which has been shown to regulate both spontaneous and evoked release in complicated and contradictory ways[48]. *In vitro*, Cpx interacts with the coiled-coiled domains of the SNARE complex to inhibit fusion and is displaced by Ca^{2+}-bound synaptotagmin to trigger AP-evoked release[79–81]. The mammalian isoforms of Cpx contain both fusogenic and inhibitory domains[48,82]. Pan-neuronal removal of Cpx in *Drosophila* reduces postsynaptic response amplitude, suggesting that Cpx promotes evoked release[47,82–84]. In contrast, expression of *Drosophila* Cpx in mammalian neurons suppresses evoked release[82]. Cpx may also adjust the relationship between release and internal Ca^{2+} concentration through its role as an adapter that helps determine the composition of the release apparatus[16,18,48]. We find that Cpx is broadly distributed in the axon, enriched at the AZ and most densely concentrated in the Brp annular core. As the Cpx/Brp ratio within the AZ core rises, the P_r of Ib synapses decreases. This suggests that Cpx in the AZ core, which is positioned to interact with SNARE complexes, inhibits evoked release. Consistent with this relationship, Cpx knockdown increases the dependence of P_r on Brp so that at equivalent Brp levels P_r is higher when Cpx is knocked down and low Brp synapses with no detected transmission events become active.

Knockdown of Cpx increased F_s by ~11-fold at Ib synapses and ~66-fold at Is synapses, indicating that Cpx suppresses spontaneous transmission more strongly than evoked transmission. In light of this and of our findings that: a) Cpx density is highest in the Brp annular core, where Cac is also located, and where AP-evoked vesicle fusion is therefore expected to take place, b) spontaneous transmission is suppressed at the site of maximal evoked transmission, c) spontaneous and evoked transmission are poorly correlated and d) knockdown of Cpx eliminates the spatial and quantitative mismatch between spontaneous and evoked transmission, we propose that Cpx within the AZ core partly suppresses evoked release and completely suppresses spontaneous release. This differential suppression can preserve vesicles that are docked near Ca^{2+} channels in a state that is ready for release when the AP arrives, yielding a higher signal-to-noise for AP-evoked transmission over background spontaneous transmission.

It is striking how knockdown of Cpx converts the relationship between P_r and F_s to near 1:1 and the spatial relationship of spontaneous and evoked transmission to coincident. This suggests that spontaneous and evoked release rates are, after all, governed by common factors. Brp levels were reduced in the CpxKD, possibly reflecting a compensatory mechanism that keeps the P_r of Ib synapses at near WT levels, as shown in recent focal extracellular recordings from Ib boutons[85]. While Cpx in the Brp annular core suppresses P_r, we find that higher bulk Cpx around the AZ is associated with higher P_r. This bulk Cpx likely reflects prenylated Cpx that is associated with endosomes and synaptic vesicles[66,67], which links vesicles to Brp[69], and so may reflect higher vesicle content.

Together, QuaSOR and super-resolution molecular imaging of AZs reveal that the balance between the quantity and nanoscale localizations of Cac, Brp and Cpx contribute to a wide diversity in release dynamics for synapses that otherwise share common pre-post pairing and activity history. This heterogeneity could serve to maintain a deep pool of reserve synapses upon which the system can draw under diverse physiological demands.

Methods

Drosophila Husbandry and Genetics

Several flies were obtained from the Bloomington Drosophila Stock Center (BDSC) including; attP40^{Empty} (BDSC Line 36304), UAS-Cpx^{RNAi} (pVALIUM20 vector; inserted into attP40; BDSC Line 42017), UAS-Cpx (BDSC Line 39743), UAS-Cac^{RNAi} (pVALIUM10 vector; inserted into attP2; BDSC Line 27244) and UAS-Dcr2 (BDSC Line 24648). OK6-Gal4 [86] and SynapGCaMP6f (3rd chromosome MHC-CD8-GCaMP6f-Sh) lines were reported previously [28,33]. Flies were raised on standard corn meal and molasses media at 25 ºC. Female wandering third instar larvae were used in all experiments. Only actively crawling larvae were used for experiments. When required, third instar larvae were screened using a Zeiss Axio Zoom.V16 microscope (Carl Zeiss, Inc. Oberkochen, Germany) through the use of balancers with larval markers including CyO^{GFP} (3xP3-EGFP variant) and TM6B. All larvae contained a single copy of SynapGCaMP6f on the 3rd chromosome. The following genotypes were used: WT (w^{1118}; +/+; SynapGCaMP6f/+), Control (w^{1118}; OK6-Gal4/attP40^{Empty}; SynapGCaMP6f/+), CpxKD (w^{1118}; OK6-Gal4/UAS-Cpx^{RNAi}; SynapGCaMP6f/+), CpxOE (w^{1118}; OK6-Gal4/+; UAS-Cpx/SynapGCaMP6f) and CacKD (UAS-Dcr2/w^{1118}; OK6-Gal4/+; UAS-Cac^{RNAi}/SynapGCaMP6f).

SynapGCaMP6f Optical Quantal Imaging

Optical quantal imaging was performed similarly to our previous report[28]. Briefly, third instar larvae were dissected on PDMS (Sylgard 184, Dow Corning, Auburn, MI) pads in ice-cold HL3 solution containing, in mM: 70 NaCl, 5 KCl, 0.45 $CaCl_2 \cdot 2H_2O$, 20 $MgCl_2 \cdot 6H_2O$, 10 $NaHCO_3$, 5 trehalose, 115 sucrose, 5 HEPES, and with pH adjusted to 7.2. Following removal of the brain, larval fillets were washed and imaged in room temperature HL3 containing 1.5 mM Ca^{2+} and 25 mM Mg^{2+}. Fluorescence images were acquired at room temperature with a Vivo Spinning Disk Confocal microscope (3i Intelligent Imaging Innovations, Denver, CO), using a 63x 1.0NA water immersion objective (Zeiss), 1.2X optical adapter, LaserStack 488nm (50 mW) laser, CSU-X1 A1 spinning disk (Yokogawa Tokyo, Japan), standard GFP filter, and EMCCD camera (Photometrics Evolve512, Tucson, AZ). All live SynapGCaMP6f imaging recordings were done on ventral longitudinal abdominal muscle 4 at segments A3-A5 of third instar larvae. All imaging was performed using 50 ms exposures (20 fps) of the full camera sensor (512x512 px) with the exception of **Suppl. Fig. 2.1a-f,** which was acquired with 20 ms exposures (50 fps).

Nerve stimulation was performed with a suction electrode attached to a Stimulus Isolation Unit (SIU, ISO-Flex, A.M.P.I Jerusalem, Israel) with 100 µs stimulus duration.

Stimulation intensity was adjusted to recruit both Ib and Is axons, as verified during the imaging. Nerve stimulation and imaging were synchronized using custom-written MATLAB scripts (MATLAB Version 2015b, MathWorks, Inc., Natick, MA) in order to control the SIU and trigger imaging episodes within SlideBook (v6.0.16, 3i Intelligent Imaging Innovations).

To gather spontaneous and evoked transmission events at each NMJ, two separate quantal imaging experimental protocols were utilized. In the sequential protocol, we collected AP-evoked responses during short, single-stimulus episodes. Here each stimulus was collected during a series of 10 images (50 ms exposures). Each episode had 3-4 baseline frames prior to nerve stimulation. We collected a minimum of 200 single-stimulus episode trials at 0.2 Hz. This was followed immediately by spontaneous event collection, imaging continuously at 20 FPS (50 ms exposures in streaming capture mode) for 2 minutes total separated into four, 30 s movies. These brief pauses between movies allowed for the manual correction of any drift in the NMJ. In the second interleaved activity imaging protocol, both spontaneous and evoked events were collected during the same image acquisition protocol. This was done by imaging continuously at 20 FPS (50 ms exposures in streaming capture mode) for 30 s while stimulating the nerve 5 times with 5 s intervals during each 30 s movie. Minor focusing adjustments were made between movies with a maximum of 10 s between movies. A minimum of 20 movies were captured per NMJ for an overall protocol of 600 s of imaging with 100 stimuli.

To ensure comparability between experiments, recordings were done on only one NMJ per larva (i.e. the number of NMJs = the number of larvae) in recordings that were performed within 30 min of the beginning of the dissection, thereby ensuring health and similar conditions. To determine whether we could pool results from segments A3, A4 and A5, we analyzed recordings from WT animals from A3 (n=9), A4 (n=11) and A5 (n=13) and compared their properties (**Suppl. Table 2.1**), we found no significant difference between Ib synapses in the three segments in the following key parameters: a) Quantal density, b) Average Pr, c) Brp STORM localizations per AZ and d) normalized Brp per AZ (**Suppl. Fig. 2.20**).

SynapGCaMP6f Registration and Bleach Correction

The initial quantal image analysis was performed using custom-written MATLAB routines similar to previous work[28]. In the case of the episodic evoked imaging protocol, individual stimulus episodes were excluded due to out of focus NMJs, moving NMJs or failed axon recruitment. Otherwise, all movies were filtered (Gaussian low-pass filter), to reduce high-frequency noise. Image analysis areas were then separated into Ib and Is NMJ regions according to their baseline SynapGCaMP6f fluorescence. All imaging data were registered using a multi-stage approach, during which all images were registered to a common reference image, even when multiple imaging modes were applied. This was either the first image of the first episode for the episodic imaging protocol, or an average image of the first 20-30 frames of the first movie for spontaneous-only and interleaved spontaneous/evoked protocols. The later method was required due to the inclusion of the highly spontaneously-active CpxKD animals where, due to the high rates of spontaneous release, there are often no single frames without at least one spontaneous event in the movie.

Following area selection and reference image selection, NMJs were tracked relative to this reference image using a rigid subpixel registration method to remove any large movements within the NMJ imaging area[28,87]. To correct for local bouton movements and small NMJ shape changes, we used a custom diffeomorphic implementation of a demons algorithm[88], similar to our previous *in vivo* image registration[28]. Here we enhanced the contrast of the NMJ and calculated a displacement field for each image pair (each image relative to the reference image). This method can generate localized movement artifacts, so we applied a temporal filter for each pixel's displacement vector over time, prior to applying the respective displacement field to each image. This ensured smooth tracking of each bouton over long imaging times. In the case of episodic evoked imaging protocols, only the first image of each 10 image-single stimulus movie was used to calculate the corrections for the whole episode. For all 30 s continuous imaging datasets, registration transformations were calculated on every image of the movie relative to a common reference image.

Once motion corrected, movies were bleach corrected using two methods. In the case of the episodic AP-evoked imaging protocols, we fit a double exponential bleach correction curve to the mean baseline pre- and post-stimulus fluorescence data for each trial separately. Spontaneous or interleaved spontaneous/evoked movies were bleach corrected by adjusting the images according to a moving average (across 20 frames) of the mean fluorescence values for the whole NMJ analysis region. Following bleach correction, both ΔF and $\Delta F/F$ movies were generated using the first image as the baseline fluorescence (F_0) image for the episodic data. An average minimum intensity image across the first 30 frames of each 30 s movie was used as the baseline image (F_0) for the other imaging protocols. This method made it possible to eliminate the contamination of the ΔF or $\Delta F/F$ signals throughout the movie by spontaneous events present during the baseline images.

Quantal Event Detection

We employed a template fitting approach to identify all quantal responses for both AP-evoked and spontaneous experiments. For episodic evoked imaging data, due to the synchronous nature of the evoked responses, a single ΔF response template was utilized according to the average temporal profile for all evoked responses at that NMJ. For spontaneous-only or evoked/spontaneous interleaved protocols, we employed a multiple ΔF response template fitting approach to accommodate responses that may not align perfectly to a single ΔF response template. Similar to our approach described previously [28], each pixel's temporal response was analyzed independently to determine if it had a high degree of correlation with the template response(s), as determined by the degree of cross-covariance. These highly correlated pixels and frames were then flagged as active if they had $\Delta F/F$ amplitudes that were above a minimum threshold (typically between 0.04 - 0.05 $\Delta F/F$) and at least 1.5 to 2 times larger than the standard deviation of the values at that pixel. When multiple templates were utilized, the best fitting template was determined according to the maximum cross-covariance found between the data and each template. We also maintained a minimum allowable time between subsequent events at each pixel (100 ms) to prevent over-fitting. Co-active pixels were then grouped together into a single response field. This produced a single, isolated, maximal temporal projection image of the response's spatial profile. To eliminate false positives, we applied size, shape, and amplitude thresholds to these response fields. For the spontaneous-only datasets, responses were further manually validated according to their shape and temporal profile. For the simultaneous spontaneous and evoked datasets, we used a common event detection process for both classes of events together. Following detection processing, events were sorted into the appropriate category using the timing of the response relative to the stimulus timing. Only a 200 ms window, following each AP, was used to assign evoked responses.

Quantal Synaptic Optical Reconstruction (QuaSOR)

After event detection, isolation and verification, we then proceeded to analyze the 2D response profile of each event's maximum ΔF/F spatial profile using the custom QuaSOR algorithm. We took all identified responses and first isolated small ROIs containing individual or small groups of partially overlapping response fields that corresponded to individual or small groups of events. These smaller ROIs were then subjected to independent 2D Gaussian mixture model fitting of the isolated ΔF/F spatial profiles. For each smaller ROI, we generated a large number of test models using a maximum likelihood Expectation-Maximization algorithm. This allowed us to test a wide number of Gaussian mixture model components (1-8) so that we could identify multiple quantal events per ROI. Each set of Gaussian mixture model component also had multiple test fit replicates (20-200) utilizing randomized starting conditions to ensure adequate coverage of the parameter space for each ROI. Each 2D Gaussian mixture model was then scored according to a number of features. This included the number of components (too many components were penalized to prevent over fitting, especially during spontaneous recordings), the distance between the peaks of each component (below a minimum distance was penalized), and the normalized 2D cross-correlation with the input ROI ΔF/F response spatial profile. We also used a large set of manually validated spontaneous quantal event, single component, 2D Gaussian fit models to define distributions for known single quantal peak amplitudes, 2D Gaussian variances, 2D Gaussian variance differences, and 2D Gaussian covariance components. These distributions of validated Gaussian profiles were used to score each test model to ensure that the fitting within each mixture model was generating appropriately sized and shaped 2D Gaussian profiles. Finally, the scores for each fit model were tabulated and the best mixture model was determined for each response ROI. This method provides >90% fitting accuracy relative to a manual fit assessment.

Following 2D Gaussian mixture model fitting for all response ROIs, all event functions were then remapped onto a common coordinate space and merged to define a single set of 2D Gaussian functions for each quantal response. The peak positions of each 2D Gaussian component were used to define event locations in a 21.2 nm x 21.2 nm pixel coordinate space. For visualization purposes, maps were generated by applying a normalized 2D Gaussian filter to each event coordinate prior to adding each event to the overall image. In this way each pixel contains an approximation of the event density at that location. The corresponding filtering parameters, as well as colorbars that indicate event counts per pixel, are indicated in the respective figures and/or figure legends. To facilitate AZ matching we sometimes reoriented the QuaSOR data by rotating and translating all the coordinates prior to re-rendering the maps to match the STORM or

Airyscan data. In all images, gray masked areas indicate where NMJs were either rotated and/or isolated for analysis and display purposes.

QuaSOR Quantification

Local QuaSOR synapse alignments were performed by identifying maximum evoked coordinate density positions for synaptic ROIs within a 350 nm radius. Maintaining their relative organization to nearby events, these QuaSOR event coordinates were averaged together with other synapses to generate a mean density image for synapse groupings. Images were rendered using the parameters indicated in the figure legends. In this way, the relative position of QuaSOR events was preserved, including between evoked event and spontaneous event datasets. Average QuaSOR density radial profiles were then calculated by binning local QuaSOR event counts into 10 nm annuli surrounding the center alignment position, with total counts being normalized to the area of each annulus to provide an average QuaSOR event density per radial bin. The synaptic clustering of QuaSOR coordinates was compared to coordinates derived from the pixel-maxima method in which each event was identified by maximal ΔF/F pixel location [28]. Evoked localizations within each method were summed to construct localization density maps for the entire NMJ so that the two methods could be compared (**Suppl. Fig. 2.1k,m**). Each map was fit with a 2D Gaussian model using a non-linear least-squares regression (**Suppl. Fig. 2.1l,n**) and used to calculate the average half-maximum evoked cluster area and average evoked event cluster full width at half-maximum (FWHM) (**Suppl. Fig. 2.1k-n**). We found the AP-evoked type Ib QuaSOR cluster FWHM to be 236.8 ± 5.6 nm, whereas the pixel-maxima FWHM was 464.6 ± 7.8 nm for the same NMJs (n = 45 NMJs) (**Suppl. Fig. 2.1o**). This represents an estimated 3.8-fold improvement in resolution by QuaSOR.

On its own, in absence of molecular imaging of AZ locations, synapse assignment in QuaSOR is not certain and could merge transmission events from neighboring synapses in regions of high synapse density. We therefore focused our study on NMJs where QuaSOR maps were related to molecular imaging maps generated in either STORM or Airy. Given the FWHM of 237 nm for QuaSOR, we added a safety margin and excluded areas of the NMJ where the distance between molecularly mapped AZs was <350 nm. Linear uniform global transformations in the x and y axes were applied to adjust for stretch of the tissue that occurred after the live optical quantal imaging during fixation and mounting on slides under cover glass for molecular imaging, yielding images in which QuaSOR transmission sites could be matched to STORM AZs (**Suppl. Fig. 2.6a-f**). After these global corrections, QuaSOR-STORM correspondence had an average QuaSOR-STORM offset correction of 257.0 ± 9.5 nm **(Suppl. Fig. 2.6i**), with a matching success rate of ~85% (**Suppl. Fig. 2.6h**). This offset represents the average distance discrepancies of neighboring AZs when comparing the same AZ pairs between their QuaSOR and STORM locations. Therefore, the alignment and matching steps are highly accurate in preserving the relative organization of synapses throughout the NMJ. The spatial alignment between QuaSOR and STORM is further illustrated in several example boutons from different NMJs at high magnification in **Suppl. Figure 2.6g.** It is worth noting that, some AZs contain more than one Cac or Brp cluster (**Fig. 2.3a,i; Suppl. Fig. 2.5a**). Although it is not known if these constitute more than one release site in the single AZ, their close proximity within the AZ meant that they could not be resolved with QuaSOR, so that each AZ was treated as a synaptic unit.

To assess the relative co-localization between different sets of QuaSOR coordinates, we adapted a technique for the analysis of ecological point pattern processes[65]. Briefly, nearest neighbor distances were calculated between all events and two comparisons were utilized: (1) evoked event locations released during the first half of a stimulus train were compared to those released during the second half of the train or (2) all evoked coordinates were compared to all spontaneous event coordinates. Using these nearest neighbor distances, an O-ring statistic was computed. This O-ring statistic used transformed distances between points as a proxy for event location. An empirical cumulative distribution function of transformed distances between points was then calculated and a two-sample Cramér–von Mises test was employed to examine differences in transformed distances between the comparison groups. Statistically significant differences in transformed distances between conditions likely indicated a distinct underlying point process for the coordinate sets.

Single synapse AP-evoked transmission probability (P_r) was determined by dividing evoked event counts within the single AZ domain by the number of motor nerve stimuli (P_r = # stimulus-coupled optical events per synapse / # stimuli; ranging from 0 to 1). Spontaneous transmission frequency (F_s) was calculated for the total imaging time (F_s = # spontaneous optical events per synapse during a period with no stimulation / imaging time; in Hz).

Antibodies and Immunohistochemistry

Larvae were fixed in room temperature Bouin's fixative (Ricca Chemical Company, Arlington, TX) for 5 minutes, permeabilized in PBS with 0.1% Triton X100 (PBT) and blocked in PBS with 0.1% Triton X100, 5% normal goat serum, and 0.02% sodium azide (PBN). All antibody incubations were performed in PBN and all washes were performed in PBT. Mouse anti-Brp (nc82; Developmental Studies Hybridoma Bank, Iowa City, IA) was used at 1:100 for confocal and Airyscan imaging, while it was used at 1:1000 for STORM imaging. Rabbit anti-Cpx antibody[47] was used at 1:2000. Chicken anti-GFP (Thermo Fisher A10262; Thermo Fisher Scientific Waltham, MA) was used at 1:1000 to label SynapGCaMP6f in fixed samples. Rabbit anti-Cac antibody[57] was used at 1:1000. Alexa Fluor 647 (Jackson 123-605-021) and Cy3-conjugated goat anti-Hrp (Jackson 123-165-021; Jackson ImmunoResearch Laboratories, West Grove, PA) antibodies were used at 1:250. Alexa Fluor 405 goat anti-mouse (Thermo Fisher A31553), Alexa Fluor 488 goat anti-chicken (Thermo Fisher A11039), Alexa Fluor 488 goat anti-rabbit (Thermo Fisher A11008), Alexa Fluor 555 goat anti-mouse (Thermo Fisher A32727), Alexa Fluor 568 goat anti-rabbit (Thermo Fisher A11036), Alexa Fluor 647 goat anti-rabbit (Thermo Fisher A32733), and Alexa Fluor 647 goat anti-mouse (Thermo Fisher A21235) secondary antibodies were all used at 1:1000. For the labeling of the anti-Cac primary antibody, we used goat, anti-rabbit Biotin $F(ab')_2$ (Jackson 111-066-144) at 1:1000, followed by Streptavidin-647 (Thermo Fisher S32357) at 1:500[57].

CF680 goat anti-mouse secondary antibody was conjugated in house and used at 1:1000. Briefly, CF680 NHS ester (Biotium Inc. Fremont, CA) was dissolved at a concentration of 3 mM in anhydrous DMSO. 1 µL of dye solution, 80 µL of a 1.25 mg/mL suspension of unlabeled goat anti-mouse IgG1 secondary antibody (Jackson 115-005-

205), and 10 µL of 1 M sodium bicarbonate solution were mixed and allowed to react for 15 min at room temperature. The reaction mixture was added to an equilibrated NAP-5 column (Sigma GE17-0853-01; Sigma-Aldrich St. Louis, MO) and flushed with PBS. The dye conjugated antibody was collected from the first colored eluent fraction and a concentration of 0.12 mg/mL was determined with a NanoDrop spectrophotometer (Thermo Fisher).

Antibodies obtained from the Developmental Studies Hybridoma Bank were developed under the auspices of the National Institute of Child Health and Human Development of the National Institutes of Health and maintained by the Department of Biological Sciences of the University of Iowa, Iowa City, IA. We confirmed the specificity of the Cac antibody by comparing staining in control animals and Cac RNAi (**Suppl. Fig. 2.3a**). We confirmed the specificity of the Cpx antibody by comparing staining in control animals with both Cpx RNAi (Cpx KD) and Cpx over-expressing (Cpx OE) animals (**Suppl. Fig. 2.11**). With both Cac and Cpx, the RNAi knocked down staining to a large extent, although not completely, consistent with what is often observed with other RNAis. To obtain uniformity in antibody staining, we fixed and stained the different genotypes compared within an experiment simultaneously with the same reagents.

Confocal and Airyscan Imaging and Analysis

Following antibody incubations and washes, larval fillets were mounted in Vectashield (H-1000; Vector Laboratories, Burlingame, CA) or Vectashield HardSet (H-1400). Confocal and Airyscan imaging were performed on either a Zeiss LSM 880 or Zeiss LSM 980 microscope. All samples were imaged with a 63x oil immersion objective (NA 1.4, DIC; Zeiss) using Zen software (Zeiss Zen black 2.3 SP1). All imaging data were collected using identical imaging and processing parameters for a given experiment set. Unless otherwise noted all confocal and Airyscan images are displayed as Gaussian filtered maximum intensity projections that were generated using custom-written MATLAB routines.

Confocal imaging data were acquired as *z* stacks with images of 2048 by 2048 px, at 1.2x zoom, with *x-y* pixel size of 55 nm, axial *z* spacing of 368 nm, 1 µs pixel dwell and 2x pixel averaging. Different channel data were acquired using custom wavelength cutoffs. Alexa Fluor 405 was excited with a 405 nm laser and data were acquired from 410-455 nm with a pinhole of 56.7 nm. Alexa Fluor 488 was excited with a 488 nm laser and data were acquired from 493-539 nm with a pinhole of 67.7 nm. Alexa Fluor 568 was excited with a 561 laser and data were acquired from 565-620 nm with a pinhole of 77.0 nm. Alexa Fluor 647 was excited with a 647 nm laser and data were acquired from 648-713 nm with a pinhole of 67.7 nm. Channels were scanned sequentially with the exception of Alexa Fluor 488 and Alexa Fluor 647 where data were acquired simultaneously. Quantification of average ROI intensities were calculated on terminal sets of 2-3 boutons using maximum intensity *z* projection images and background corrected using an ROI over the muscle area and adjacent to the boutons.

Airyscan imaging data[64,89] were acquired using a tiling strategy, whereby smaller volumes of each an NMJ were acquired sequentially and stitched together. Brp reconstructions for matching to QuaSOR data were acquired on the LSM 880 system. Briefly, each imaging volume was acquired with an additional magnification of 12x with a 5 AU pinhole, 2 µs pixel dwell times, line averaging of 2, an *x-y* dimension of 1024 by

1024 px (processed to 1000 by 1000 px) at 11 nm/px and axial *z* spacing of 159 nm. Each of the three channel volumes (anti-Brp/Alexa 405, anti-GFP/Alexa 647, and anti-Hrp/Cy3) were scanned sequentially. Alexa 405 was excited with a 405 nm laser and data were acquired with a BP420-480-LP605 filter. Alexa 488 was excited with a 488 nm laser and data were acquired with a BP495-550+LP570 filter. Cy3 was excited with a 561 laser and data were acquired with a BP495-550+LP570 filter. Additional Brp intensity quantification data were acquired on an LSM 980 system with 4x magnification, a 5 AU pinhole, 0.66 µs pixel dwell times, an *x-y* dimension of 792 by 792 px (processed to 768 by 768 px) at 43 nm/px and axial *z* spacing of 160 nm. Here anti-GFP/Alexa 488 and anti-Brp/Alexa 555 were excited with 488 nm and 561 nm lasers respectively and data were acquired with a SP615 filter.

Airyscan processing of all channels and *z* slices were performed in Zen (Zeiss Zen Black v2.3 SP1) using super-resolution settings. We then sequentially stitched each 4D volume together in Fiji (NIH ImageJ Version 2.0.0-rc-43/1.52n) using pairwise stitching with linear blending [90]. Alignments were performed to maximum intensity pixels of Brp puncta in overlapping volumes. Regions outside of the tile borders are always indicated by gray coloring in the corresponding images.

AZ locations in stitched Airyscan datasets were calculated by masking the volumetric Brp data. Sites were initially identified using a local 3D Brp intensity maxima with a minimum distance of 150 nm from neighboring maxima. AZ identifications were manually validated and corrected when neighboring sites were misidentified. AZ-specific Brp voxel intensities were calculated by identifying 3D connected voxels to each AZ maxima for isolated AZs. To avoid artifacts of stitching and bleaching of overlapping regions, pixel quantifications were collected using the original image pixel intensity information, prior to stitching, with intensity values calculated from 3D voxel AZ masks.

STORM Imaging and Analysis

STORM imaging was performed on a homebuilt setup based on a modified Nikon Eclipse Ti-E inverted fluorescence microscope using a Nikon CFI Plan Apo λ 100x oil immersion objective (NA 1.45), as previously described[91]. Briefly, dye-labeled samples were mounted with imaging buffer [5% (w/v) glucose, 140 mM cysteamine, 0.8 mg/mL glucose oxidase, and 40 µg/mL catalase in 1 M Tris-HCl, pH 7.5][53,54] and sealed with Cytoseal 60. Conventional epifluorescence imaging of 560 nm (anti-Hrp Cy3) and 488 nm (anti-GFP Alexa Fluor 488) dyes was performed immediately prior to STORM imaging using the appropriate laser and filter set and served as reference for alignment with QuaSOR data. Alexa Fluor 647 and CF680 dye molecules were photoswitched to the dark state and imaged using a 647 nm laser (MPB Communications, Montreal, CAN). All lasers were introduced through an optical fiber into the back focal plane of the microscope and onto the sample at intensities of ~2 kWcm^{-2}. These lasers reached the sample at incident angles slightly smaller than the critical angle, thus illuminating a few micrometers into the sample. Weak (~0.1 Wcm^{-2}) 405 nm laser illumination was used to further assist photoswitching of single molecules. The resultant single-molecule fluorescence was recorded with an EM-CCD (Andor iXon Ultra 897; Oxford Instruments Abingdon, United Kingdom) at 110 frames per second, for a total of ~70,000 frames per image. A cylindrical lens (f = 1 m) was inserted into the imaging path to encode the depth (*z*) information into the single-molecule image shape[54]. The raw STORM data were analyzed according to previously described methods[53,54].

Single-color 3D-STORM was performed using only Alexa Fluor 647 (Brp), while two-color 3D-STORM imaging was performed with Alexa Fluor 647 (Cac or Cpx) and CF680 (Brp in two-color mode). For two-color imaging with 647 nm excitation, a ratiometric detection scheme[55,56,92] was employed to concurrently collect the emission of Alexa Fluor 647 and CF680 single molecules. Emission of these dyes was split into two light paths using a long pass dichroic mirror (T685lpxr; Chroma Technology Bellow Falls, VT), each of which was projected onto one half of the EM-CCD camera. Dye assignment was performed by comparing the intensity of each single molecule in the two channels. Proper localization assignments in this tissue was validated using *en face* AZs with anti-Cac/Alexa Fluor 647 and anti-Brp/CF680 localizations, ensuring robust label separation. STORM images were generated similarly to the QuaSOR images described above. Each STORM localization was rendered using a normalized 2D Gaussian intensity profile, with each image being a sum of filtered localizations providing density approximations. All STORM images are *z* projections unless otherwise noted, with similar localization Gaussian σ values (9 – 15 nm) with colors indicating approximate localization densities per pixel.

To quantify the degree of uniformity of excitation in 3D STORM over the field of view (FOV), we plotted total Brp and Cac localizations per AZ against radial distance from the center of the FOV. As shown in **Supplementary Figure 2.21**, both Brp and Cac localization numbers varied widely and uniformly (~5% trend in opposite directions for Brp and Cac) over the range of radial distances from the center of the FOV, indicating uniform excitation.

For AZ-specific STORM quantifications, we first identified all AZ locations at a relatively low resolution (32 nm/px). Each AZ ROI was then rendered at a substantially higher resolution (1.6 nm/px), whereby individual AZ areas could be clearly identified and isolated, typically using a *z* projection of Brp localizations. These areas were used to identify isolated ROIs corresponding to individual AZs, with the ROI being used to calculate all AZ statistics. To account for variations in the STORM imaging conditions for each NMJ, we normalized the values within each NMJ to the largest AZ, unless otherwise noted. The orientation of each AZ was classified according to the relative Brp-defined AZ shape, AZ position within the bouton, the conventional Hrp image (which provided the relative location of membrane) and the relative locations of Brp and Cac in those datasets. Volumetric masking was accomplished by rendering STORM localizations in 3D at 20 nm increments in the *z* dimension. These 3D STORM images were used to generate a volume mask that collected STORM localizations within ~ 80 nm of Brp localization densities above a threshold density of ~ 1 localization per nm^2 for each 20 nm *z* slice throughout the AZ.

Following determination of the alignment parameters, each *en face* AZ image was translated to match a common center location. Localization data were then added and the subsequent pixel values were divided by the number of AZs included in the alignment to calculate the average localization density. Because construction of all STORM images used either unfiltered localization coordinates or normalized 2D Gaussians to represent each localization, the resulting images provide a measure of average localization density per pixel. For *en face* AZ, localization density radial profile calculations, localizations were binned into 10 nm annuli surrounding the center alignment position, with total counts being normalized to the area of each annulus.

Structure-function matching

QuaSOR data were matched to the corresponding Airyscan or STORM data through a multi-stage approach. First, the two datasets were roughly aligned by rotating either the QuaSOR or Airyscan data to match the orientation of the corresponding map. In the case of the STORM imaging, before acquiring STORM data, we obtained conventional images of postsynaptic SynapGCaMP6f labeled with anti-GFP antibody and motor neuron axon membrane labeled with anti-Hrp antibody (**Suppl. Fig. 2.6a**). These were used to align the SynapGCaMP6f baseline fluorescence images obtained during quantal imaging in the living preparation (**Suppl. Fig. 2.6b**). Once roughly aligned, sites were matched to one another in a pairwise fashion taking care to match each STORM or Airyscan AZ to a corresponding location on the QuaSOR map. We used low-density areas to match all unambiguous AZ pairs with clear relative orientations and positions. Following these areas, we used the relative positioning of AZs around these pairs to match the denser regions or match AZs with no corresponding QuaSOR activity to an empty region of the QuaSOR map. In the case of the STORM matching, Brp STORM-defined AZ areas were matched to clusters of QuaSOR event localizations for 100-200 synapses per NMJ. In the Airyscan-matched data we sorted all QuaSOR event coordinates to their nearest QuaSOR AZ centroid location. Both methods produced very similar results. To further ensure unbiased matching, a minimum of two people validated the site pairings prior to quantification. All pairs had to minimize the local alignment variance within each bouton as determined by the alignment vector between sites.

The quality of the AZ matching was further confirmed by using the paired coordinate positions to generate vectors to transform the QuaSOR coordinates into the matching STORM or Airyscan pixel-space. This was done by first converting the relative QuaSOR coordinates into a matched pixel-space image and then using a 2D, locally weighted, mean transformation method[93], with groupings of 8-14 AZs being used as control points in the local weighting. Successful site pairing generated accurate remapping of QuaSOR events onto the appropriate AZ for either structural imaging technique. In all figures these transformed images are denoted by "*Evoked" or "*Spontaneous". However, all quantifications were performed on un-translated data in order to eliminate artifacts of transformations.

Additionally, we used an automated alignment, clustering and matching process to confirm general trends within the data. This involved aligning the STORM and QuaSOR coordinate sets with an Affine registration and then taking advantage of a density-based spatial clustering of applications with noise (DBSCAN) to identify AZ clusters within both STORM and QuaSOR datasets. Corresponding AZ clusters were then matched, with interpolation to account for QuaSOR sites with no detected evoked responses. While this generated similar results, we found better performance with manual corrections of ROIs, as it allowed for proper separation of neighboring AZs in dense regions.

Electrophysiology

Female third instar larvae were dissected as described above and all recordings were performed on muscle 4 from segment A3 only. Recording electrodes contained 3 M

KCl and had resistances in the range 15-25 MΩ. For two-electrode voltage clamp experiments, the membrane was held at -70 mV. All data were recorded at 5 kHz, with an AxoClamp-2A amplifier and Digidata 1322A interface and Clampex 8.0 software (Molecular Devices, Sunnyvale, CA). For simultaneous electrophysiology measurements with imaging, the image acquisition was triggered by the Digidata so that the imaging was time-locked to the start of the electrophysiology recording. All electrophysiological recordings were analyzed with custom-written MATLAB routines. Briefly, all data were moving average low-pass filtered with a span of 2 ms. EPSPs and EPSCs were calculated as the difference between the peak response to the average baseline immediately prior to stimulation. At least 20 evoked responses were acquired at 0.1 Hz and then averaged to calculate the mean response with both recording types. For simultaneous mEPSP/mEPSC and optical recordings verified optical events and mEPSPs/mEPSCs were paired manually according to their relative timing and amplitudes. Evoked responses were also used to more accurately align the two data types.

Statistics

Wilcoxon signed-rank or Mann-Whitney *U* tests were used to compare paired Ib-Is quantifications. Two-sample Kolmogorov-Smirnov tests or Cramér–von Mises tests were used to compare pooled cumulative distributions. One-way ANOVAs with Tukey-Kramer *post hoc* tests were used to compare mean NMJ Ib-Is properties for different genotypes, pooled data cumulative frequency distributions for different genotypes and distributions of data between multiple bins. One-dimensional Pearson's correlation coefficients (*R*) were used to compare the radial density profiles for different QuaSOR event types (i.e. spontaneous versus evoked). 2D fitting of the binned data utilized linear regressions or nonlinear regressions, while three-dimensional fits were calculated using a linear polynomial surface. All R^2 values and fit equations are provided in the figure legends. Unless otherwise noted, reported values are mean ± SEM. The specific statistical tests as well as number of replicates including numbers of animals, activity bouts, NMJs or AZs are all provided in the corresponding figures and/or figure legends. For all figures, significance markers are * $p < 0.05$, ** $p < 0.01$, *** $p < 0.001$, **** $p < 0.0001$ or NS not significant for the comparisons indicated in the figure or figure legend.

Figures

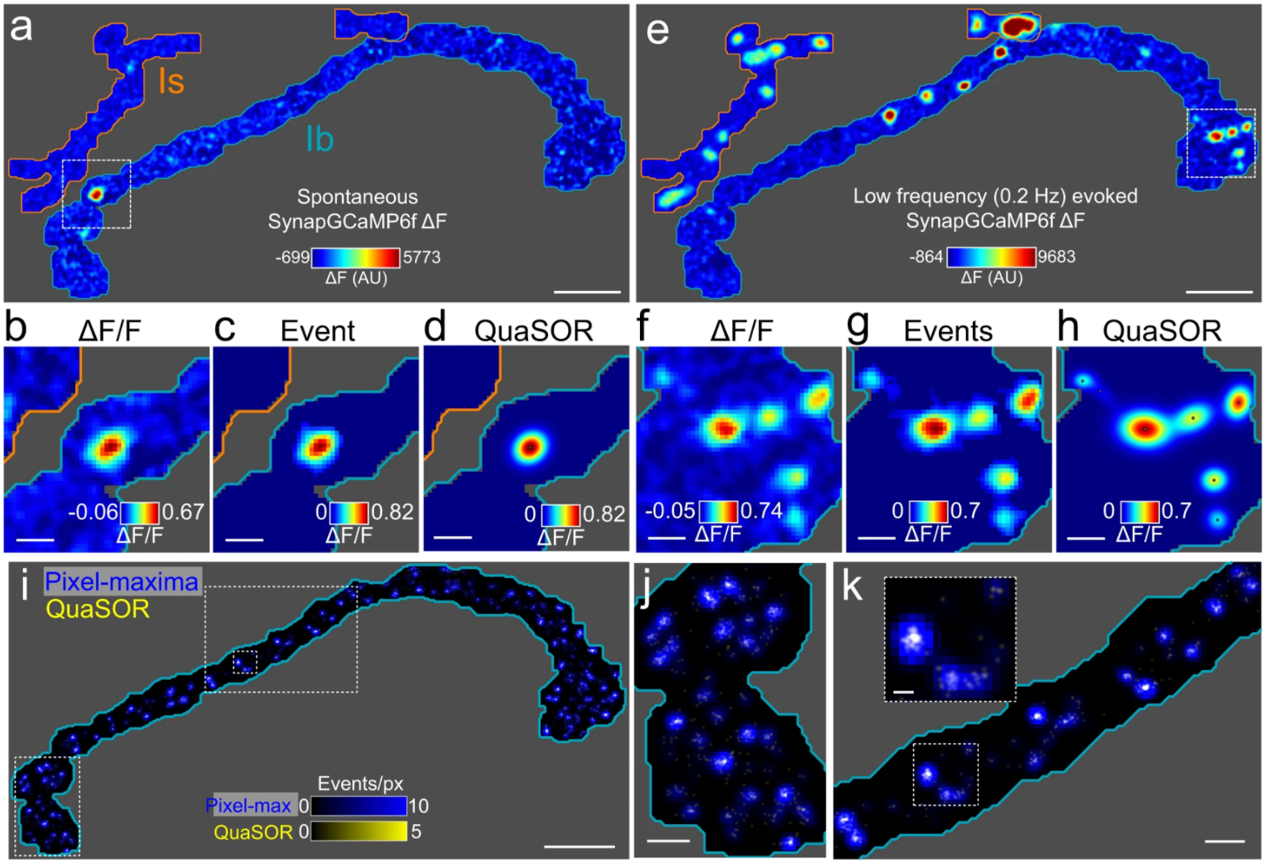

Figure 2.1: QuaSOR super-resolution mapping of spontaneous and evoked transmission.
a, Example spontaneous quantal event showing a full WT NMJ ΔF frame. Gray regions indicate areas of the muscle that were not associated with either Ib or Is NMJ and therefore not analyzed. **b**, ΔF/F corresponding to boxed region in **a**. **c**, Same event as in **a-b** showing isolated ΔF/F (only pixels associated with event). **d,** QuaSOR-determined 2D Gaussian model for event in **a-c**. Black dot indicates maxima coordinate. **e,** Single AP-evoked ΔF response frame. **f**, ΔF/F frame corresponding to boxed region in **e**. **g**, Same AP-evoked events as in **e-f** showing isolated ΔF/F. **h**, QuaSOR-determined 2D Gaussian mixture model for 7 events in **g**. Black dots indicate maxima coordinates for each event component. **i-k**, Comparison of AP-evoked pixel-maxima and QuaSOR mapping methods for the example Ib NMJ in **a-g** (pixel-maxima method blue, 211.6 nm/px, σ = 211.6 nm; QuaSOR yellow, 21.2 nm/px, σ = 42.3 nm; overlap white). Scale bars: 10 μm (**a,e,i**), 2 μm (**b-d,f-h,j-k**) and 500 nm (**k Inset**).

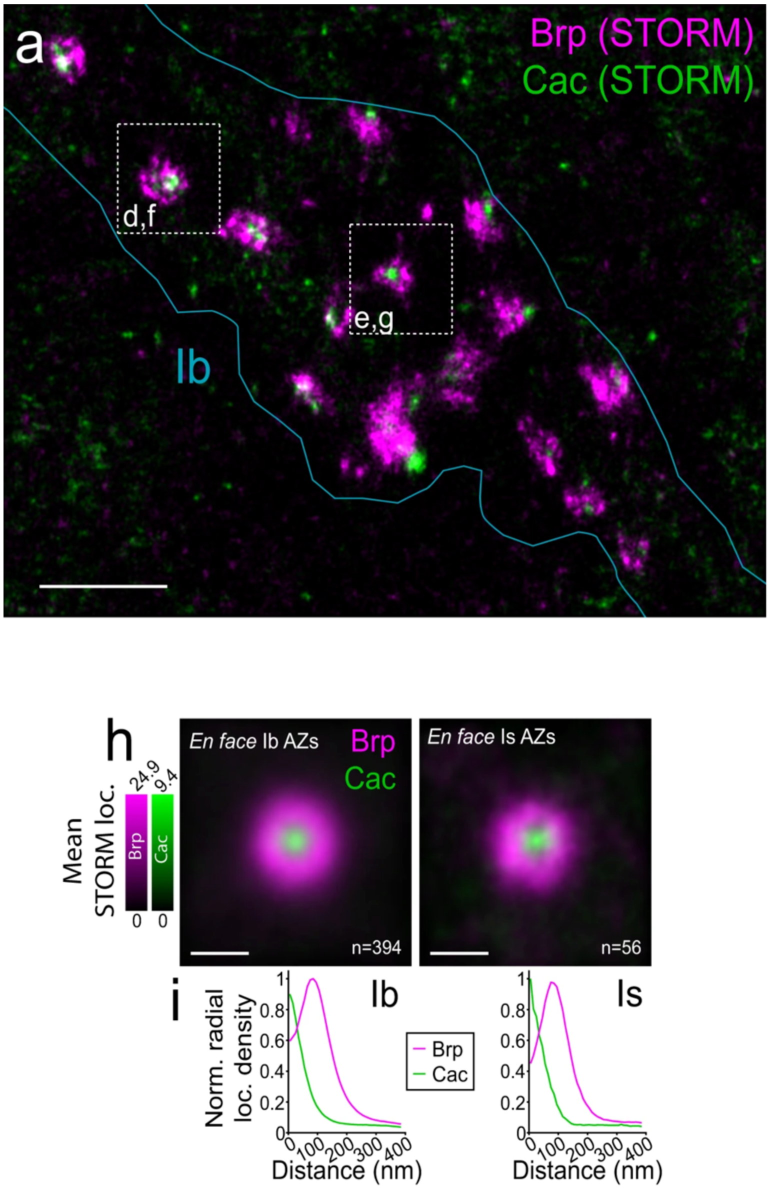

Figure 2.2: 3D-STORM reconstructs Brp and Cac across synapses and orientations.
a, WT 3D-STORM *z*-projection of Brp (magenta) and Cac (green) localizations for a representative Ib bouton. **b-c**, Schematics of the Brp and Cac molecule arrangements and their antibody epitopes (* Brp; + Cac) for *en face* AZs in **b** and side-on AZs in **c**. **d-g**, 3D-STORM projection images of Brp (magenta) and Cac (green) for two *en face* AZs from the bouton in **a**. Shows *x-y* images with a *z*-projection in **c,d** and *y-z* images with an *x*-projection in **f,g**. **h**, Pooled Ib and Is *en face* AZ alignments. Brp (magenta) and Cac (green) *z*-projection mean density images, aligned and averaged, for Ib AZs (left; n = 394 AZs from 9 NMJs) and Is AZs (right; n=56 AZs from 9 NMJs). **i**, STORM density radial profiles for Ib (left) and Is (right) *en face*-aligned AZ averages in **h**, normalized to the maximum radial density between the two axon types. Scale bars: 1 µm (**a**), 200 nm (**d-h**).

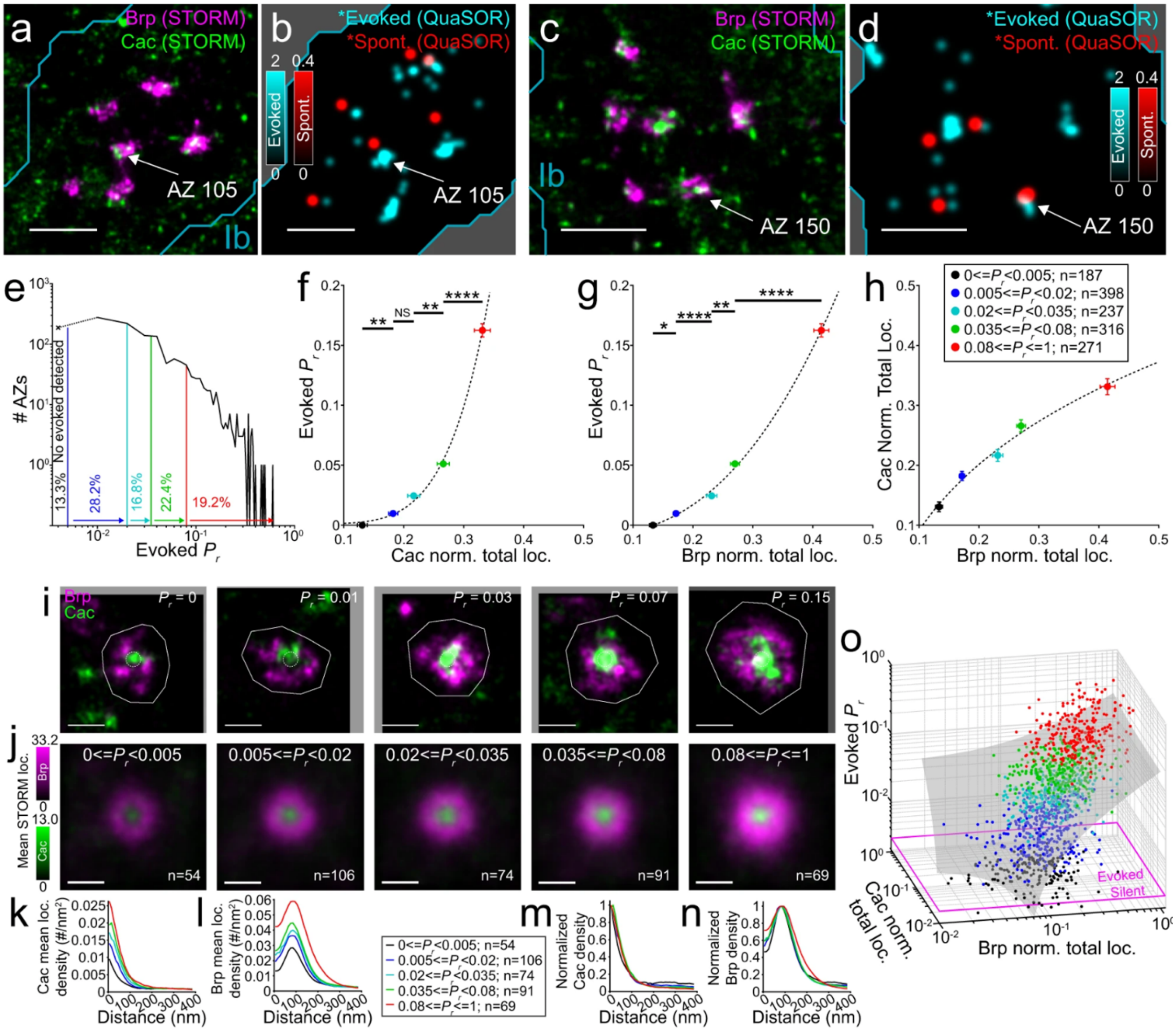

Figure 2.3: QuaSOR-STORM: Cac and Brp strongly promote P_r but account for only a fraction of P_r variance across extremely diverse synapses.

a-d, QuaSOR-STORM alignment examples. Two WT Ib NMJ boutons showing Brp and Cac 3D-STORM *z*-projections in **a,c** alongside the corresponding STORM-aligned QuaSOR map (σ = 42.3 nm) for evoked (*; cyan) and spontaneous (*; red) events in **b,d**. Whole Ib NMJ alignments are found in **Suppl. Fig. 6**. **e**, WT Ib AZ evoked P_r distribution with bin edges (see **f-h**) and percentages (n = 1409 QuaSOR-STORM matched Ib AZs from 9 NMJs; 200 stimuli at 0.2 Hz episodic protocol) with (×) indicating the fraction of sites with no detected evoked transmission. **f**, P_r dependence on Cac. P_r-binned, mean NMJ-normalized total Cac STORM localizations per AZ versus mean evoked P_r for all AZ orientations ($R^2 = 0.998$; $y=42x^{\mathbf{5.0}} + 0.001$; ANOVA $p < 0.0001$ with Tukey-Kramer *post hoc* tests indicated). **g**, P_r dependence on Brp. P_r-binned, mean NMJ-normalized total Brp STORM localizations per AZ versus mean evoked P_r ($R^2 = 0.998$; $y=1.7x^{\mathbf{2.6}} - 0.01$; ANOVA $p < 0.0001$ with Tukey-Kramer *post hoc* tests indicated). **h**, Non-linear Brp-Cac relationship. P_r-binned, mean NMJ-normalized total STORM localizations per AZ for Brp versus Cac ($R^2 = 0.987$; $y=1.2x^{\mathbf{0.2}} - 0.65$). **i**, Representative *en face* AZs (all from same NMJ) showing 3D-STORM overlay *z*-projections for Brp (magenta) and Cac (green) from each of the P_r-binned groups in **e** with AZ borders (solid white lines) and core 40 nm radial region (white dotted circles). **(continued on the next page)**

Figure 2.3(cont.)

j, Average Brp and Cac densities across P_r. Aligned and spatially averaged *en face* projections for Brp (magenta) and Cac (green) from bins in **e** (from 9 NMJs). **k-l**, Radial mean STORM localization density profiles for *en face* AZs showing Cac in **k** and Brp in **l**. **m-n,** Relative Cac (**m**) and Brp (**n**) radial profile dimensions across P_r showing bin-normalized mean radial density profiles for the corresponding *en face* AZ profiles in **k**-**l**. **o**, Pooled NMJ-normalized total Brp STORM localizations versus Cac localizations versus P_r for all AZ orientations. AZs with a P_r below the detection threshold value (magenta lines) are indicated. AZ colors correspond to the respective bins in **e**. 3D fit (gray plane) is linear polynomial surface ($R^2 = 0.312$ $P_r = -0.014 + 0.21 Brp + 0.053 Cac$; n = 1409 AZs from 9 NMJs). Scale bars: 1 µm (**a-d**) and 200 nm (**i,j**).

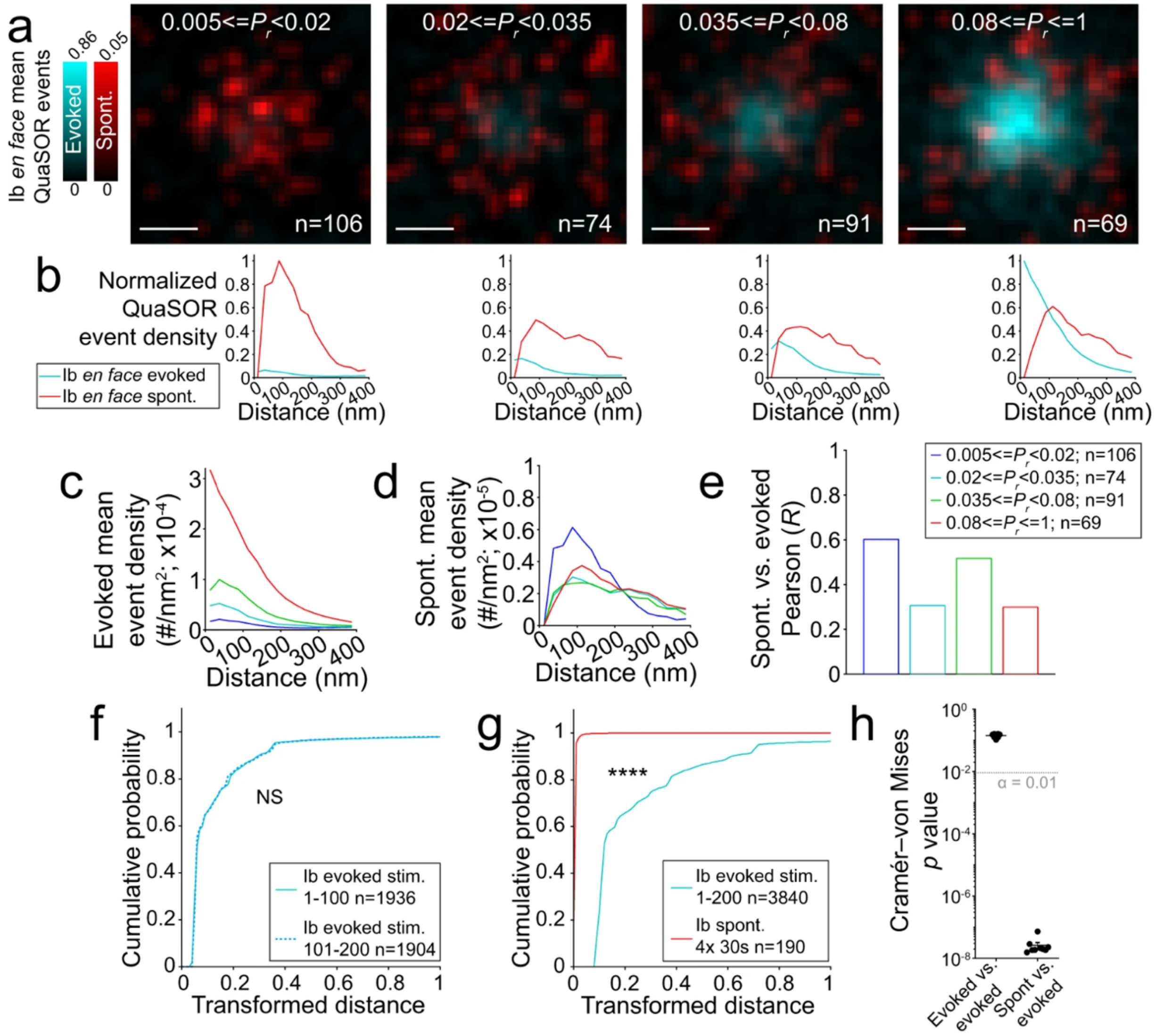

Figure 2.4: Evoked and spontaneous transmission are spatially mismatched.
a, Evoked and spontaneous average event densities across P_r. P_r-binned, aligned and averaged *en face* classified QuaSOR spatial patterns for evoked-active Ib AZs showing both evoked (cyan) and spontaneous (red) events (σ = 21.2 nm). **b**, QuaSOR radial event density profiles across P_r. P_r-binned, normalized *en face* radial mean evoked and spontaneous density profiles for event distributions in **a**. Normalization is calculated from the maximum profile density for each event type. **c-d**, Aligned P_r-binned *en face*-defined radial mean event density profiles for evoked (**c**) and spontaneous (**d**) events. **e**, Spatial decoupling of evoked and spontaneous radial profiles. Pearson correlation coefficients (*R*) for evoked versus spontaneous P_r-binned *en face*-defined radial mean density profiles for each evoked-active P_r bin in a**-d**. **f**, Global evoked pattern stability across stimulus trials. Representative transformed distance distributions for a single NMJ (example in **Suppl. Fig. 6**) comparing evoked event coordinates from stimuli 1-100 (solid; n = 1936 events) to evoked coordinates from stimuli 101-200 (dashed; n = 1904 events; Cramér–von Mises *p* = 0.14). **g**, Global spontaneous and evoked pattern decoupling. Representative transformed distance distributions for the same NMJ in **f** comparing evoked event coordinates from all stimuli 1-200 (cyan; n = 3840 events) versus all spontaneous event coordinates (red; n = 190 events; Cramér–von Mises $p = 1.56*10^{-7}$). **h**, Global decoupling of evoked and spontaneous release. Pooled Cramér–von Mises *p* values for evoked first half versus evoked second half (**f**) and all evoked stimuli versus spontaneous (**g**) cumulative distributions for multiple WT NMJs (n = 9 NMJs). Dotted line indicates an α = 0.01. Scale bars: 200 nm (**a**).

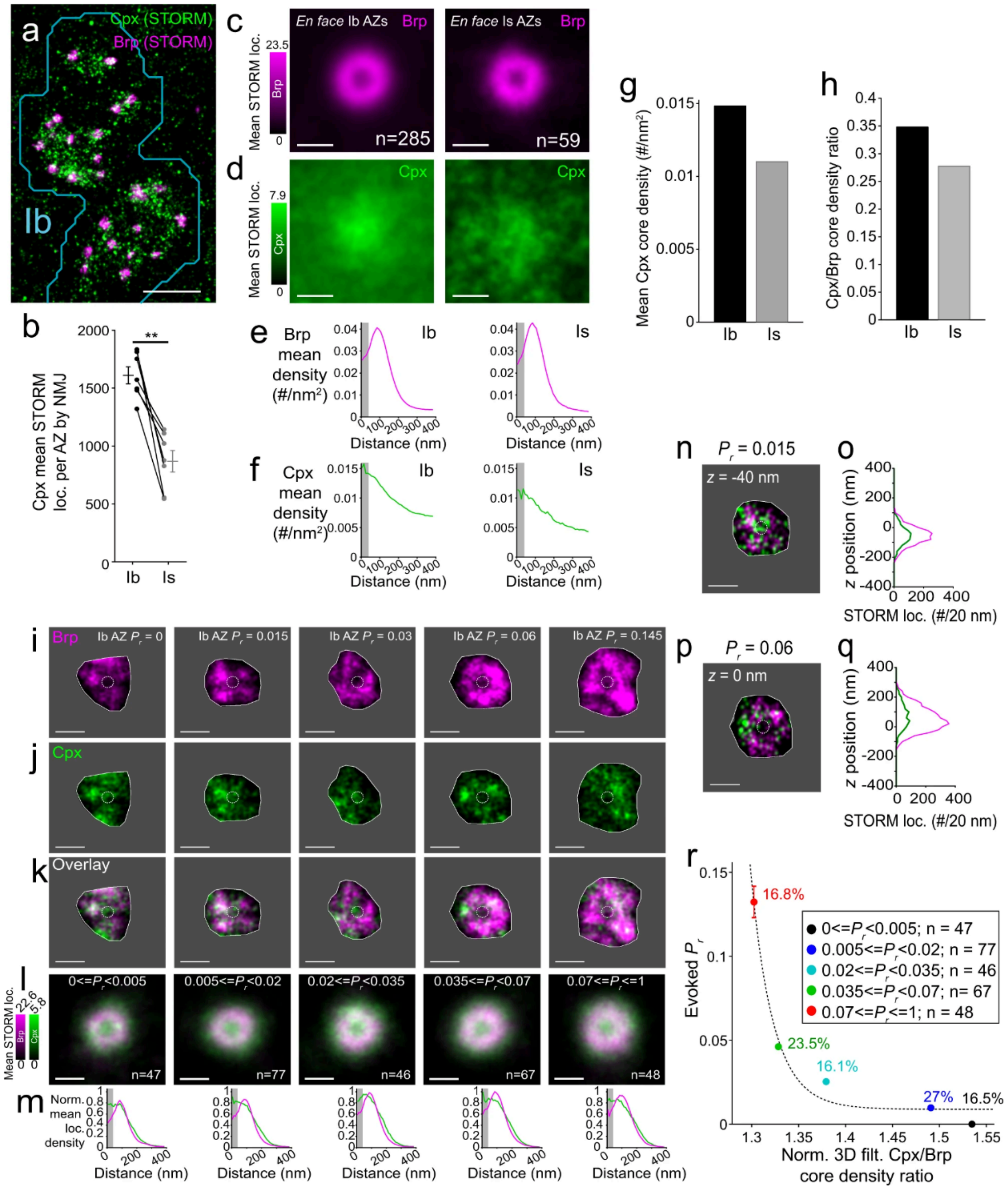
a
Cpx (STORM)
Brp (STORM)
Ib
b
Cpx mean STORM loc. per AZ by NMJ
2000
1500
1000
500
0
**
Ib
Is
c
En face Ib AZs Brp
En face Is AZs Brp
Mean STORM loc.
23.5
Brp
0
n=285
n=59
d
Cpx
Mean STORM loc.
7.9
Cpx
0
e
Brp mean density (#/nm²)
0.04
0.03
0.02
0.01
0
Ib
Is
0 100 200 300 400
Distance (nm)
f
Cpx mean density (#/nm²)
0.015
0.01
0.005
0
Ib
Is
0 100 200 300 400
Distance (nm)
g
Mean Cpx core density (#/nm²)
0.015
0.01
0.005
0
Ib
Is
h
Cpx/Brp core density ratio
0.4
0.35
0.3
0.25
0.2
0.15
0.1
0.05
0
Ib
Is
i
Brp
Ib AZ Pr = 0
Ib AZ Pr = 0.015
Ib AZ Pr = 0.03
Ib AZ Pr = 0.06
Ib AZ Pr = 0.145
j
Cpx
k
Overlay
l
Mean STORM loc.
22.6
5.8
Brp
Cpx
0 0
0<=Pr<0.005
0.005<=Pr<0.02
0.02<=Pr<0.035
0.035<=Pr<0.07
0.07<=Pr<=1
n=47
n=77
n=46
n=67
n=48
m
Norm. mean loc. density
1
0.8
0.6
0.4
0.2
0
0 200 400
Distance (nm)
n
Pr = 0.015
z = -40 nm
o
z position (nm)
400
200
0
-200
-400
0 200 400
STORM loc. (#/20 nm)
p
Pr = 0.06
z = 0 nm
q
z position (nm)
400
200
0
-200
-400
0 200 400
STORM loc. (#/20 nm)
r
Evoked Pr
0.15
0.1
0.05
0
16.8%
23.5%
16.1%
27%
16.5%
● 0<=Pr<0.005; n = 47
● 0.005<=Pr<0.02; n = 77
● 0.02<=Pr<0.035; n = 46
● 0.035<=Pr<0.07; n= 67
● 0.07<=Pr<=1; n = 48
1.3
1.35
1.4
1.45
1.5
1.55
Norm. 3D filt. Cpx/Brp core density ratio

Figure 2.5: Cpx at the Brp annular AZ core suppresses evoked transmission.
a, Brp and Cpx 3D-STORM *z*-projection of the terminal boutons for a WT Ib axon. **b**, Axon-specific differences in Cpx levels. Pooled mean total Cpx localizations for WT Ib and Is AZs (n = 7 NMJ pairs; Wilcoxon signed-rank test $p = 0.0156$). **c-d**, Cpx distributions in WT Ib (**left**; n = 285 AZs from 7 NMJs) and Is (**right**; n=59 AZs from 7 NMJs) *en face*-aligned AZs showing Brp (**c**; magenta) and Cpx (**d**; green) *z*-projection aligned mean density images. **e-f**, Radial STORM Brp (**e**) and Cpx (**f**) density profiles for WT Ib (**left**) and Is (**right**) *en face*-aligned AZs in **c,d** with core 40 nm radial region (gray area) indicated. **g-h**, Cpx enrichment in Ib AZ core. Mean core radial Cpx density (**g**) and core Cpx/Brp density ratio (**h**) in WT AZs. **i-k**, Representative, P_r-binned, volume filtered, *en face* Ib AZ 3D-STORM images (all from same NMJ) for Brp (**i**; magenta), Cpx (**j**; green) and overlay (**k**). Largest *x*-*y* quantification area for each AZ (gray area) and core 40 nm radius (dotted circle) indicated. **l**, P_r-binned, aligned and averaged 3D-STORM overlays showing 3D-filtered, average density *z*-projections for WT Ib *en face* AZs. **m**, Radial normalized mean 3D-STORM localization density profiles for P_r-binned spatial averages in **l** with core 40 nm radial region (gray area) indicated. **n-q**, AZ core Cpx levels in low P_r (**n-o**) and high P_r AZs (**p-q**) including a 3D-filtered, 20 nm thick *z* slice image at indicated depth (**n,p**) and the corresponding STORM localization counts along the *z* depth of the AZ (**o,q**). The core 40 nm radial region (dotted circle) is also indicated (**n,p**). **r**, AZ core Cpx/Brp ratio inversely related to P_r. P_r-binned, 3D-filtered, mean core 40 nm radial Cpx/Brp density ratio ($R^2 = 0.98$ $y=2.4*10^5x^{-55}+0.009$). Scale bars: 2 μm (**a**) and 200 nm (**c,d,i-l,n,p**).

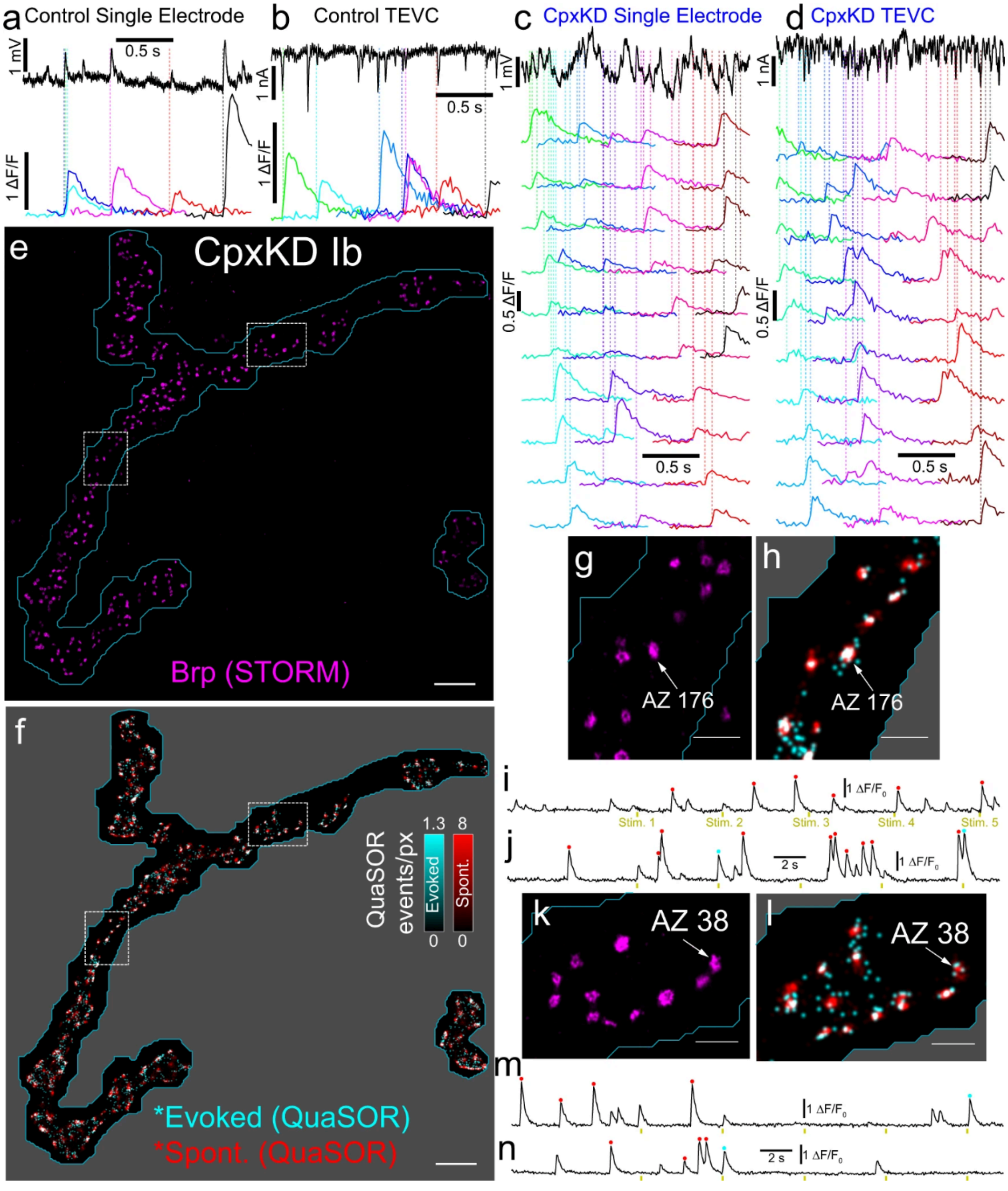
a Control Single Electrode
0.5 s
1 mV
1 ΔF/F
b Control TEVC
1 nA
0.5 s
1 ΔF/F
c CpxKD Single Electrode
1 mV
0.5 ΔF/F
0.5 s
d CpxKD TEVC
1 nA
0.5 ΔF/F
0.5 s
e
CpxKD Ib
Brp (STORM)
f
QuaSOR events/px
1.3
Evoked
0
8
Spont.
0
*Evoked (QuaSOR)
*Spont. (QuaSOR)
g
AZ 176
h
AZ 176
i
1 ΔF/F0
Stim. 1
Stim. 2
Stim. 3
Stim. 4
Stim. 5
j
2 s
1 ΔF/F0
k
AZ 38
l
AZ 38
m
1 ΔF/F0
n
2 s
1 ΔF/F0

Figure 2.6: Analysis of spontaneous and evoked transmission in the knockdown of Cpx.
a-d, Simultaneous electrophysiological and optical analysis of transmission in Control (**a,b**) and CpxKD (**c,d**) NMJs. Spontaneous events are infrequent enough in control animals to be easily measured electrophysiologically (black traces) as mEPSPs (**a**) and mEPSCs (**b**) and to identify corresponding optical events at identified synapses (colored traces). In CpxKD animals, the frequency of spontaneous mEPSPs (**c**) and mEPSCs **(d**) (black traces) is too high to measure electrophysiological events accurately, but optical events at individual synapses occur infrequently enough to measure easily (colored traces). **e**, Brp 3D-STORM *z*-projection image for a CpxKD Ib NMJ (OK6-Gal4, UAS-Cpx^{RNAi}, SynapGCaMP6f). **f**, CpxKD QuaSOR map including evoked (cyan) and spontaneous (red) events (σ = 42.3 nm) aligned to 3D-STORM area in e. **g-n,** Two magnified Ib boutons from ROIs shown in dashed squares in **f**, each with a single example AZ (**g-h**, AZ 176 and k-l, AZ 38) and its corresponding QuaSOR traces (**i-j** for AZ 176 and **m-n** for AZ 38). The QuaSOR traces mark evoked (cyan dots) and spontaneous (red dots) transmission events. Unmarked events were generated at other neighboring sites. Stimulus times are indicated below the traces. Scale bars: 5 µm (**e,f**), 1 µm (**g-h, k-l**).

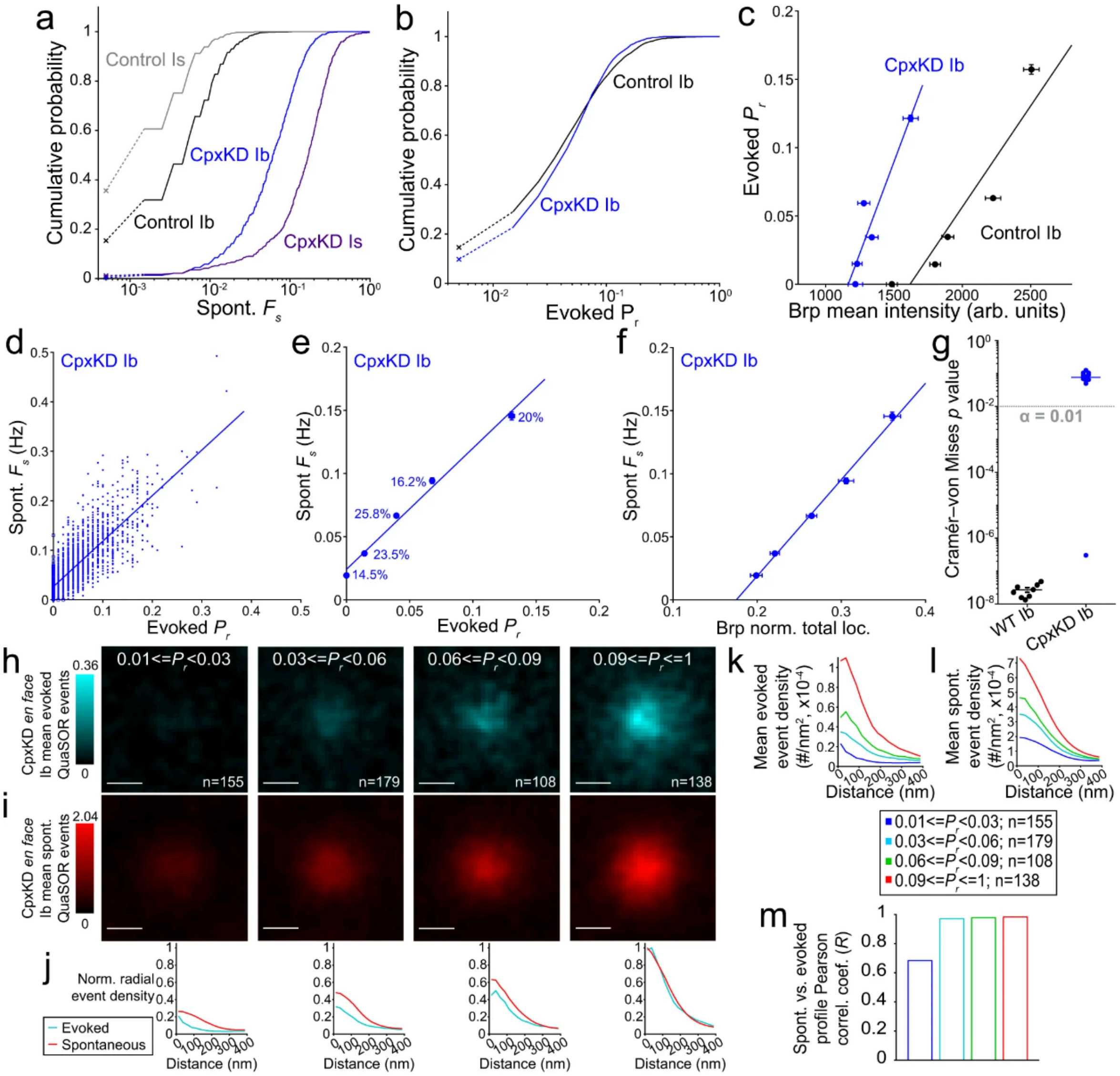

Figure 2.7: Knockdown of Cpx increases F_s more at Is synapses, boosts the dependence of evoked transmission on Brp and eliminate the spatial and quantitative mismatch between spontaneous and evoked transmission.

a, CpxKD increases F_s in both Ib and Is. F_s distributions for Control (OK6-Gal4, attP40$^{\text{Empty}}$, SynapGCaMP6f) Ib (n=2709 AZs from 7 NMJs), Control Is (n=1114 AZs from 7 NMJs), CpxKD Ib (Ib n=1547 AZs from 5 NMJs) and CpxKD Is (n=697 AZs from 5 NMJs) pooled QuaSOR-Airyscan matched AZs (ANOVA $p < 0.0001$; Tukey-Kramer *post hoc* test; Control Ib vs Control Is $p = 0.15$; CpxKD Ib vs CpxKD Is $p < 0.0001$; Control Ib vs CpxKD Ib $p < 0.0001$; Control Is vs CpxKD Is $p < 0.0001$). **b**, Normal AP-evoked release in CpxKD Ib NMJs. P_r distributions for QuaSOR-Airyscan matched Control and CpxKD Ib AZs (Kolmogorov–Smirnov test $p = 0.00071$). **c**, P_r dependence on Brp shifts to the left in CpxKD Ib NMJs. P_r-binned, mean Airyscan Brp voxel intensities versus mean evoked P_r for Control Ib (black; $y=1.48*10^{-4}x-0.239$; $R^2 = 0.873$) and CpxKD Ib (blue; $y=2.68*10^{-4}x-0.313$; $R^2 = 0.871$) AZs. **d-e**, P_r and F_s are highly correlated in CpxKD Ib synapses. QuaSOR-STORM matched, pooled P_r versus F_s for all CpxKD Ib AZs in **d** ($R^2 = 0.62$; n=1774 AZs from 6 NMJs) and QuaSOR-STORM matched, P_r-binned (bin percentages indicated), mean P_r versus mean F_s for CpxKD Ib AZs in **e** ($R^2 = 0.991$; $y=0.96x+0.024$). **f**, F_s has a linear dependence on Brp in CpxKD Ib NMJs. QuaSOR-STORM matched, P_r-binned, mean NMJ-normalized total Brp STORM localizations per AZ versus F_s ($R^2 = 0.995$; $y=0.76x-0.13$). **(continued on the next page)**

Figure 2.7 (cont.)
g, Global spatial overlap between spontaneous and evoked events in CpxKD animals but not in WT animals. Pooled Cramér–von Mises *p* values for WT (n = 8) and CpxKD Ib (n = 11) NMJs in response to 100 stimuli (evoked) and during a 600 s period of observation without stimulation (spontaneous). **h-i**, Local spatial overlap between spontaneous and evoked events in CpxKD animals. P_r-binned, aligned evoked (cyan; **h**) and spontaneous (red; **i**) QuaSOR spatial averages (σ = 42.3 nm) from *en face* classified, evoked-active CpxKD Ib AZs (n=655 from 6 NMJs). **j**, Normalized radial density profiles for CpxKD Ib AZs. **k-l**, Aligned P_r-binned (as indicated in color code inset), *en face* classified, evoked-active CpxKD Ib AZ radial mean QuaSOR evoked (**k**) and spontaneous (**l**) density profiles. **m**, High local correlation between spontaneous and evoked radial profiles. Pearson correlation coefficients (*R*) for evoked *versus* spontaneous transmission events, P_r-binned (same color code as k-l), aligned, *en face* classified, radial mean density profiles for evoked-active CpxKD Ib. Scale bars: 200 nm (**h-i**).

Supplementary Figures

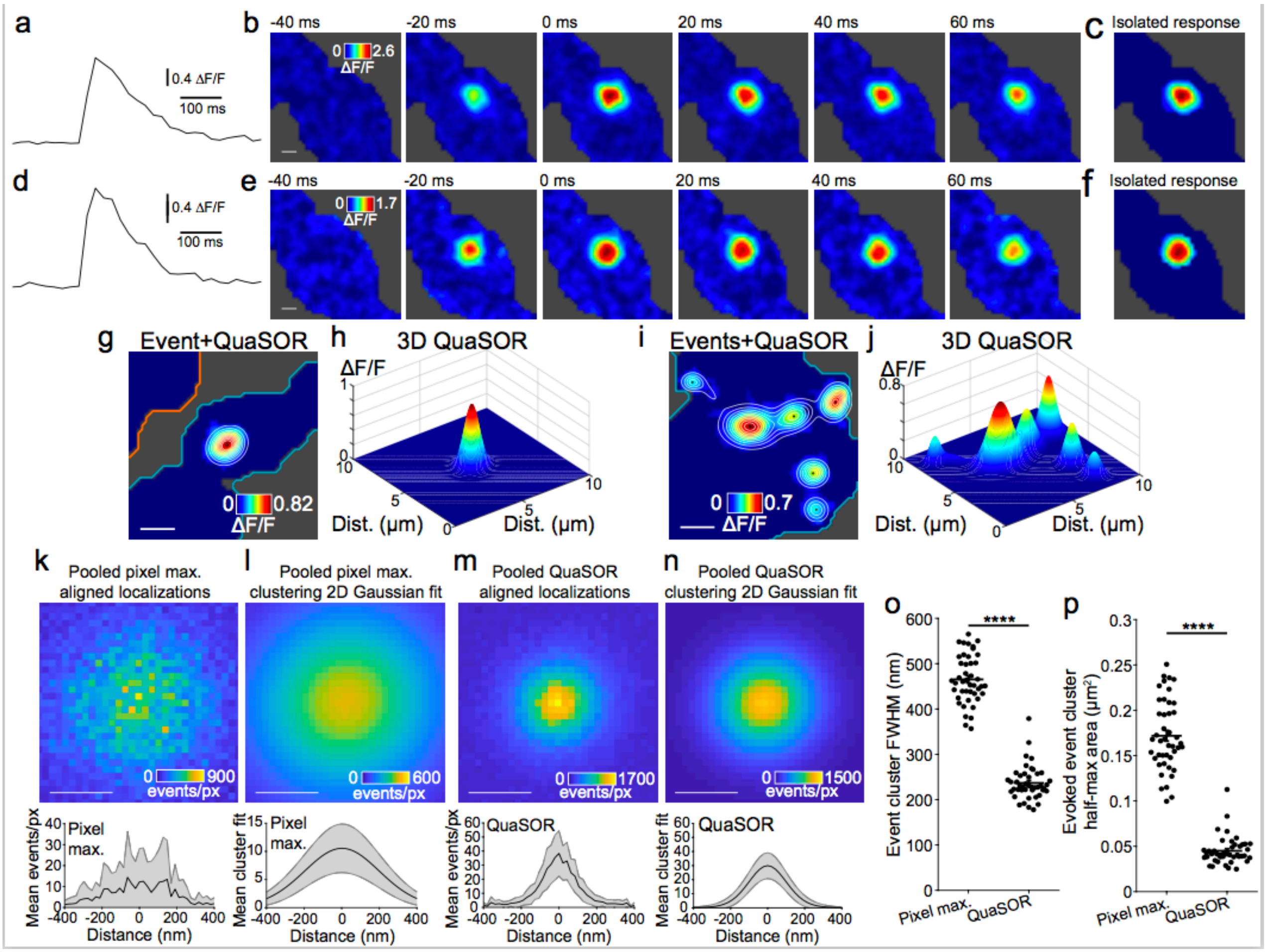

Supplementary Figure 2.1: QuaSOR fitting of evoked and spontaneous transmission events; related to Figure 2.1.

a-f, Rapid spatial spread of quantal SynapGCaMP6f responses. Two example spontaneous events (imaged at 50 FPS) showing mean SynapGCaMP6f ΔF/F traces (**a,d**), sequential ΔF/F frames (**b,e**), and the isolated response following event detection (**c,f**). **g-h**, Same event in **Fig. 1a-d** with the isolated ΔF/F response and contours lines showing the QuaSOR 2D Gaussian fit model in **g** and a 3D representation of the fit model in **h**. **i-j**, Same AP-evoked events in **Fig. 1e-h** with the isolated ΔF/F response and contours lines showing the corresponding merged QuaSOR 2D Gaussian mixture model in **i** and a 3D representation of the mixture model in **j**. **k-n**, Aligned localizations (**k,m**) and 2D Gaussian fits (**l, n**) to evoked transmission events from same data set (10,363 AZs from 44 NMJs) using either the pixel maxima method (**k,l**) or QuaSOR (**m,n**). Images above, spatial profiles below (in all panels data with error bands are presented as mean ± SD). **o-p**, Evoked event cluster full width at half max (FWHM) (**o**) and evoked event cluster half-maximal area (**p**) for the 44 NMJs showing significantly better resolution for QuaSOR (**o** Wilcoxon two-tailed signed-rank *p* = p = $7.59x10^{-9}$;**p** Wilcoxon two-tailed signed-rank *p* = p = $7.62x10^{-9}$). Scale bars: 1 μm (**b,e,g,i**) and 200 nm (**k-n**).

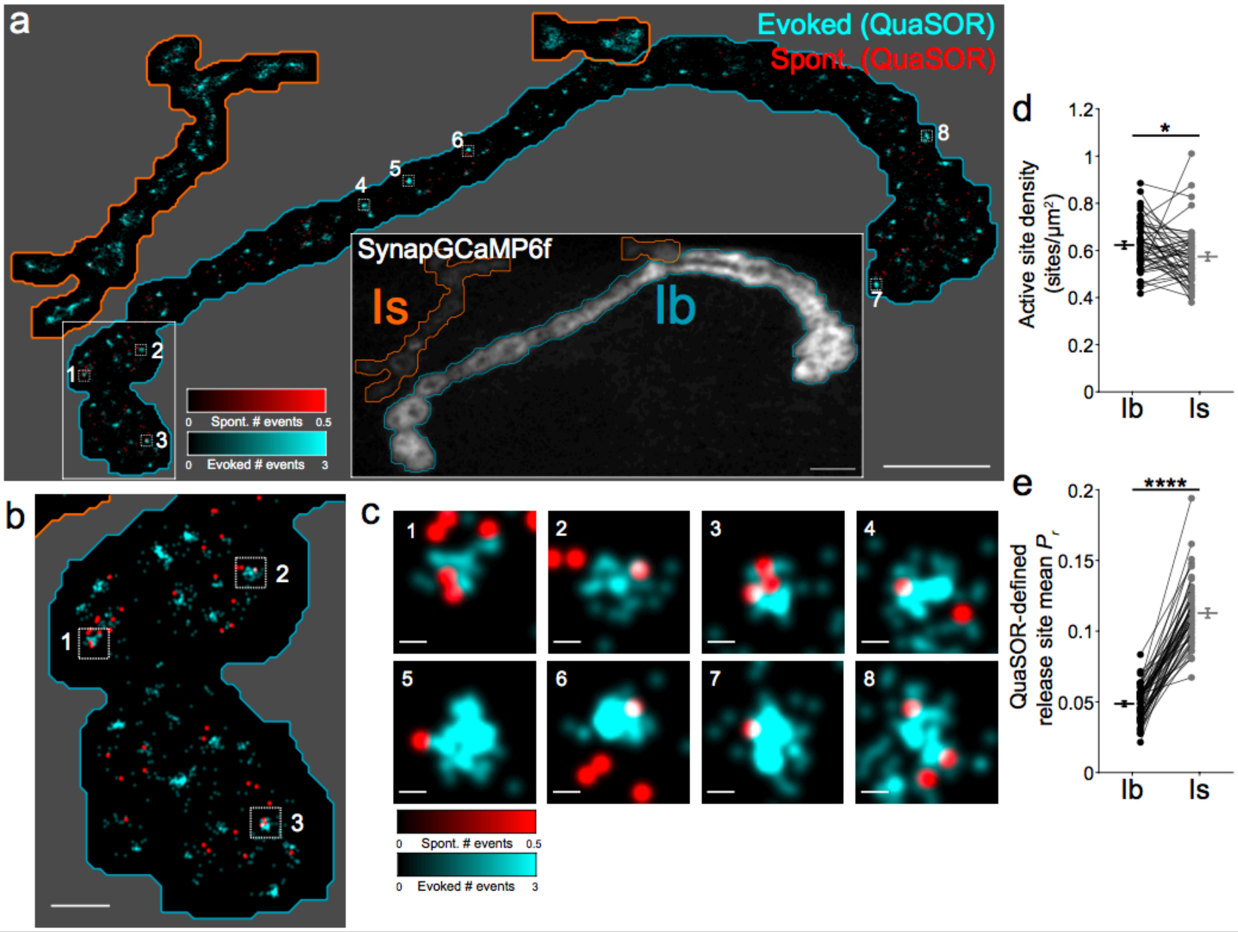

Supplementary Figure 2.2: QuaSOR analysis of evoked and spontaneous transmission; related to Figure 2.1.

a-c, Evoked and spontaneous events do not colocalize in WT NMJs. **a,** Evoked (cyan) and spontaneous (red) QuaSOR transmission event locations (σ = 42.3 nm) in Ib and Is NMJs onto a common muscle 4, with one terminal Ib bouton ROI indicated (white square). **Inset,** Baseline SynapGCaMP6f fluorescence. **b**, Terminal bouton from (**a**) magnified. **c**, QuaSOR transmission clusters from (**b**) further magnified. **d**, QuaSOR-defined active site density, including evoked and spontaneous QuaSOR event clusters (n = 48 NMJ pairs; Wilcoxon two-tailed signed-rank test p = 0.018). **e**, Mean P_r. of QuaSOR-defined transmission sites (Wilcoxon two-tailed signed-rank test $p = 1.6*10^{-9}$). Scale bars: 10 μm (**a**), 2 μm (**b**) and 200 nm (**c**).

a Control Ib NMJ

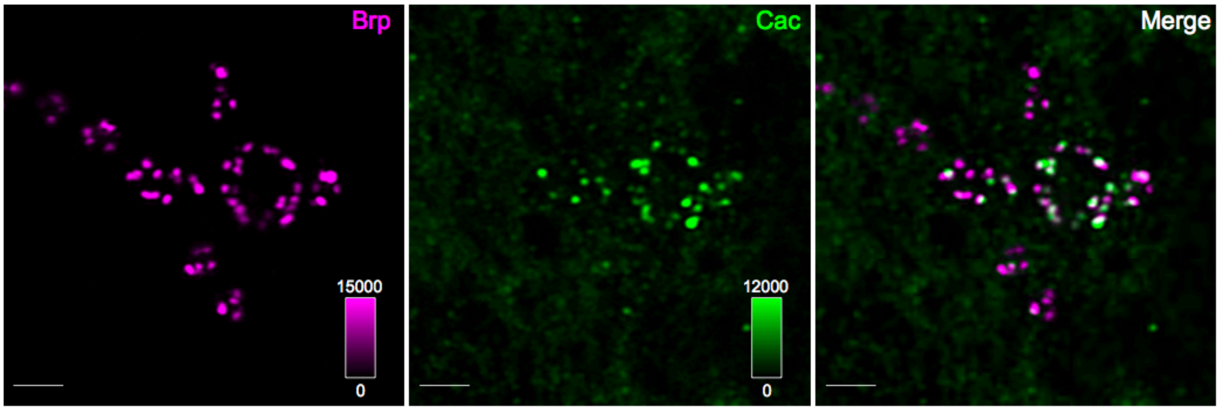

b CacKD Ib NMJ

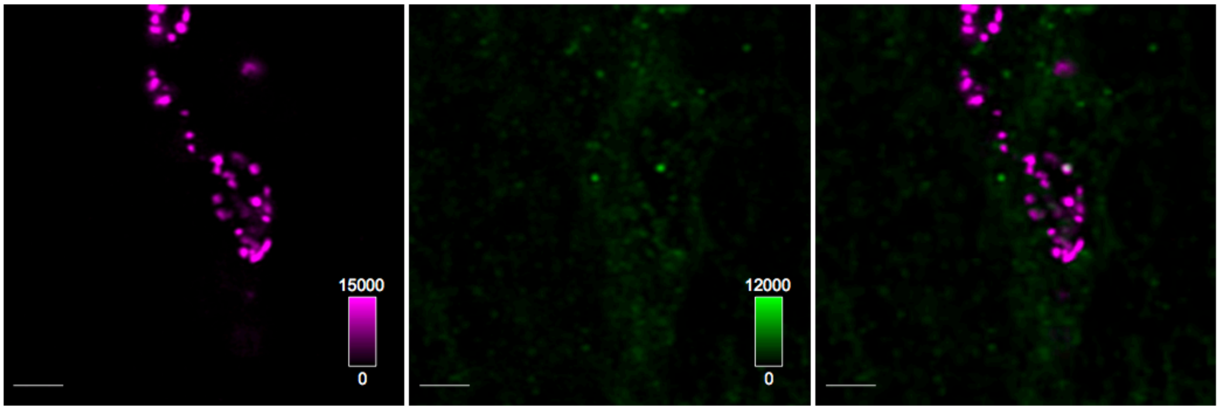

Supplementary Figure 2.3: Cac labeling in control and CacKD animals; related to Figure 2.2. a,b, Cac antibody staining of Ib bouton labels puncta that overlap with Brp puncta in a control NMJ (**a**) but is almost eliminated in the CacKD (**b**), indicating that the antibody is specific for Cac. Scale bars: 2 µm.

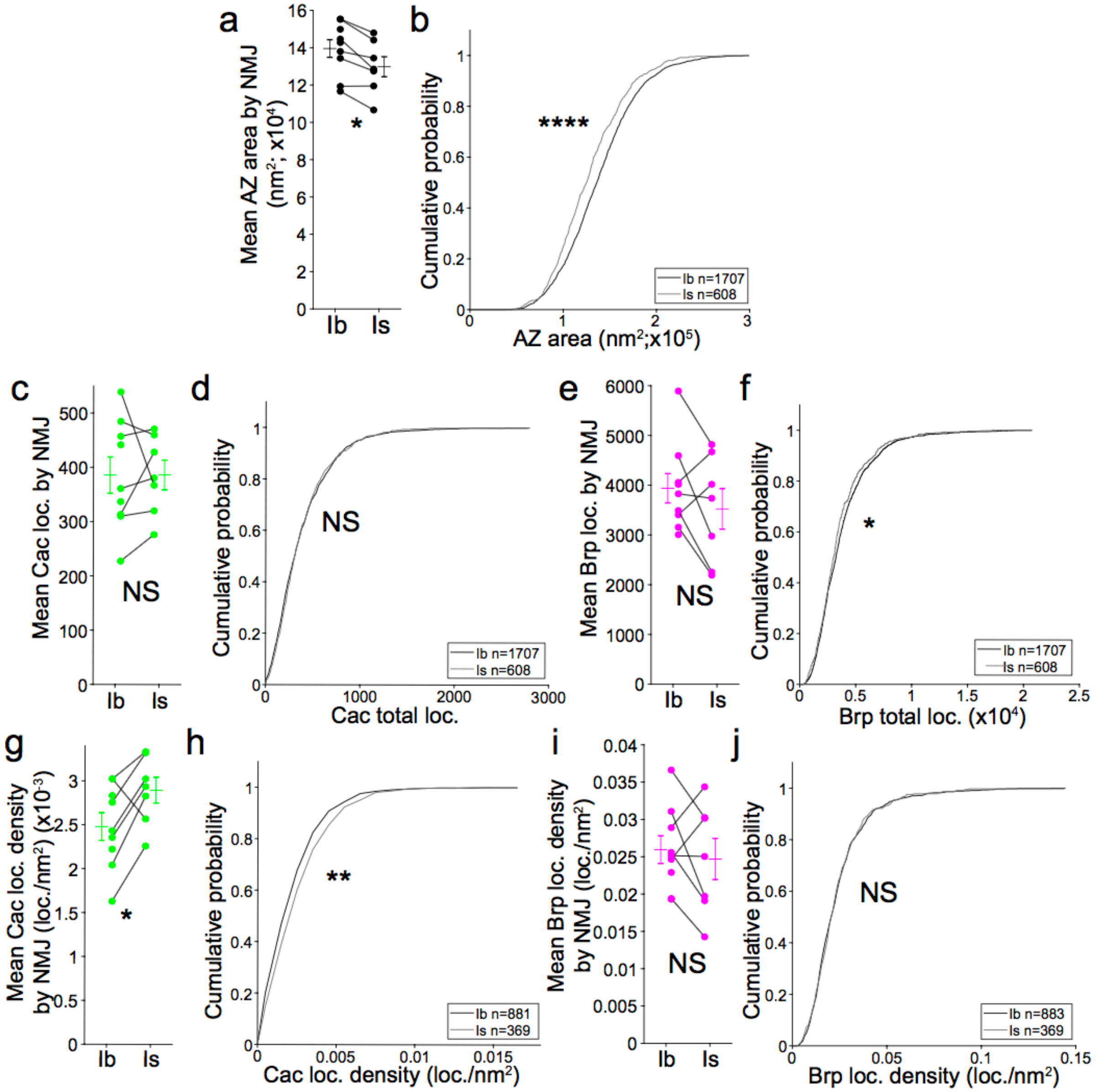

Supplementary Figure 2.4: Brp and Cac in Ib and Is axons; related to Figure 2.2.

a-b, Is AZs slightly smaller than Ib AZs. Mean 3D-STORM Brp AZ area (nm^2) for Ib-Is axon pairs innervating the same muscle 4 (**a**; n = 9 NMJ Ib-Is pairs; Wilcoxon two-tailed signed-rank test *p* = 0.031) and pooled cumulative frequency distributions (**b**; Ib n = 1707 AZs, n = 9 NMJs; Is n = 608 AZs, n = 9 NMJs; two-sample two-sided Kolmogorov–Smirnov test *p* =2.2*10^{-7}). **c-d**, Similar Cac levels in Ib and Is AZs. Mean total Cac 3D-STORM AZ localizations for Ib-Is axon pairs (**c**; n = 9 NMJ Ib-Is pairs; Wilcoxon two-tailed signed-rank test *p* = 0.69) and pooled cumulative frequency distributions (**d**; Ib n = 1707 AZs, n = 9 NMJs; Is n = 608 AZs, n = 9 NMJs; two-sample two-sided Kolmogorov–Smirnov test *p* = 0.38). **(continued on the next page)**

Supplementary Figure 2.4 (cont.) e-f, Similar Brp levels in Ib and Is AZs. Mean total Brp 3D-STORM AZ localizations for Ib-Is axon pairs (**e**; n = 9 NMJ Ib-Is pairs; Wilcoxon two-tailed signed-rank test $p = 0.16$) and pooled cumulative frequency distributions (**f**; Ib n = 1707 AZs, n = 9 NMJs; Is n = 608 AZs, n = 9 NMJs; two-sample two-sided Kolmogorov–Smirnov test $p = 0.033$) **g-h**, Cac density is higher in Is than in Ib AZs. Mean Cac 3D-STORM AZ localization density for Ib-Is axon pairs (**g**; n = 9 NMJ Ib-Is pairs; Wilcoxon two-tailed signed-rank test $p = 0.047$) and pooled cumulative frequency distributions (**h**; Ib n = 1707 AZs, n = 9 NMJs; Is n = 608 AZs, n = 9 NMJs; two-sample two-sided Kolmogorov–Smirnov test $p = 0.0017$). **i-j**, Similar Brp densities in Ib and Is AZs. Mean Brp 3D-STORM AZ localization density for Ib-Is axon pairs (**i**; n = 9 NMJ Ib-Is pairs; Wilcoxon two-tailed signed-rank test $p = 0.30$) and pooled cumulative frequency distributions (**j**; Ib n = 881 AZs, n = 9 NMJs; Is n = 369 AZs, n = 9 NMJs; Kolmogorov–Smirnov test $p = 0.89$). All data Mean ± SEM.

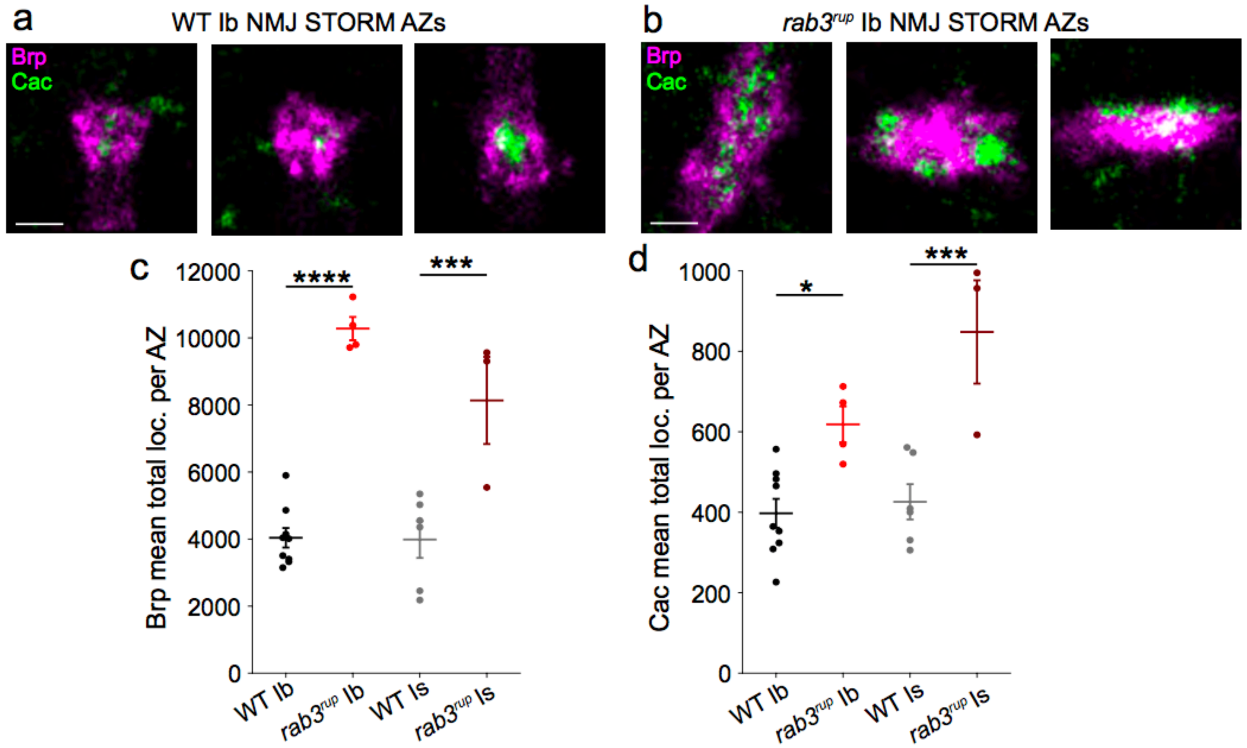

Supplementary Figure 2.5: Brp and Cac STORM AZs in WT and *rab3*^{rup} NMJs; related to Figure 2.2. a-d, STORM images of Ib AZs from WT (**a**) and *rab3*^{rup} (**b**) show that *rab3*^{rup} AZs are larger and contain more Cac puncta, with more Brp localizations per AZ in both Ib and Is axons (**c,** One-way ANOVA $p = 1.8*10^{-7}$; Tukey-Kramer *post hoc* test: WT Ib vs *rab3*^{rup} Ib $p = 5.5*10^{-7}$; WT Is vs *rab3*^{rup} Is $p = 0.00073$; data are presented as mean ± SEM) and more Cac localizations per AZ in both Ib and Is axons (**d,** One-way ANOVA $p = 0.00015$; Tukey-Kramer *post hoc* test: WT Ib vs *rab3*^{rup} Ib $p = 0.36$ WT Is vs *rab3*^{rup} Is $p = 0.00068$; data are presented as mean ± SEM).

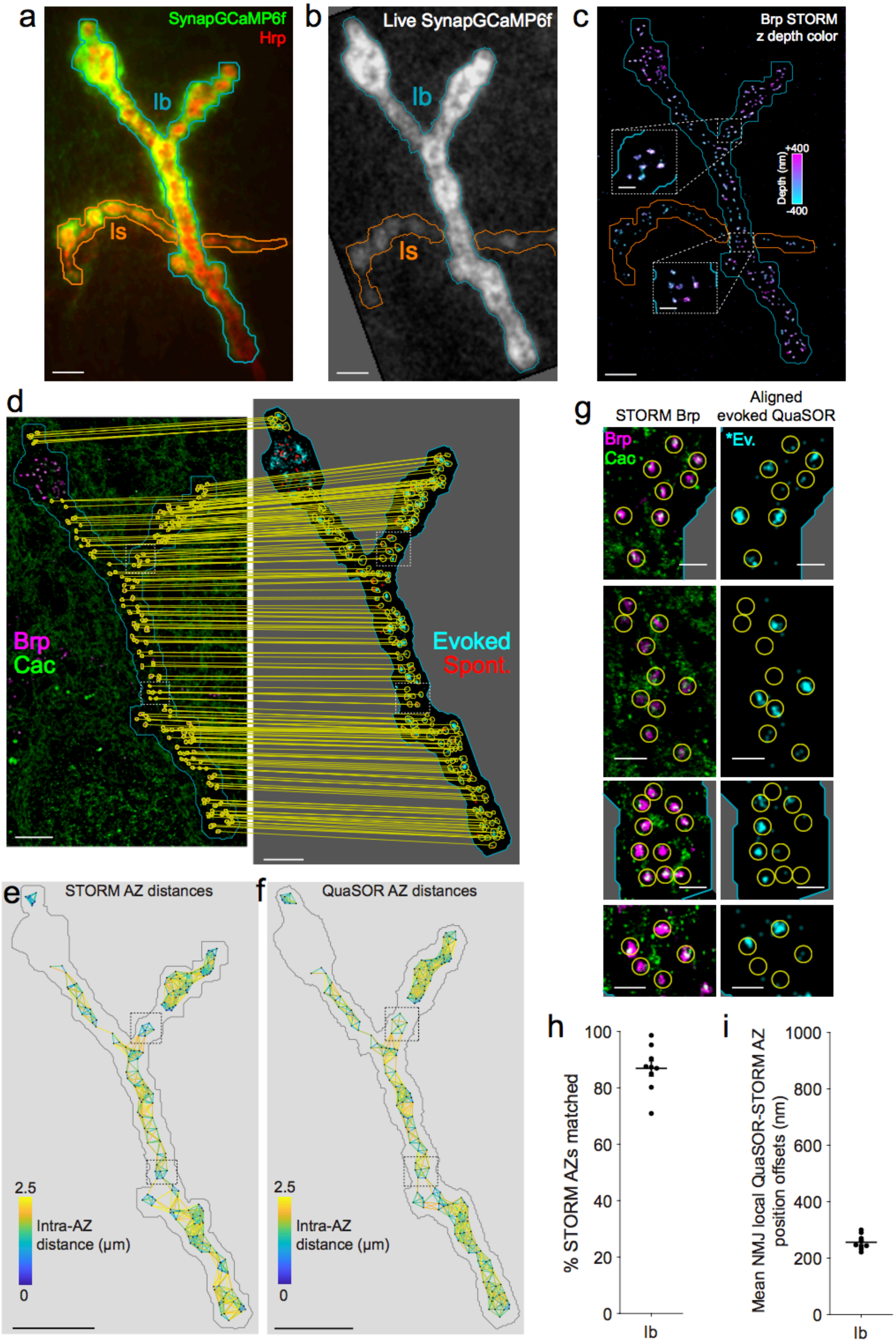
a
SynapGCaMP6f
Hrp
Ib
Is
b
Live SynapGCaMP6f
Ib
Is
c
Brp STORM
z depth color
Depth (nm)
+400
-400
d
Brp
Cac
Evoked
Spont.
g
STORM Brp
Aligned
evoked QuaSOR
Brp
Cac
*Ev.
e
STORM AZ distances
2.5
Intra-AZ
distance (µm)
0
f
QuaSOR AZ distances
2.5
Intra-AZ
distance (µm)
0
h
% STORM AZs matched
100
80
60
40
20
0
Ib
i
Mean NMJ local QuaSOR-STORM AZ
position offsets (nm)
1000
800
600
400
200
0
Ib

Supplementary Figure 2.6: QuaSOR matching to 3D-STORM AZ maps; related to Figure 2.3. **a**, SynapGCaMP6f (green) and motor neuron membrane (Hrp, red) reference image overlay collected immediately prior to STORM imaging for the example found in **Fig. 2.3** with Ib (cyan border) and Is (orange border) NMJ regions indicated. **b**, Live baseline SynapGCaMP6f fluorescence image rotated to the corresponding orientation of the STORM data in **a**. **c**, Brp *z*-position depth-colored STORM image with **Insets** showing small ROIs also found in **Fig. 2.3a-d**. **d-f**, QuaSOR-STORM AZ matching and alignment in an example Ib NMJ. **d**, Brp (magenta) and Cac (green) 3D-STORM *z*-projection image (**d, left**) and QuaSOR Ib NMJ area image (σ = 42.3 nm), showing evoked (cyan) and spontaneous (red) transmission events (**d, right**) with yellow lines connecting AZs to their corresponding transmission sites. **e,f**, A map of relative positions of AZs from STORM (e) shows a similar pattern to a map of relative positions of transmission sites from QuaSOR (f), **g**, Four example boutons from different NMJs at high magnification show close alignment of AZs imaged in STORM (left; Brp and Cac) and QuaSOR defined sites of evoked transmission (right; *evoked; σ = 42.3 nm). h,i, An average of ~85% of QuaSOR transmission sites could be matched to a STORM imaged AZ (h) with an average offset correction of 257.0 nm ±- 9.5 nm (i) (data are presented as mean ± SEM). Scale bars: 5 μm (**a-f**) and 1 μm (**g**).

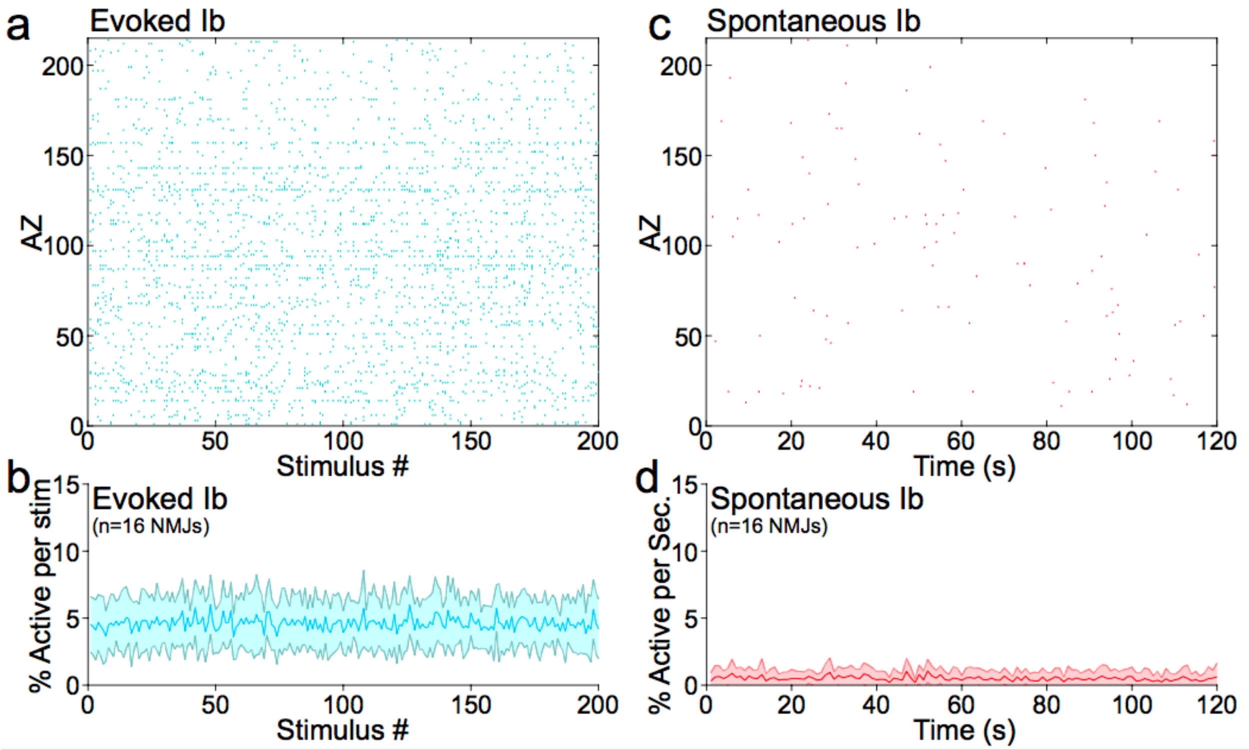

Supplementary Figure 2.7: Diversity in evoked and spontaneous activity patterns across AZs; related to Figure 2.3.

a, Heterogeneous evoked transmission patterns. Raster for a single Ib NMJ example in **Fig. 2.3a-d** and **Supplementary Fig. 2.4** showing all AZs and all 200 stimulus trials. **b**, Low percentage AP participation of Ib AZs. Mean percent of AZs participating in each evoked stimulus trial (n =16 Ib NMJs; data with error bands are presented as mean ± SEM). **c**, Extremely low spontaneous rates throughout the Ib NMJ. Spontaneous event raster for all Ib AZs representing four 30 s movies. **d,** Minimal spontaneous release of Ib AZs. Mean percent of AZs active per second for 120 s total of spontaneous event imaging (n = 16 Ib NMJs; data with error bands are presented as mean ± SEM).

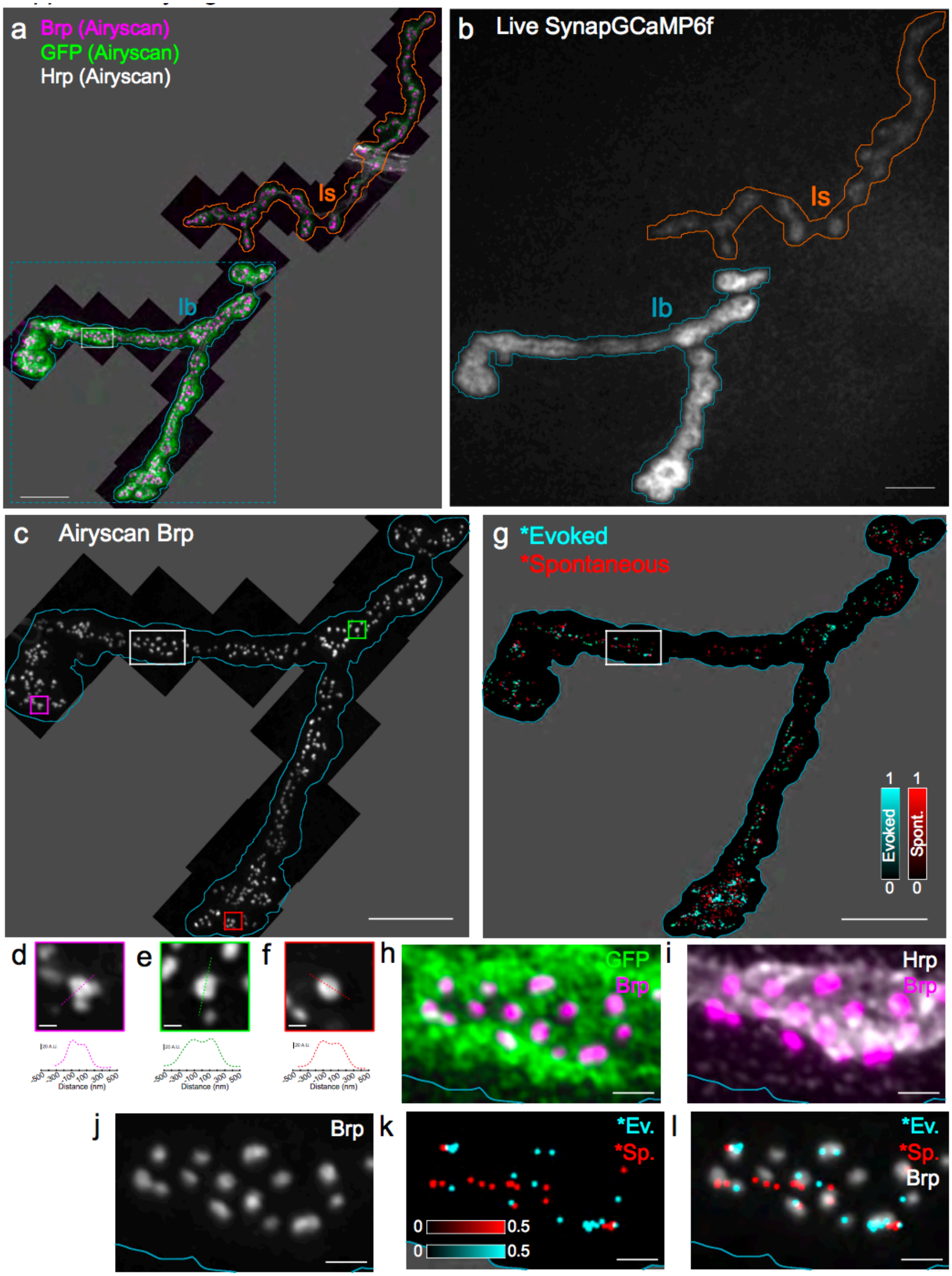
a
Brp (Airyscan)
GFP (Airyscan)
Hrp (Airyscan)
Is
Ib
b
Live SynapGCaMP6f
Is
Ib
c
Airyscan Brp
g
*Evoked
*Spontaneous
1
1
Evoked
Spont.
0
0
d
e
f
20 A.U.
-500 -300 -100 100 300 500
Distance (nm)
20 A.U.
-500 -300 -100 100 300 500
Distance (nm)
20 A.U.
-500 -300 -100 100 300 500
Distance (nm)
h
GFP
Brp
i
Hrp
Brp
j
Brp
k
*Ev.
*Sp.
0
0.5
0
0.5
l
*Ev.
*Sp.
Brp

Supplementary Figure 2.8: QuaSOR matching to 3D-Airyscan AZ maps; related to Figure 2.3.
a, Maximum intensity projection 3D-Airyscan tiled dataset for Brp (magenta), SynapGCaMP6f (green), and Hrp (gray). Areas outside the tiled region are indicated by the gray background with Ib (cyan border) and Is (orange border) axons indicated. **b**, Live baseline SynapGCaMP6f fluorescence image aligned to the Airyscan data in **a**. **c-f**, Maximum intensity projection 3D-Airyscan tiled dataset for the Ib axon showing only Brp (gray) (**c**) along with single *z*-slice images of the indicated three example *en face* oriented AZs along with a line intensity profile through each (**d-f**). Note that AZ dimensions are similar to those found with STORM in **Fig. 2**. **g**, Evoked (cyan) and spontaneous (red) Airyscan-aligned QuaSOR overlay image (σ = 63.5 nm) for the Ib NMJ in **c**. **h-l,** Local QuaSOR-Airyscan alignment showing the white rectangular ROI from **a,c,g**. Images include the ROI with Brp/SynapGCaMP6f overlay (**h**), the Brp/Hrp overlay (**i**), Brp only (**j**), the Airyscan-aligned spontaneous and evoked QuaSOR coordinates (Evoked, cyan; Spont, red; σ = 42.3 nm) (**k**) and the aligned QuaSOR overlaid on Brp (**l**). Scale bars: 10 μm (**a-c,g**), 400nm (**d-f**) and 1 μm (**h-l**).

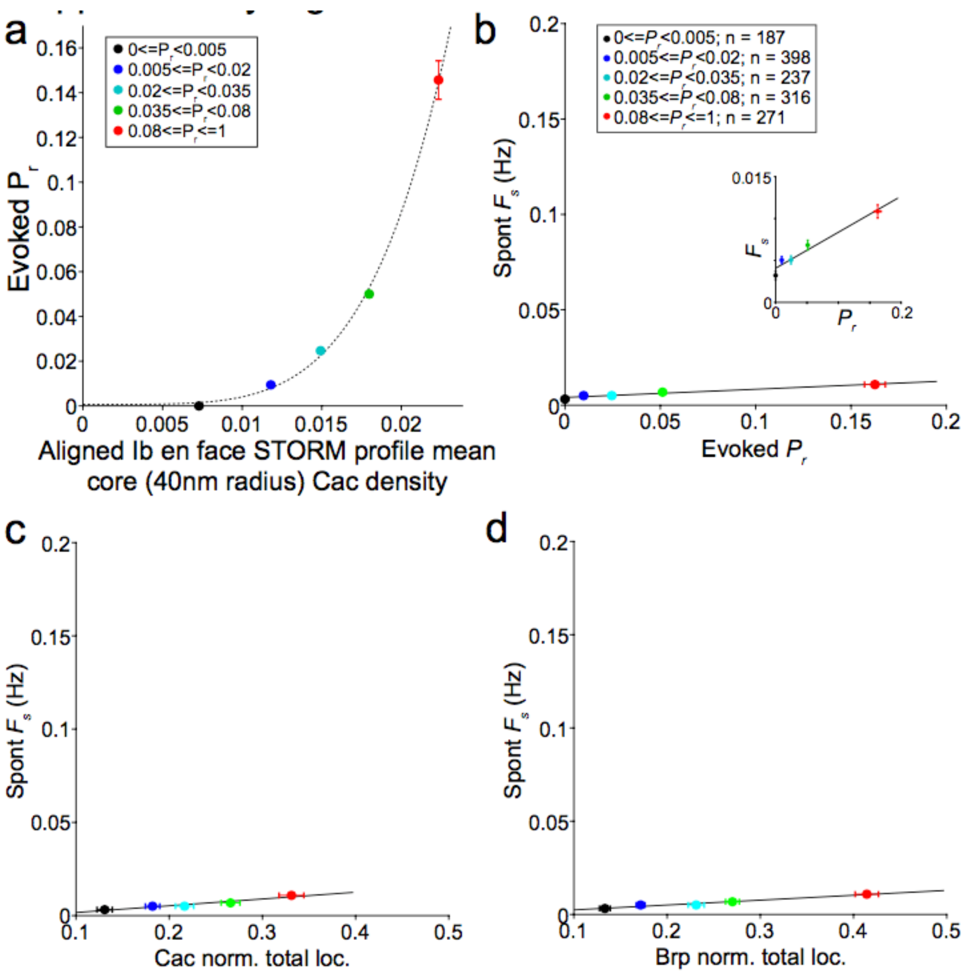

Supplementary Figure 2.9: Relationship between *P_r* and *F_S* and their dependence on Brp and Cac; related to Figure 2.4.
a, *P_r* dependence on core AZ Cac density. *P_r*-binned mean core Cac radial localization density (40 nm radius) versus mean binned AP-evoked *P_r* for *en face*-aligned AZ profile data plotted in **Fig. 3k** (R^2 = 0.999; $y=8*10^6 x^{4.7} +0.0007$). **b,** *P_r*-binned, mean *F_S* *versus* mean *P_r* from pooled Brp/Cac 3D-STORM matched to QuaSOR dataset for WT Ib AZs (all AZ orientations; 200 stim. 2 min spontaneous; R^2=0.958; y=0.043x+0.004; n = 1409 AZs from 9 NMJs). **Inset** shows a zoomed view of the relationship. **c**, *P_r*-binned, mean *F_S* *versus* mean Cac normalized total localizations per AZ for WT Ib AZs (QuaSOR-STORM dataset; R^2=0.929; y=0.036x-0.002; n = 1409 AZs from 9 NMJs). **d**, *P_r*-binned, mean *F_S* *versus* mean Brp normalized total localizations per AZ for WT Ib AZs (QuaSOR-STORM dataset; R^2=0.963; y=0.026x-0.0002; n = 1409 AZs from 9 NMJs).

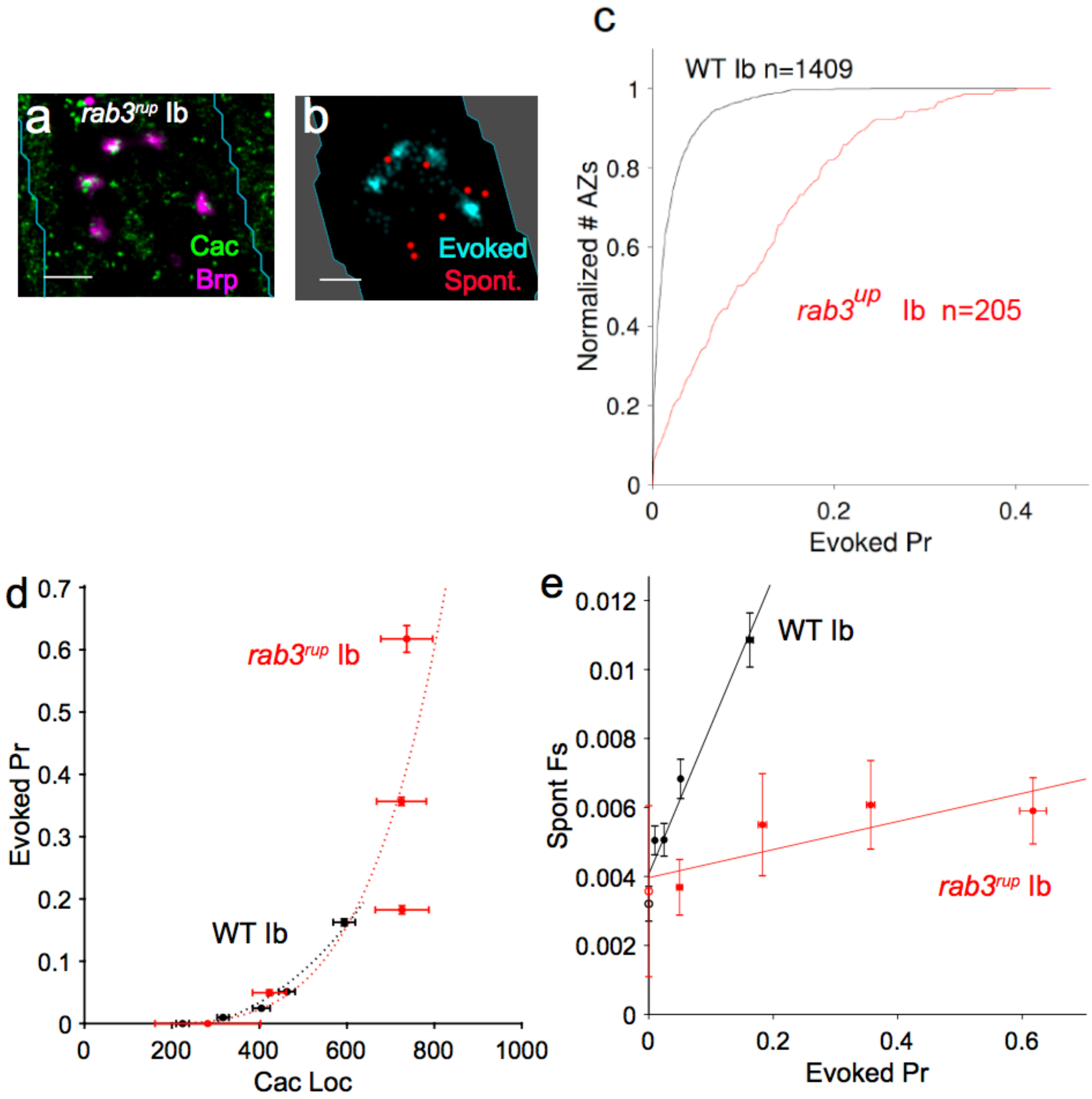

Supplementary Figure 2.10: Synaptic transmission in *rab3^{rup}* mutant; related to Figure 2.4. **a,b**, Aligned STORM and QuaSOR images from an example *rab3^{rup}* Ib bouton. **a**, STORM image showing localizations for Brp (magenta) and Cac (green). **b**, QuaSOR image showing localizations of spontaneous (red) and evoked (cyan) transmission events. **c**, Ib P_r distribution for *rab3^{rup}* (red) is shifted to higher P_r values compared to WT (black, WT data is from **Fig. 3e**; two-sample two-sided Kolmogorov–Smirnov test $p = 9.1 * 10^{-57}$). **d**, P_r – Cac STORM localization relation for *rab3^{rup}* is similar to that of WT but extends to higher values along both axes (data are presented as mean ± SEM). **e,** F_S - P_r relation is shallower in *rab3^{rup}* than in WT (data are presented as mean ± SEM).

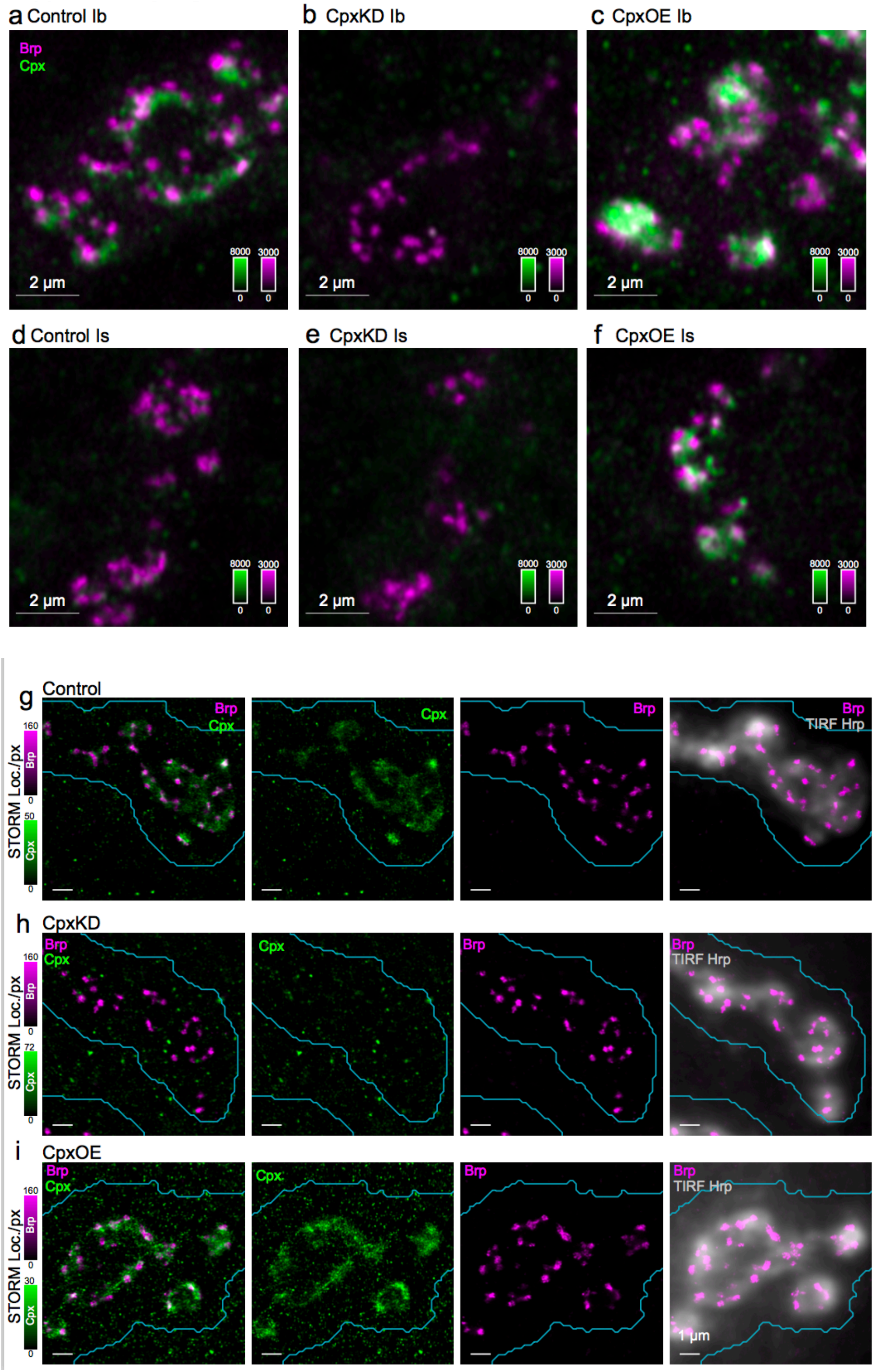
a Control Ib
b CpxKD Ib
c CpxOE Ib
Brp
Cpx
2 µm
8000
3000
0
0
d Control Is
e CpxKD Is
f CpxOE Is
g Control
h CpxKD
i CpxOE
STORM Loc./px
160
Brp
50
72
30
Cpx
TIRF Hrp
1 µm

Supplementary Figure 2.11: Cpx detection in Ib and Is boutons; related to Figure 2.5. **a-f**, Detection of Cpx in Airyscan. Example Airyscan maximum intensity *z*-projection images for boutons in Ib (**a-c**) and Is (**d-e**) axons of Control (**a,d**), CpxKD (**b,e**) and CpxOE (**c,f**). showing Brp (magenta;) and Cpx (green). Images acquired and processed with identical settings. **g-i,** STORM imaging of Ib terminal boutons from same Control (**g**), CpxKD (**h**) and CpxOE (**i**) genotypes as (**a-f**), with same antibody stains and color scheme, and adding merged images of Brp (magenta) and Hrp (white) on right. Genotypes were: Control (OK6-Gal4, attP40$^{\text{Empty}}$, SynapGCaMP6f), CpxKD (OK6-Gal4, UAS-Cpx$^{\text{RNAi}}$, SynapGCaMP6f) and CpxOE (OK6-Gal4, UAS-Cpx, SynapGCaMP6f. Scale bars: 2 (**a-f**), 1 µm (**g-i**).

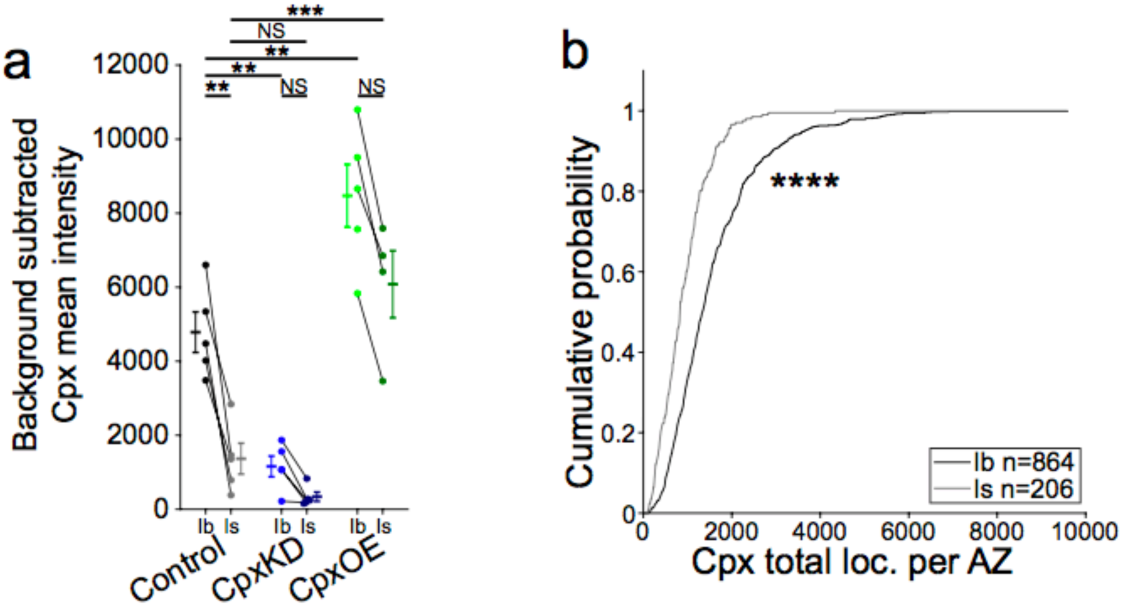

Supplementary Figure 2.12: Cpx expression in Ib and Is boutons; related to Figure 2.5.
a,b, Expression levels of Cpx in Ib and Is axons. **a**, Mean background subtracted terminal axon Cpx fluorescence intensity for Control (n = 5 Ib and n = 5 Is NMJs), CpxKD (n = 5 Ib and n = 5 Is NMJs), and CpxOE (n = 5 Ib and n = 3 Is NMJs) animals (data are presented as mean ± SEM; One-way ANOVA $p = 7.9*10^{-10}$ with Tukey-Kramer *post hoc* test Control Ib vs. Is $p = 0.0028$; CpxKD Ib vs. Is $p = 0.90$; CpxOE Ib vs. Is $p = 0.081$; Control Ib vs. CpxKD Ib $p = 0.0015$; Control Ib vs. CpxOE Ib $p = 0.0012$; Control Is vs. CpxKD Is $p = 0.78$; Control Is vs. CpxOE Is $p = 0.00012$). **b**, Type Ib synapses have higher levels of Cpx per AZ than does Is. Mean total Cpx 3D-STORM AZ localization pooled cumulative frequency distributions for WT Ib and Is axons (Ib n = 864 AZs from n = 7 NMJs; Is n = 206 AZs from n = 7 NMJs; two-sample two-sided Kolmogorov–Smirnov test $p = 2.4*10^{-16}$).

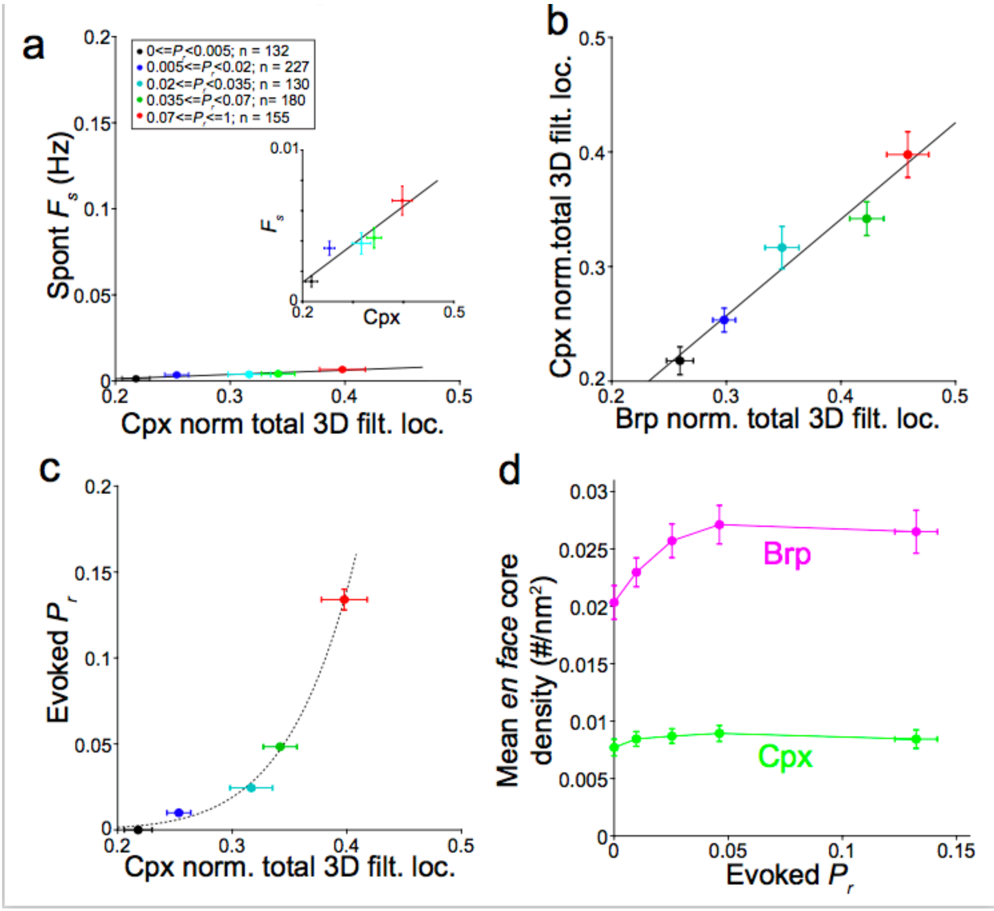

Supplementary Figure 2.13: Relationship between Cpx and Brp associated with differences in P_r; related to Figure 2.5.

a, Weak relationship between Cpx and F_S. P_r-binned, 3D-filtered (note, only localizations within ~80 nm of the Brp localization volume are counted), mean Cpx NMJ-normalized total localizations versus mean F_S for WT Ib AZs (QuaSOR-STORM dataset; all AZ orientations; 200 stim. 2 min spontaneous; R^2=0.884; y=0.025x-0.0038; data are presented as mean ± SEM). **Inset** shows a zoomed view of the relationship. **b**, Relationship between Brp and Cpx. P_r-binned, 3D-filtered, Brp versus Cpx mean NMJ-normalized total localizations for WT Ib AZs (R^2=0.960; y=0.84x+0.0045; data are presented as mean ± SEM). **c**, P_r dependence on Cpx. P_r-binned, 3D-filtered, mean Cpx NMJ-normalized total localizations per AZ versus mean P_r for WT Ib AZs (R^2=0.997; y=85x^7+0.0004; data are presented as mean ± SEM). **d**, Relationship between P_r, core Cpx density and core Brp density. P_r-binned, mean evoked P_r versus mean integrated core radial localization densities (40 nm radius) for Brp (magenta) or Cpx (green) in all *en face*-aligned AZs (data are presented as mean ± SEM).

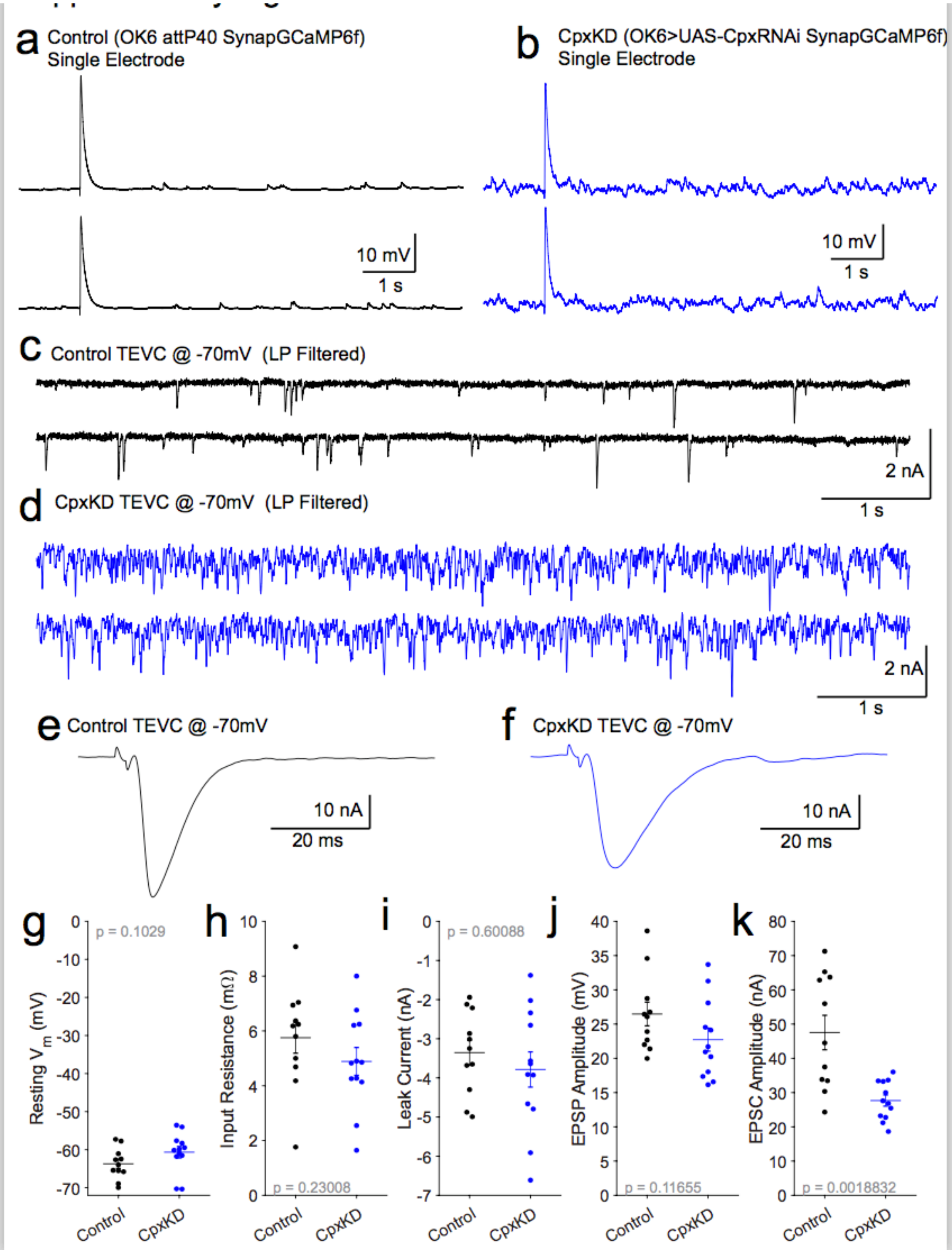
a
Control (OK6 attP40 SynapGCaMP6f)
Single Electrode
10 mV
1 s
b
CpxKD (OK6>UAS-CpxRNAi SynapGCaMP6f)
Single Electrode
10 mV
1 s
c
Control TEVC @ -70mV (LP Filtered)
2 nA
1 s
d
CpxKD TEVC @ -70mV (LP Filtered)
2 nA
1 s
e
Control TEVC @ -70mV
10 nA
20 ms
f
CpxKD TEVC @ -70mV
10 nA
20 ms
g
p = 0.1029
Resting V_m (mV)
0
-10
-20
-30
-40
-50
-60
-70
Control
CpxKD
h
Input Resistance (mΩ)
10
8
6
4
2
0
p = 0.23008
Control
CpxKD
i
p = 0.60088
Leak Current (nA)
0
-1
-2
-3
-4
-5
-6
-7
Control
CpxKD
j
EPSP Amplitude (mV)
40
35
30
25
20
15
10
5
0
p = 0.11655
Control
CpxKD
k
EPSC Amplitude (nA)
80
70
60
50
40
30
20
10
0
p = 0.0018832
Control
CpxKD

Supplementary Figure 2.14: Spontaneous and evoked transmission in the CpxKD; related to Figure 2.6. a-f, Comparison of synaptic transmission in Control (OK6-Gal4, attp40^{empty}, SynapGCaMP6f) to CpxKD (OK6-Gal4, UAS-Cpx^{RNAi}, SynapGCaMP6f). Evoked EPSP and spontaneous mEPSPs in Control **(a)** and CpxKD **(b)** measured in single electrode bridge recording. Spontaneous mEPSCs in Control (**c**) and CpxKD (**d**) and evoked EPSCs in Control **(e)** and CpxKD **(f)** measured in two-electrode voltage clamp (low-pass filtered). **g-i**, Muscle properties (resting potential, **g**; input resistance, **h**; leak current, **i**) are unchanged in CpxKD (data are presented as mean ± SEM). **g-i**, EPSP slightly decreased (but not statistically significant) (**j**) and EPSC significantly decreased (**k**) in CpxKD (data are presented as mean ± SEM). Smaller change in EPSP may be due to non-linear summation.

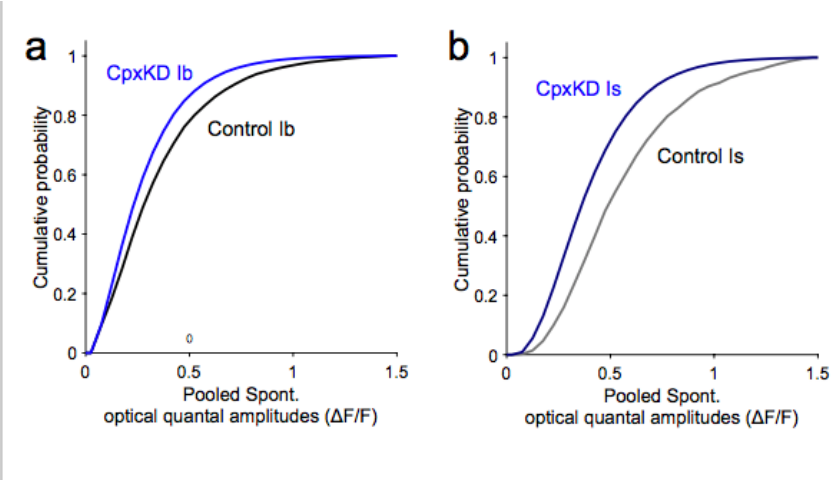

Supplementary Figure 2.15: CpxKD decreases optical spontaneous transmission event amplitude; related to Figure 2.6.
a,b, Optical spontaneous transmission event amplitude (∆F/F) decreased at both Ib (**a**) and Is **(b**) synapses by CpxKD.

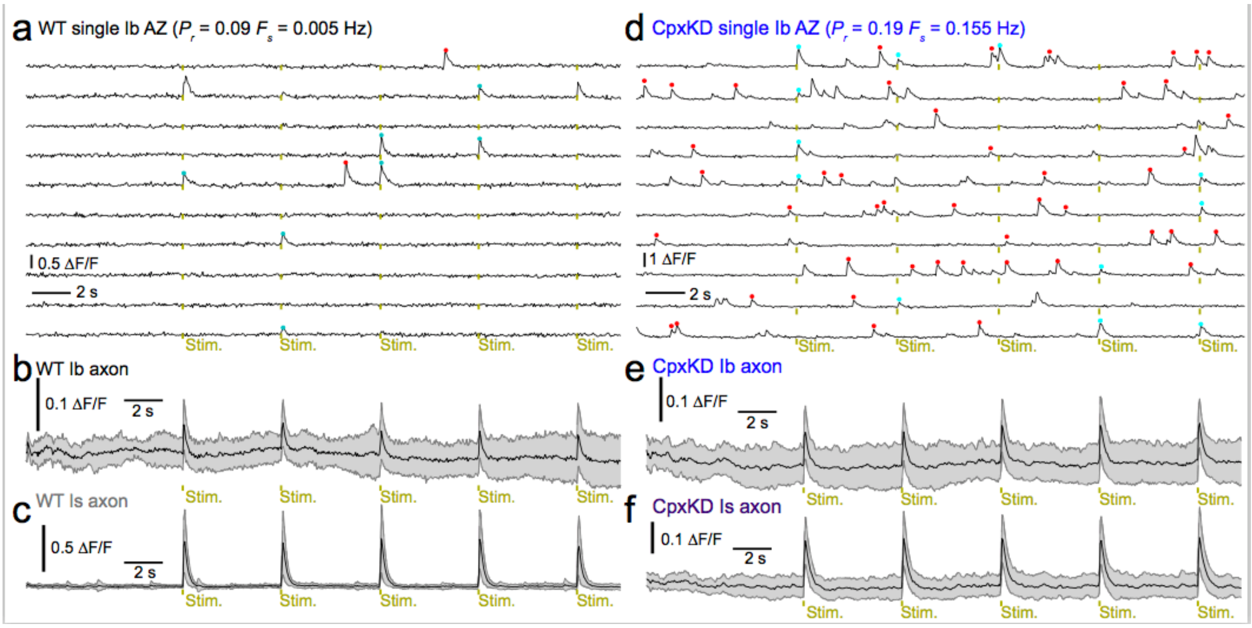

Supplementary Figure 2.16: CpxKD increases spontaneous transmission frequency; related to Figure 2.6.

a, Example ΔF/F traces from ten 30 s movies for a single AZ from a WT Ib QuaSOR-STORM matched NMJ. Synaptic transmission events elicited at that AZ are indicated by dots marking event peaks (cyan = evoked; red = spontaneous; no dot = event elicited elsewhere). Stimulus timing indicated below traces (yellow). Continuous imaging bouts with 5 stimuli per bout at 0.2 Hz. **b-c**, Mean ΔF/F traces for all AZs and all movies for a single WT Ib (**b**; n = 136 AZs and 20 movies) or Is (**c**; n = 44 AZs and 20 movies) NMJ (data with error bands are presented as mean ± SEM). **d**, Example ΔF/F traces from ten 30 s movies for a single AZ from a CpxKD (OK6-Gal4, UAS-Cpx^{RNAi}, SynapGCaMP6f) Ib QuaSOR-STORM matched NMJ. **e-f**, Mean ΔF/F traces for all AZs and all movies for a single CpxKD Ib (**e**; n = 617 AZs and 20 movies) or Is (**f;** n = 277 AZs and 20 movies) NMJ (data with error bands are presented as mean ± SEM).

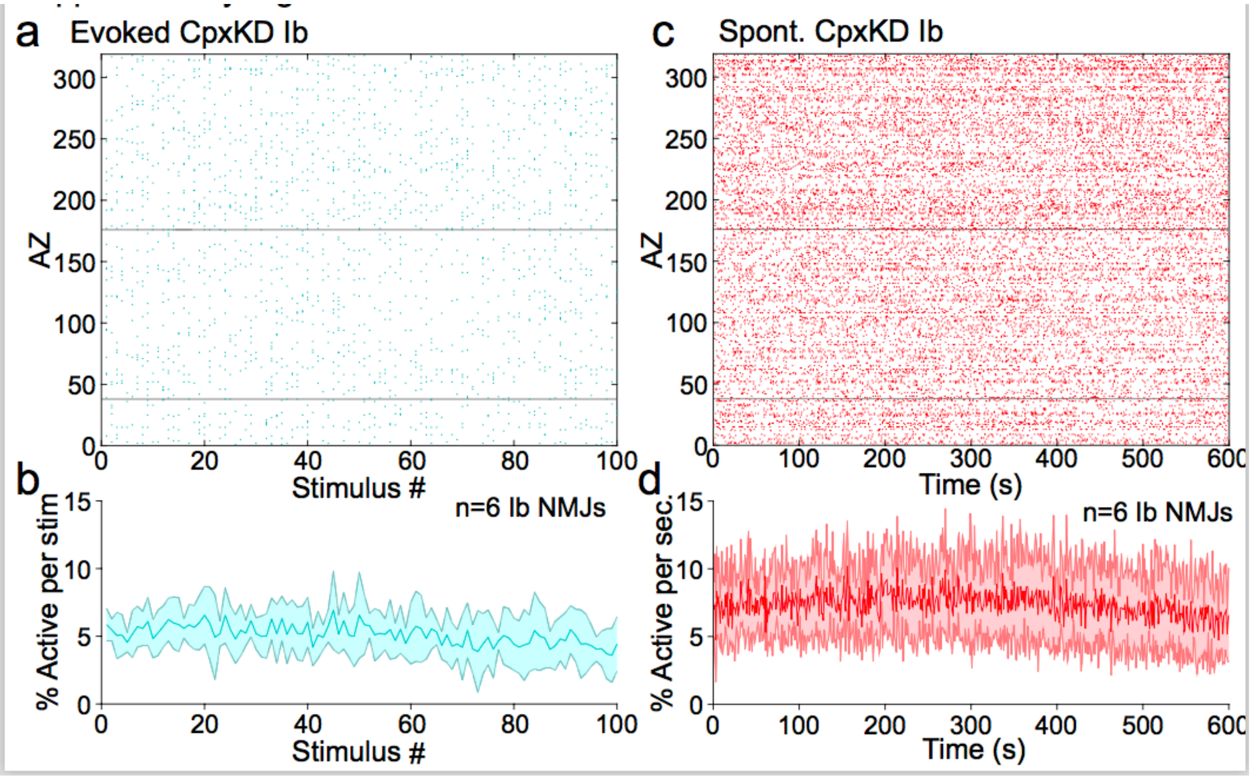

Supplementary Figure 2.17: CpxKD synapses retain diversity in evoked and spontaneous transmission throughout the NMJ; related to Figure 2.6.
a, Global evoked release heterogeneity in CpxKD Ib NMJs. CpxKD event raster for all evoked events at each AZ within the example NMJ in **Fig. 2.6**. Gray rows highlight AZs 38 and 176 from **Fig. 2.6**. **b**, CpxKD mean percent of active AZs for each evoked stimulus trial (100 stimuli; n = 6 NMJs; data with error bands are presented as mean ± SEM). **c**, High and diverse spontaneous release rates in CpxKD Ib NMJs. Raster for all detected spontaneous events (20, 30 s movies) at every type Ib AZ within the example NMJ. Gray rows highlight AZs 38 and 176 from **Fig. 2.6**. **d**, High spontaneous participation in CpxKD Ib NMJs. CpxKD mean percent of spontaneously active AZs per second (600 s; n = 6 NMJs; data with error bands are presented as mean ± SEM).

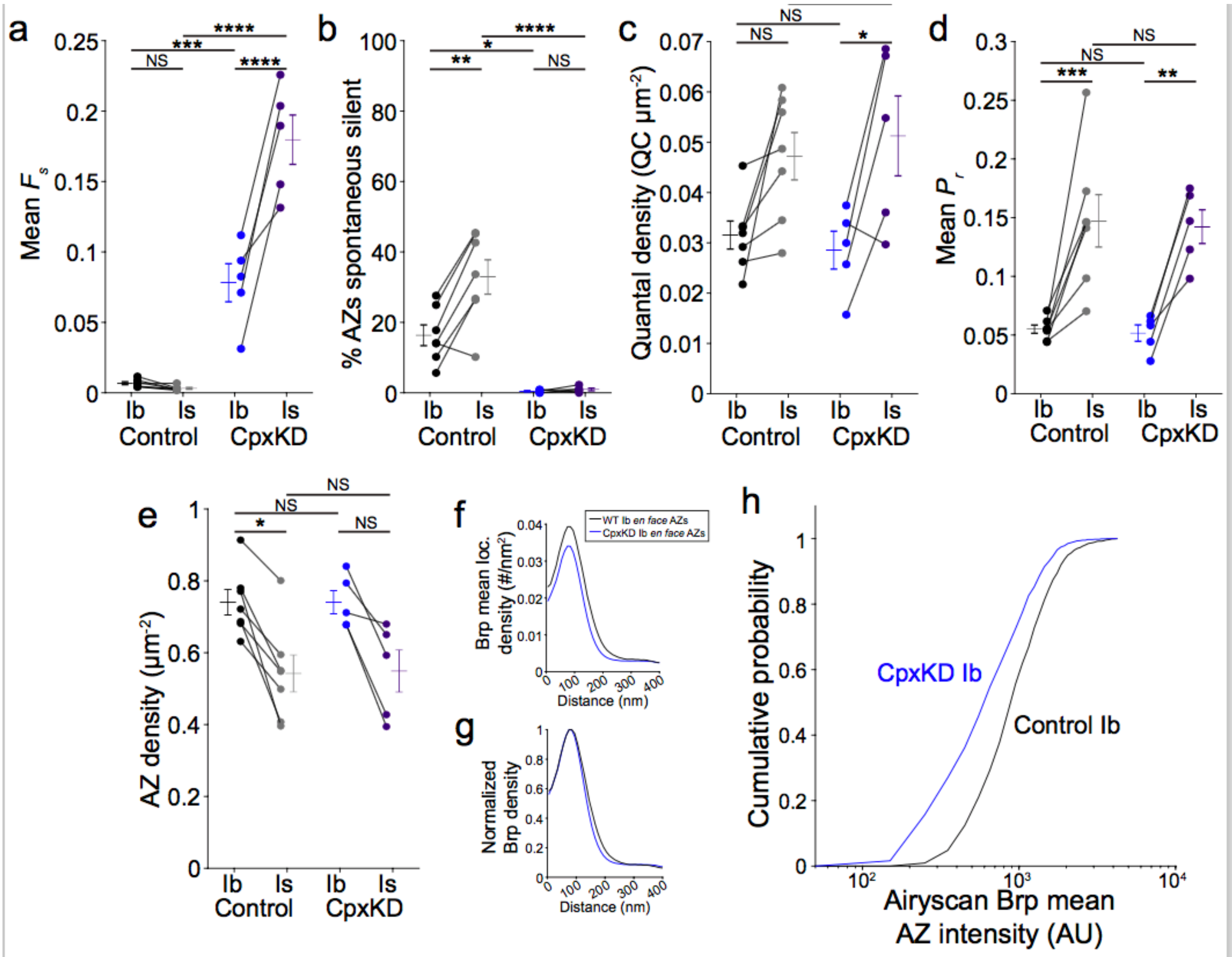

i

	WT Ib NMJs Brp/Alexa647 STORM (n = 407 AZs 2 NMJs)	CpxKD Ib NMJs Brp/Alexa647 STORM (n = 1774 AZs 6 NMJs)
Brp loc. per AZ	2436±62	1904±25****
% Difference		-21.8

	Control Ib NMJs Brp/Alexa405 Airyscan (n = 2333 AZs 7 NMJs)	CpxKD Ib NMJs Brp/Alexa405 Airyscan (n = 1482 AZs 5 NMJs)
Mean Brp intensity^{1,2}	1066±12	770±13****
% Difference		-27.7

	Control Ib NMJs Brp/Alexa555 Airyscan (n = 5656 AZs 11 NMJs)	CpxKD Ib NMJs Brp/Alexa555 Airyscan (n = 5010 AZs 10 NMJs)
Mean Brp intensity^{3}	3459±18	2660±17****
% Difference		-23.1

**** $p < 0.0001$ Kolmogorov-Smirnov Test

[1] see also Fig. 7O

[2] using automated 3D AZ Mask

[3] using fixed size 3D AZ Mask

Supplementary Figure 2.18: CpxKD increases F_S without altering evoked transmission or AZ density; related to Figure 2.7.

a, CpxKD increases F_S. Mean F_S per NMJ for QuaSOR-Airyscan matched Control Ib (n = 2709 AZs, 7 NMJs; OK6-Gal4, attP40$^{\mathrm{Empty}}$, SynapGCaMP6f), Control Is (n = 1114 AZs, 7 NMJs), CpxKD Ib (n = 1547 AZs, 5 NMJs; OK6-Gal4, UAS-Cpx$^{\mathrm{RNAi}}$, SynapGCaMP6f), and CpxKD Is (n = 697 AZs, 5 NMJs) animals (One-way ANOVA $p = 3.2*10^{-11}$; Tukey-Kramer *post hoc* test: Control Ib vs. Control Is $p = 0.99$; CpxKD Ib vs. CpxKD Is $p = 3.0*10^{-6}$; Control Ib vs. CpxKD Ib $p = 0.00012$; Control Is vs. CpxKD Is $p = 3.9*10^{-9}$). **b**, CpxKD NMJs lack sites with no spontaneous transmission. Percent of AZs with no spontaneous transmission (QuaSOR-Airyscan matched; One-way ANOVA $p = 2.2*10^{-6}$; Tukey-Kramer *post hoc* tests: Control Ib vs. Control Is $p = 0.0064$; CpxKD Ib vs. CpxKD Is $p = 0.999$; Control Ib vs. CpxKD Ib $p = 0.018$; Control Is vs. CpxKD Is $p = 1.1*10^{-5}$). **c**, CpxKD does not increase AP-evoked quantal density. Optical quantal density per NMJ (quantal content per μm^2 SynapGCaMP6f area; QuaSOR-Airyscan matched; One-way ANOVA $p = 0.0086$; Tukey-Kramer *post hoc* tests: Control Ib vs. Control Is $p = 0.094$; CpxKD Ib vs. CpxKD Is $p = 0.031$; Control Ib vs. CpxKD Ib $p = 0.97$; Control Is vs. CpxKD Is $p = 0.94$). **d**, CpxKD does not increase AP-evoked P_r. Mean AP-evoked P_r per NMJ (QuaSOR-Airyscan matched; One-way ANOVA $p = 2.2*10\text{-}6$; Tukey-Kramer *post hoc* tests: Control Ib vs. Control Is $p = 0.00067$; CpxKD Ib vs. CpxKD Is $p = 0.0042$; Control Ib vs. CpxKD Ib $p = 0.999$; Control Is vs. CpxKD Is $p = 0.99$). **e**, CpxKD does not increase AZ density. AZ density per NMJ (AZs per μm^2 NMJ area; QuaSOR- Airyscan matched; One-way ANOVA $p = 0.0041$; Tukey-Kramer *post hoc* tests: Control Ib vs. Control Is $p = 0.017$; CpxKD Ib vs. CpxKD Is $p = 0.061$; Control Ib vs. CpxKD Ib $p = 1$; Control Is vs. CpxKD Is $p = 0.999$). **f**-**g**, CpxKD Ib AZs similar in size to WT Ib. Pooled *en face*-aligned AZ radial density profiles (**f**) for WT Ib (black; n = 129 AZs, 2 NMJs) and CpxKD (blue; n = 655 AZs, 6 NMJs) and corresponding normalized radial density profiles (**g**). **h**, Reduced Brp in CpxKD Ib. Distributions for mean Airyscan Brp voxel intensities for Control Ib (n = 2333 AZs, 7 NMJs) and CpxKD Ib (n=1482 AZs, 5 NMJs) AZs (two- sample two-sided Kolmogorov–Smirnov test $p = 3.0*10^{-52}$). **i**, Additional evidence for reduced Brp in CpxKD STORM and Airyscan (two-sample two-sided Kolmogorov–Smirnov tests; mean ± SEM).

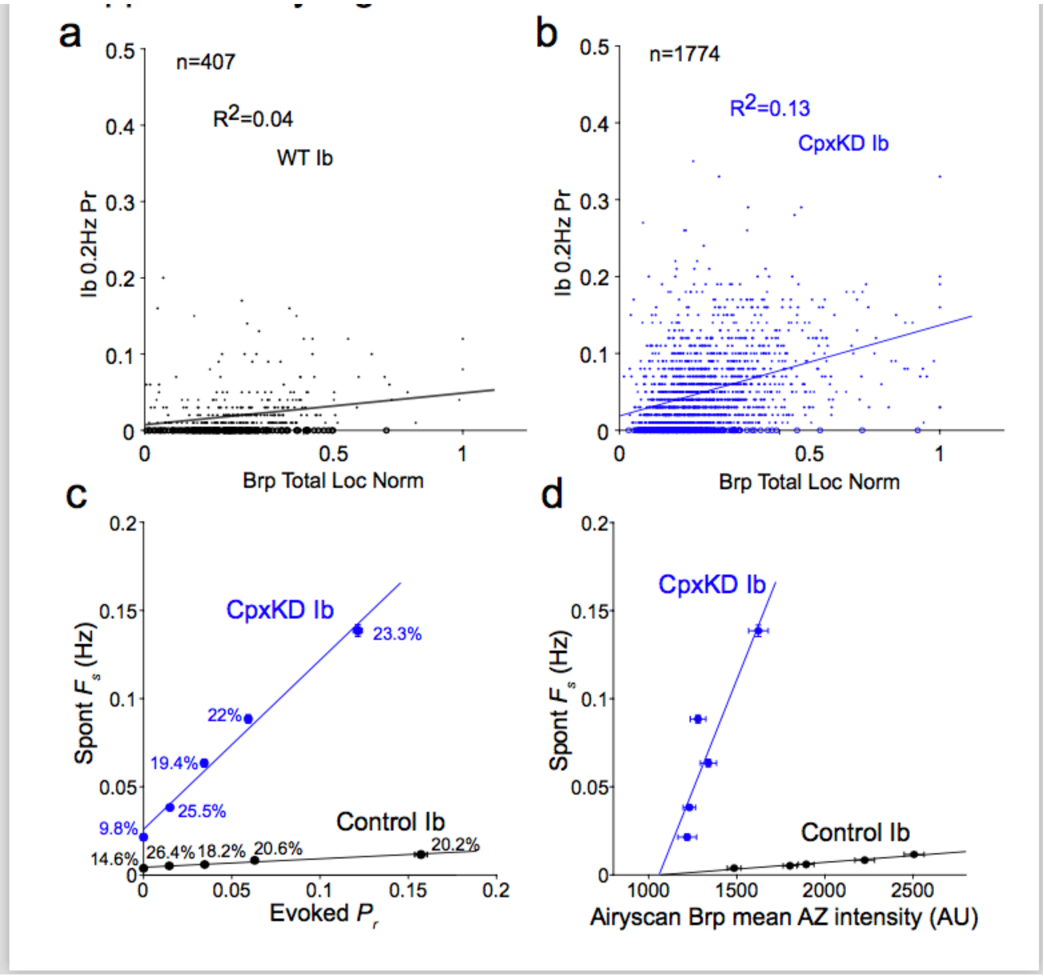

Supplementary Figure 2.19: Knockdown of Cpx dramatically steepens the relationship between evoked (*P_r*) and spontaneous (*F_S*) transmission and the dependence of *P_r* and *F_S* on Brp content; related to Figure 2.7.

a,b, F_S dependence on Brp is increased in the CpxKD (**b**) compared to WT (**a**). **c**, F_S highly related to P_r in CpxKD NMJs. QuaSOR-Airyscan matched, P_r-binned, mean P_r *versus* mean F_S data for pooled Control Ib AZs (black; OK6-Gal4, attP40$^{\text{Empty}}$, SynapGCaMP6f; n=2709 AZs from 7 NMJs; $y=0.048x+0.0044$; $R^2 = 0.965$) and CpxKD Ib AZs (blue; OK6-Gal4, UAS-Cpx$^{\text{RNAi}}$, SynapGCaMP6f; n=1547 AZs 5 NMJs; $y=0.96x+0.026$; $R^2 = 0.989$) (data are presented as mean ± SEM). **D**, F_S dependence on Brp is greatly increased in the CpxKD. QuaSOR-Airyscan matched, P_r-binned, mean Brp voxel intensity *versus* mean F_S for pooled Control Ib AZs (black; $y=7.63*10^{-6}x-0.0081$; $R^2 = 0.963$) and CpxKD Ib AZs (blue; $y=2.51*10^{-4}x-0.027$; $R^2 = 0.821$) (data are presented as mean ± SEM).

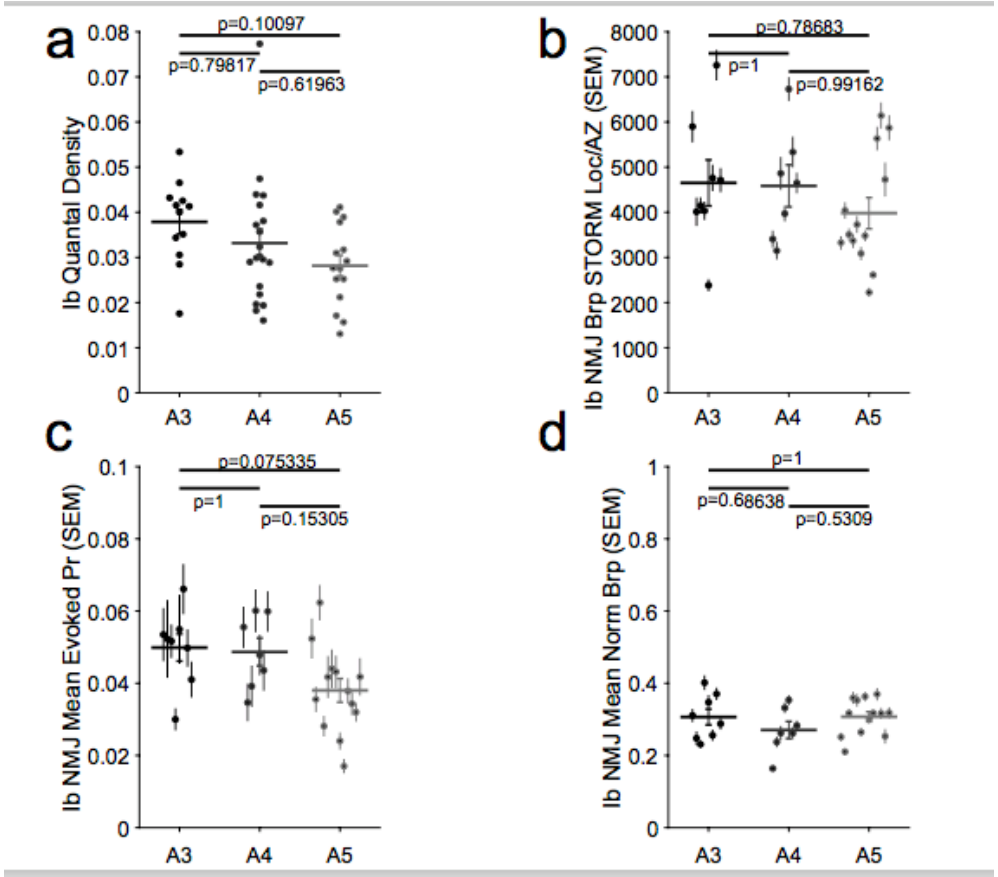

Supplementary Figure 2.20: Minimal differences between Ib synapses onto muscle 4 in segments A3- A5, related to Figures 2.1-2.7.

Ib synapses onto muscle 4 are similar in quantal density (a; One-way ANOVA *p* = 0.10 with Tukey-Kramer *posthoc*testA3vsA4*p*=0.50;A4vsA5*p*=0.41;A3vsA5*p*=0.084),averageP_r (b;One-wayANOVA *p* = 0.028 with Tukey-Kramer *post hoc* test A3 vs A4 *p* = 0.96; A4 vs A5 *p* = 0.10; A3 vs A5 *p* = 0.042), Brp STORM localizations per AZ (c; One-way ANOVA *p* = 0.45 with Tukey-Kramer *post hoc* test A3 vs A4 *p* = 0.99; A4 vs A5 *p* = 0.62; A3 vs A5 *p* = 0.49) and average normalized Brp localizations per AZ (d; One-way ANOVA *p* = 0.32 with Tukey-Kramer *post hoc* test A3 vs A4 *p* = 0.41; A4 vs A5 *p* = 0.33; A3 vs A5 *p* = 0.99).

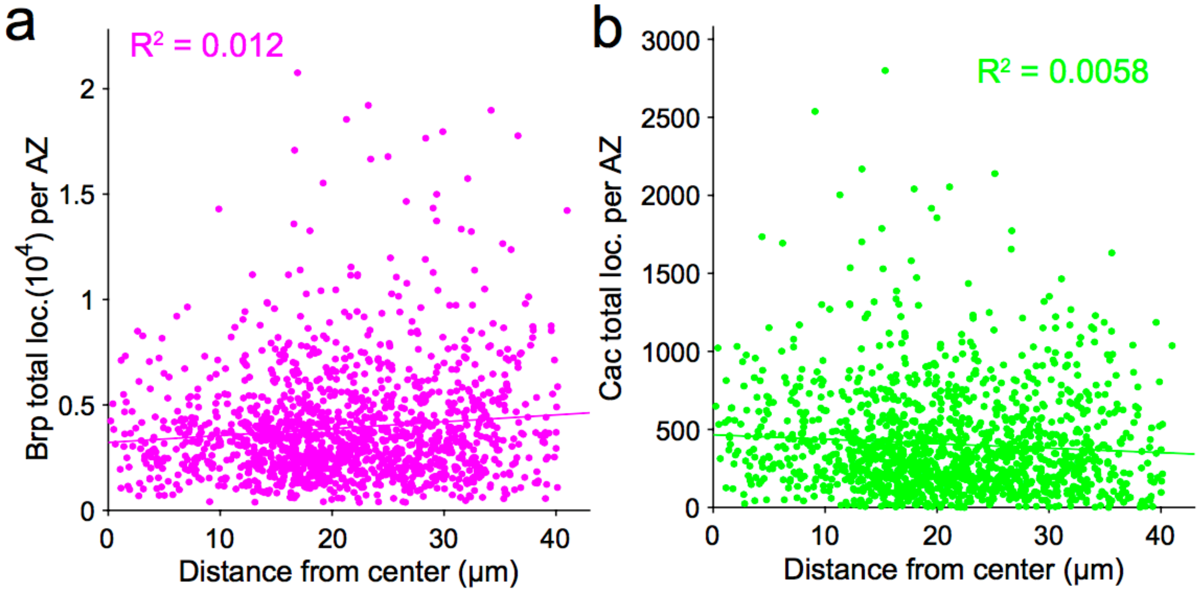

Supplementary Figure 2.21: Uniform STORM excitation across field of view, related to Figures 2.2, 2.3, 2.5 and 2.6. (a) and Cac (b) localizations per AZ as a function of radial distance from the center of the FOV show uniformity (~5% trend in opposite directions for Brp and Cac) in TIRF excitation for STORM imaging over the range of radial distances (linear regressions indicated; a, y=32.7x+3220 R^2 = 0.012; b, Cac y = - 2.87x+466 R^2 =0.0058).

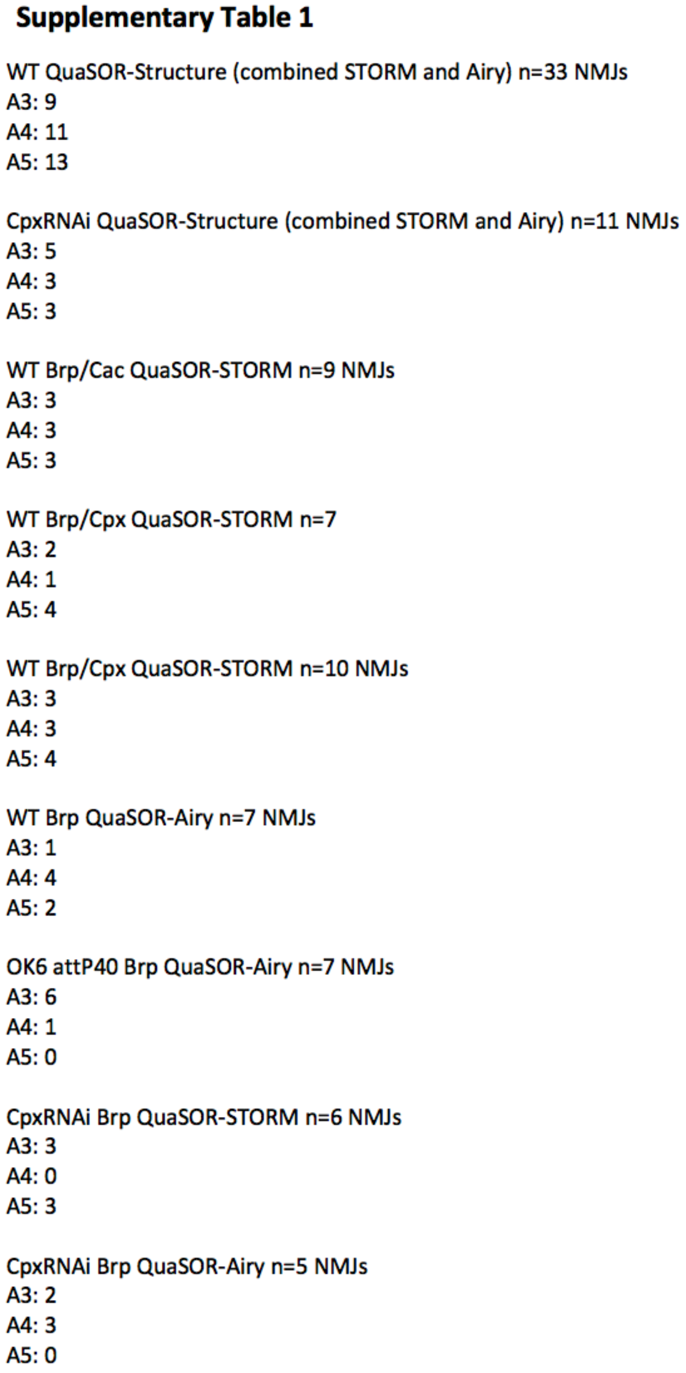

Supplementary Table 1

WT QuaSOR-Structure (combined STORM and Airy) n=33 NMJs
A3: 9
A4: 11
A5: 13

CpxRNAi QuaSOR-Structure (combined STORM and Airy) n=11 NMJs
A3: 5
A4: 3
A5: 3

WT Brp/Cac QuaSOR-STORM n=9 NMJs
A3: 3
A4: 3
A5: 3

WT Brp/Cpx QuaSOR-STORM n=7
A3: 2
A4: 1
A5: 4

WT Brp/Cpx QuaSOR-STORM n=10 NMJs
A3: 3
A4: 3
A5: 4

WT Brp QuaSOR-Airy n=7 NMJs
A3: 1
A4: 4
A5: 2

OK6 attP40 Brp QuaSOR-Airy n=7 NMJs
A3: 6
A4: 1
A5: 0

CpxRNAi Brp QuaSOR-STORM n=6 NMJs
A3: 3
A4: 0
A5: 3

CpxRNAi Brp QuaSOR-Airy n=5 NMJs
A3: 2
A4: 3
A5: 0

Supplementary Table 2.1. Summary of experiments. Number of muscle-4 NMJs (one per larva) along with abdominal segment identity (A3-A5) for each experimental set.

References

1. Borczyk, M., Śliwińska, M. A., Caly, A., Bernas, T. & Radwanska, K. Neuronal plasticity affects correlation between the size of dendritic spine and its postsynaptic density. *Sci. Rep.* **9**, 1–12 (2019).
2. Holtmaat, A. & Svoboda, K. Experience-dependent structural synaptic plasticity in the mammalian brain. *Nat. Rev. Neurosci.* **10**, 647–658 (2009).
3. Nusser, Z. *et al.* Cell type and pathway dependence of synaptic AMPA receptor number and variability in the hippocampus. *Neuron* **21**, 545–559 (1998).
4. Tanaka, J. I. *et al.* Number and density of AMPA receptors in single synapses in immature cerebellum. *J. Neurosci.* **25**, 799–807 (2005).
5. Holler-Rickauer, S., Köstinger, G., Martin, K., Schuhknecht, G. & Stratford, K. Structure and function of a neocortical synapse. *bioRxiv* (2019). doi:10.1101/2019.12.13.875971
6. Matz, J., Gilyan, A. & Kolar, A. Rapid structural alterations of the active zone lead to sustained changes in neurotransmitter release. *Proc. Natl. Acad. Sci.* **107**, 8836–8841 (2010).
7. Schikorski, T. & Stevens, C. F. Quantitative Ultrastructural Analysis of Hippocampal Excitatory Synapses. *J. Neurosci.* **17**, 5858–5867 (1997).
8. Holderith, N. *et al.* Release probability of hippocampal glutamatergic terminals scales with the size of the active zone. *Nat. Neurosci.* **15**, 988–997 (2012).
9. Branco, T., Marra, V. & Staras, K. Examining size – strength relationships at hippocampal synapses using an ultrastructural measurement of synaptic release probability. *J. Struct. Biol.* **172**, 203–210 (2010).
10. Murthy, V. N., Schikorski, T., Stevens, C. F. & Zhu, Y. Inactivity Produces Increases in Neurotransmitter Release and Synapse Size. *Neuron* **32**, 673–682 (2001).
11. O’Rourke, N. A., Weiler, N. C., Micheva, K. D. & Smith, S. J. Deep molecular diversity of mammalian synapses: why it matters and how to measure it. *Nat. Rev. Neurosci.* **13**, 365–79 (2012).
12. Fekete, A. *et al.* Underpinning heterogeneity in synaptic transmission by presynaptic ensembles of distinct morphological modules. *Nat. Commun.* **10**, 826 (2019).
13. Nusser, Z. Creating diverse synapses from the same molecules. *Current Opinion in Neurobiology* **51**, 8–15 (2018).
14. Südhof, T. C. The presynaptic active zone. *Neuron* **75**, 11–25 (2012).

15. Körber, C. & Kuner, T. Molecular Machines Regulating the Release Probability of Synaptic Vesicles at the Active Zone. *Front. Synaptic Neurosci.* **8**, fnsyn.2016.00005 (2016).

16. Brunger, A. T., Choi, U. B., Lai, Y., Leitz, J. & Zhou, Q. Molecular Mechanisms of Fast Neurotransmitter Release. *Annu. Rev. Biophys.* **47**, 469–497 (2018).

17. Rizo, J. & Xu, J. The Synaptic Vesicle Release Machinery. *Annu. Rev. Biophys.* **44**, 339–367 (2015).

18. Dittman, J. S. & Ryan, T. A. The control of release probability at nerve terminals. *Nat. Rev. Neurosci.* **20**, (2019).

19. Yuste, R., Majewska, A., Cash, S. S. & Denk, W. Mechanisms of calcium influx into hippocampal spines: heterogeneity among spines, coincidence detection by NMDA receptors, and optical quantal analysis. *J. Neurosci.* **19**, 1976–87 (1999).

20. Oertner, T. G., Sabatini, B. L., Nimchinsky, E. A. & Svoboda, K. Facilitation at single synapses probed with optical quantal analysis. *Nat. Neurosci.* **5**, 657–64 (2002).

21. Emptage, N. J., Reid, C. A., Fine, A. & Bliss, T. V. P. Optical quantal analysis reveals a presynaptic component of LTP at hippocampal Schaffer-associational synapses. *Neuron* **38**, 797–804 (2003).

22. Reid, C. A., Dixon, D. B., Takahashi, M., Bliss, T. V. P. & Fine, A. Optical quantal analysis indicates that long-term potentiation at single hippocampal mossy fiber synapses is expressed through increased release probability, recruitment of new release sites, and activation of silent synapses. *J. Neurosci.* **24**, 3618–26 (2004).

23. Koester, H. J. & Johnston, D. Target Cell – Dependent Normalization of Transmitter Release at Neocortical Synapses. *Science* **308**, 863–866 (2005).

24. Ward, B. *et al.* State-dependent mechanisms of LTP expression revealed by optical quantal analysis. *Neuron* **52**, 649–61 (2006).

25. Enoki, R., Hu, Y.-L., Hamilton, D. & Fine, A. Expression of long-term plasticity at individual synapses in hippocampus is graded, bidirectional, and mainly presynaptic: optical quantal analysis. *Neuron* **62**, 242–53 (2009).

26. Padamsey, Z., Tong, R. & Emptage, N. Optical Quantal Analysis Using Ca2+ Indicators: A Robust Method for Assessing Transmitter Release Probability at Excitatory Synapses by Imaging Single Glutamate Release Events. *Front. Synaptic Neurosci.* **11**, 1–11 (2019).

27. MacDougall, M. J. & Fine, A. Optical Quantal Analysis. *Front. Synaptic Neurosci.* **11**, fnsyn.2019.00008 (2019).

28. Newman, Z. L. *et al.* Input-specific plasticity and homeostasis at the Drosophila

larval neuromuscular junction. *Neuron* **93**, 1388–1404 (2017).

29. Akbergenova, Y., Cunningham, K. L., Zhang, Y. V., Weiss, S. & Littleton, J. T. Characterization of developmental and molecular factors underlying release heterogeneity at drosophila synapses. *Elife* **7**, 1–37 (2018).

30. Gratz, S. J. *et al.* Endogenous tagging reveals differential regulation of Ca2+ channels at single active zones during presynaptic homeostatic potentiation and depression. *J. Neurosci.* **39**, 2416–2429 (2019).

31. Melom, J. E., Akbergenova, Y., Gavornik, J. P. & Littleton, J. T. Spontaneous and Evoked Release Are Independently Regulated at Individual Active Zones. *J. Neurosci.* **33**, 17253–17263 (2013).

32. Reddy-Alla, S. *et al.* Stable Positioning of Unc13 Restricts Synaptic Vesicle Fusion to Defined Release Sites to Promote Synchronous Neurotransmission. *Neuron* **95**, 1350-1364.e12 (2017).

33. Peled, E. S., Newman, Z. L. & Isacoff, E. Y. Evoked and spontaneous transmission favored by distinct sets of synapses. *Curr. Biol.* **24**, 484–493 (2014).

34. Peled, E. S. & Isacoff, E. Y. Optical quantal analysis of synaptic transmission in wild-type and rab3-mutant Drosophila motor axons. *Nat. Neurosci.* **14**, 519–526 (2011).

35. Sabatini, B. L. & Tian, L. Imaging Neurotransmitter and Neuromodulator Dynamics In Vivo with Genetically Encoded Indicators. *Neuron* **108**, 17–32 (2020).

36. Ariel, P. & Ryan, T. A. Optical mapping of release properties in synapses. *Front. Neural Circuits* **4**, fncir.2010.00018 (2010).

37. Tang, A.-H. *et al.* A trans-synaptic nanocolumn aligns neurotransmitter release to receptors. *Nature* **536**, 210–214 (2016).

38. Gramlich, M. W. & Klyachko, V. A. Nanoscale Organization of Vesicle Release at Central Synapses. *Trends Neurosci.* **42**, 425–437 (2019).

39. Kawasaki, F. Active Zone Localization of Presynaptic Calcium Channels Encoded by the cacophony Locus of Drosophila. *J. Neurosci.* **24**, 282–285 (2004).

40. Jan, L. Y. & Jan, Y. N. Properties of the larval neuromuscular junction in Drosophila melanogaster. *J Physiol.* **262**, 189–214 (1976).

41. Dodge, F. J. & Rahamimoff, R. Co-operative action of calcium ions in transmitter release at the neuromuscular junction. *J Physiol* **193**, 419–432 (1967).

42. Schneggenburger, R. & Neher, E. Intracellular calcium dependence of transmitter release rates at a fast central synapse. *Nature* **406**, 889–93 (2000).

43. Borst, J. G. G. & Sakmann, B. Calcium influx and transmitter release in a fast CNS synapse. *Nature* **383**, 431–434 (1996).

44. Kittel, R. J. *et al.* Bruchpilot promotes active zone assembly, Ca2+ channel clustering, and vesicle release. *Science* **312**, 1051–4 (2006).

45. Wagh, D. A. *et al.* Bruchpilot, a protein with homology to ELKS/CAST, is required for structural integrity and function of synaptic active zones in Drosophila. *Neuron* **49**, 833–44 (2006).

46. Hallermann, S. *et al.* Naked dense bodies provoke depression. *J. Neurosci.* **30**, 14340–5 (2010).

47. Huntwork, S. & Littleton, J. T. A complexin fusion clamp regulates spontaneous neurotransmitter release and synaptic growth. *Nat. Neurosci.* **10**, 1235–1237 (2007).

48. Trimbuch, T. & Rosenmund, C. Should I stop or should I go? The role of complexin in neurotransmitter release. *Nature Reviews Neuroscience* **17**, 118–125 (2016).

49. Han, T. H., Dharkar, P., Mayer, M. L. & Serpe, M. Functional reconstitution of Drosophila melanogaster NMJ glutamate receptors. *Proc. Natl. Acad. Sci.* **112**, 6182–7 (2015).

50. Small, A. & Stahlheber, S. Fluorophore localization algorithms for super-resolution microscopy. *Nat. Methods* **11**, 267–279 (2014).

51. Maschi, D. & Klyachko, V. A. Spatiotemporal Regulation of Synaptic Vesicle Fusion Sites in Central Synapses. *Neuron* **94**, 65–73 (2017).

52. Farsi, Z. *et al.* Single-Vesicle imaging reveals different transport mechanisms between glutamatergic and GABAergic vesicles. *Science* **351**, 981–984 (2016).

53. Rust, M. J., Bates, M. & Zhuang, X. Sub-diffraction-limit imaging by stochastic optical reconstruction microscopy (STORM). *Nat. Methods* **3**, 793–795 (2006).

54. Huang, B., Wang, W., Bates, M. & Zhuang, X. Three-Dimensional Super-Resolution Reconstruction Microscopy. *Science* **319**, 810–813 (2008).

55. Bossi, M. *et al.* Multicolor far-field fluorescence nanoscopy through isolated detection of distinct molecular species. *Nano Lett.* **8**, 2463–2468 (2008).

56. Testa, I. *et al.* Multicolor fluorescence nanoscopy in fixed and living cells by exciting conventional fluorophores with a single wavelength. *Biophys. J.* **99**, 2686–2694 (2010).

57. Chang, J., Hazelett, D. J., Stewart, J. A. & Morton, D. B. Motor neuron expression of the voltage-gated calcium channel cacophony restores locomotion defects in a

Drosophila , TDP-43 loss of function model of ALS. *Brain Res.* **1584**, 39–51 (2014).

58. Ehmann, N. *et al.* Quantitative super-resolution imaging of Bruchpilot distinguishes active zone states. *Nat. Commun.* **5**, ncomms5650 (2014).
59. Fouquet, W. *et al.* Maturation of active zone assembly by Drosophila Bruchpilot. *J. Cell Biol.* **186**, 129–45 (2009).
60. Broeken, J. *et al.* Resolution improvement by 3D particle averaging in localization microscopy. *Methods Appl. Fluoresc.* **3**, 014003 (2015).
61. Szymborska, A. *et al.* Nuclear pore scaffold structure analyzed by super-resolution microscopy and particle averaging. *Science* **341**, 655–658 (2013).
62. Wu, Y. Le, Tschanz, A., Krupnik, L. & Ries, J. Quantitative Data Analysis in Single-Molecule Localization Microscopy. *Trends Cell Biol.* **30**, 837–851 (2020).
63. Liu, K. S. Y. *et al.* RIM-Binding Protein, a Central Part of the Active Zone, Is Essential for Neurotransmitter Release. *Science* **334**, 1565–1569 (2011).
64. Weisshart, K. The Basic Principle of Airyscanning The Basic Principle of Airyscanning. *Zeiss Microsc.* 22 (2014).
65. Wiegand, T. & Moloney, K. A. Rings, circles, and null-models for point pattern analysis in ecology. *Oikos* **104**, 209–229 (2004).
66. Iyer, J., Wahlmark, C. J., Kuser-Ahnert, G. A. & Kawasaki, F. Molecular mechanisms of COMPLEXIN fusion clamp function in synaptic exocytosis revealed in a new Drosophila mutant. *Mol. Cell. Neurosci.* **56**, 244–54 (2013).
67. Robinson, S. W. *et al.* Nitric oxide-mediated posttranslational modifications control neurotransmitter release by modulating complexin farnesylation and enhancing its clamping ability. *PLOS Biol.* **16**, e2003611 (2018).
68. Buhl, L. K. *et al.* Differential regulation of evoked and spontaneous neurotransmitter release by C-terminal modifications of complexin. *Mol. Cell. Neurosci.* **52**, 161–72 (2013).
69. Scholz, N. *et al.* Complexin cooperates with Bruchpilot to tether synaptic vesicles to the active zone cytomatrix. *J. Cell Biol.* **218**, 1011–1026 (2019).
70. Chouhan, A. K., Zhang, J., Zinsmaier, K. E. & Macleod, G. T. Presynaptic mitochondria in functionally different motor neurons exhibit similar affinities for Ca2+ but exert little influence as Ca2+ buffers at nerve firing rates in situ. *J. Neurosci.* **30**, 1869–81 (2010).
71. Zhan, H., Bruckner, J., Zhang, Z. & O'Connor-Giles, K. Three-dimensional imaging of *Drosophila* motor synapses reveals ultrastructural organizational

patterns. *J. Neurogenet.* **30**, 237–246 (2016).

72. Bruckner, J. J. *et al.* Fife organizes synaptic vesicles and calcium channels for high-probability neurotransmitter release. *J. Cell Biol.* **216**, (2016).

73. Bekkers, J. M. Convolution of mini distributions for fitting evoked synaptic amplitude histograms. *J. Neurosci. Methods* **130**, 105–114 (2003).

74. Clements, J. D. Variance–mean analysis: a simple and reliable approach for investigating synaptic transmission and modulation. *J. Neurosci. Methods* **130**, 115–125 (2003).

75. Karunanithi, S. *et al.* Activity-dependent global downscaling of evoked neurotransmitter release across glutamatergic inputs in Drosophila. *J. Neurosci.* **40**, 8025–8041 (2020).

76. Schneggenburger, R. & Neher, E. Presynaptic calcium and control of vesicle fusion. *Curr. Opin. Neurobiol.* **15**, 266–274 (2005).

77. Rebola, N. *et al.* Distinct Nanoscale Calcium Channel and Synaptic Vesicle Topographies Contribute to the Diversity of Synaptic Function. *Neuron* **104**, 693–710 (2019).

78. Atasoy, D. *et al.* Spontaneous and evoked glutamate release activates two populations of NMDA receptors with limited overlap. *J. Neurosci.* **28**, 10151–10166 (2008).

79. Giraudo, C. G., Eng, W. S., Melia, T. J. & Rothman, J. E. A clamping mechanism involved in SNARE-dependent exocytosis. *Science* **313**, 676–680 (2006).

80. Schaub, J. R., Lu, X., Doneske, B., Shin, Y. K. & McNew, J. A. Hemifusion arrest by complexin is relieved by Ca2+-synaptotagmin I. *Nat. Struct. Mol. Biol.* **13**, 748–750 (2006).

81. Tang, J. *et al.* A Complexin/Synaptotagmin 1 Switch Controls Fast Synaptic Vesicle Exocytosis. *Cell* **126**, 1175–1187 (2006).

82. Xue, M. *et al.* Tilting the Balance between Facilitatory and Inhibitory Functions of Mammalian and Drosophila Complexins Orchestrates Synaptic Vesicle Exocytosis. *Neuron* **64**, 367–380 (2009).

83. Cho, R. W. *et al.* Phosphorylation of Complexin by PKA Regulates Activity-Dependent Spontaneous Neurotransmitter Release and Structural Synaptic Plasticity. *Neuron* **88**, 749–761 (2015).

84. Jorquera, R. A., Huntwork-Rodriguez, S., Akbergenova, Y., Cho, R. W. & Littleton, J. T. Complexin controls spontaneous and evoked neurotransmitter release by regulating the timing and properties of synaptotagmin activity. *J. Neurosci.* **32**, 18234–45 (2012).

85. Vasin, A., Volfson, D., Littleton, J. T. & Bykhovskaia, M. Interaction of the Complexin Accessory Helix with Synaptobrevin Regulates Spontaneous Fusion. *Biophys. J.* **111**, 1954–1964 (2016).

86. Aberle, H. *et al.* wishful thinking encodes a BMP type II receptor that regulates synaptic growth in Drosophila. *Neuron* **33**, 545–58 (2002).

87. Guizar-Sicairos, M., Thurman, S. T. & Fienup, J. R. Efficient subpixel image registration algorithms. *Opt. Lett.* **33**, 156–158 (2008).

88. Vercauteren, T., Pennec, X., Perchant, A. & Ayache, N. Diffeomorphic demons : Efficient non-parametric image registration. *Neuroimage* **45**, S61–S72 (2009).

89. Schermelleh, L. *et al.* Super-resolution microscopy demystified. *Nature Cell Biology* **21**, 72–84 (2019).

90. Preibisch, S., Saalfeld, S. & Tomancak, P. Globally optimal stitching of tiled 3D microscopic image acquisitions. *Bioinformatics* **25**, 1463–1465 (2009).

91. Wojcik, M., Hauser, M., Li, W., Moon, S. & Xu, K. Graphene-enabled electron microscopy and correlated super-resolution microscopy of wet cells. *Nat. Commun.* **6**, 2–7 (2015).

92. Gorur, A. *et al.* COPII-coated membranes function as transport carriers of intracellular procollagen I. *J. Cell Biol.* **216**, 1745–1759 (2017).

93. Goshtasby, A. Image registration by local approximation methods. *Image Vis. Comput.* **6**, 255–261 (1988).

CHAPTER 3: Input- and synapse-specific neuromodulatory regulation of glutamate release at the larval *Drosophila* Neuromuscular Junction

Dariya Bakshinska[1], Caroline Cypranowska[2,5], Zachary L. Newman[2] and Ehud Y. Isacoff[1,2,3,4]

[1] Helen Wills Neuroscience Institute, University of California Berkeley, Berkeley, California 94720
[2] Department of Molecular and Cell Biology, University of California Berkeley, Berkeley, California 94720
[3] Weill Neurohub, University of California Berkeley, Berkeley, California 94720
[4] Molecular Biophysics and Integrated BioImaging Division, Lawrence Berkeley National Laboratory, Berkeley, California 94720
[5] Current Address: The Francis Crick Institute, London, United Kingdom

This manuscript is in preparation for submission.

Author contributions: Dariya Bakshinska performed all of the experiments and analysis, except for the RNAseq (Fig. 3.3A,B), which was done by Caroline Cypranowska. Zach Newman created the QuaSOR to molecular imaging mapping system used throughout.

Abstract

Norepinephrine in vertebrates and its invertebrate analog octopamine (OA) regulate diverse neural circuits and behaviors by modulating neuronal excitability and synaptic transmission. We studied the regulation of excitatory synaptic transmission in *Drosophila* larval type I motor neurons (MNs) by OA, which is released by type II MNs. Quantal-resolution optical imaging showed that octopamine increases glutamate release in a manner that depends on phospholipase C (PLC) and Unc13A — a known target of modulation by the PLC product diacylglycerol (DAG). The potentiating effect of octopamine was mimicked by the membrane-permeable DAG analog PdBU and the amount of potentiation was proportional to the level of Unc13A at the synapse. Strikingly, modulation occurred only at synapses of type Ib MNs, and not type Is MNs. While, overall, OA potentiated release, a subset of Ib synapses depressed. The fraction of synapses that depressed was larger in octopamine than in PdBU–treated animals. Also knocking down Unc13A increased the number of synapses that depressed after treatment even further. Taken together, this suggests that octopamine also acts through a non–G_q coupled OA receptor in addition to the G_q-coupled receptor (which acts through the PLC pathway). Consistent with this, RNAseq analysis showed that type I MNs express both G_q and non-G_q coupled octopamine receptors. Our observations suggest that octopamine released by type II MNs boosts and diversifies glutamate release from one of two convergent glutamatergic inputs in a way that can increase both the strength and dynamic range for locomotory drive.

Introduction

Catecholamines, such as norepinephrine and dopamine, are essential neuromodulators that regulate neuronal excitability and synaptic transmission thereby controlling neural circuit function, brain states and behavior[1,2]. In vertebrates, the actions of these neuromodulators are widespread because of the broad projections by norepinephrine axons (from *locus coeruleus*) and dopamine axons (from basal ganglia) to many targets within the brain[1]. A similarly broad projection pattern is seen in the insect brain both for dopamine axons[3] and for axons that release the norepinephrine analog octopamine (OA)[4].

In *Drosophila*, OA has been shown to play a role in locomotion[5], courtship behavior[6], sleep[7], olfactory[8] and aversive[9] learning, and many other behaviors[10] analogous to the functions of norepinephrine in the vertebrate brain. For each of these behaviors, the modulation can occur at multiple sites in the relevant neural circuit. In locomotion, this includes not only sites in the brain and ventral nerve cord, but also at the neuromuscular junctions of the body wall muscles that mediate movement. The cellular mechanisms of OA modulation in the central nervous system are difficult to study. We therefore turned to the excitatory synapse model of the *Drosophila* larval neuromuscular junction (NMJ). In the NMJ, type I motor neurons (MNs) release glutamate and provide the drive for muscle contraction[11]. OA boosts this transmission both pre- and postsynaptically[12]. Presynaptically, OA has two effects — a long-term developmental effect and an acute effect. Long-term changes in axon growth are induced by OA through activation of the cyclic AMP (cAMP)/CREB pathway in type I MNs[13,14]. Acutely, OA increased evoked glutamatergic transmission, but the site of this modulation (presynaptic *versus* postsynaptic) and signaling mechanism are not known[14]. We applied quantal-resolution optical imaging, as described in the previous chapters, to study the presynaptic aspects of OA modulation with high precision.

In general, neuromodulators (such as OA) can act both locally — near the site of release with low affinity receptors — and at a distance through high affinity receptors. At the *Drosophila* NMJ, type I MNs, which release glutamate and provide the drive for muscle contraction, form synapses near two other neuron types: type II MNs, which release glutamate and OA, and type III MNs, which release neuromodulatory peptides [11]. Firing in all three MN types contributes to an increases in locomotion[11]. The small molecule transmitters glutamate and OA are released from small clear vesicles at all frequencies of action potential firing, but peptide release only occurs at high firing frequencies[15]. The neuromodulatory action of all of these transmitters increases as firing frequency increases due to the accumulated activation of their G protein coupled receptors [16].

Here, we find that OA acutely increases glutamate release from type I MNs and that this modulation depends on phospholipase C (PLC) and uncoordinated (Unc)13A, a known target of modulation by the PLC enzymatic product diacylglycerol (DAG). Consistent with this, the effect of OA is mimicked by the membrane-permeable DAG analog PdBU. Strikingly, the modulation occurs only at the synapses of type Ib MNs and not in the type Is MNs that innervate the same muscle. Moreover, the effect varies across type Ib synapses — with most synapses potentiating and some depressing. The level potentiation and depression varied greatly between synapses. Among potentiating synapses, the degree of potentiation was proportional to the level of Unc13A at the synapse. Overall, modulation by OA and PdBU increases the probability of action potential evoked glutamate release in Ib synapses. This diversity of modulation aids in maintaining a dynamic range of the system.

Results

Octopamine boosts glutamate release from Ib but not Is MNs

In the *Drosophila* larval neuromuscular junction (NMJ), almost all of the muscle cells receive input from two excitatory glutamatergic type I MNs: Ib (big) and Is (small)[17], each forming multiple boutons on the muscle, with each bouton containing multiple synapses (**Fig. 3.1A**). In addition to the type I MNs, muscle cells also receive inputs from type II neuromodulatory neurons, which release octopamine (OA)[18], and type III MNs, which release neuropeptides[15]. Type I and II axons have been shown to be intricately linked spatially[18] — with type II terminals synapsing close to type I terminals — and functionally[14]. Specifically, previous work has shown that prolonged optogenetic activation of type II MNs leads to OA-dependent growth of arbors in type I MNs, synaptic outgrowth of type II MNs, and an increase in locomotion[14]. In addition, acute application of OA (10 μM) has been shown to increase excitatory junction potentials (EJPs) in the muscle[14]. However, it was not clear whether this effect was due to pre- or postsynaptic action since OA receptors are found on both sides of the synapse[5,14].

Using spinning disk confocal microscopy, we imaged postsynaptic Ca^{2+} influx through iGluRII ionotropic glutamate receptors using SynapGCaMP6f. As in our previous work, in SynapGCaMP6f the Ca^{2+}-indicator portion (GCaMP6f), is targeted to the plasma membrane and the post-synaptic density via tethering to the single pass transmembrane protein CD8 (at its N-terminal) and via tethering to Discs large protein (at its C-terminal), respectively[19]. SynapGCaMP6f was expressed exclusively in the muscles under control of the myosin heavy chain (MHC) promoter (*MHC-SynapGCaMP6f*). To assess basal release, we measured action potential (AP)-evoked release during low frequency (0.2 Hz) stimulation at Ib/Is MN pairs that innervated the same muscle cell, specifically muscle 4. We obtained a baseline recording of 100 stimuli in control physiological solution, stopped stimulation, incubated with 10 μM OA for 10 min and then resumed stimulation for 100 more stimuli at 0.2 Hz in the continued presence of OA. First, we measured the number of events per trial, as measured by the number of $\Delta F/F$ peaks time-locked to our stimulus, across the entire NMJ (see Methods). OA increased the total number of transmission events per stimulus in the Ib MN (**Figs. 3.1B, Suppl. Fig. 3.1)** but had no effect on the Is MN (**Fig. 3.1C, Suppl. Fig. 3.1)**. To compare results between NMJs, we normalized the transmission event counts to the NMJ area to yield a measure of quantal density (QD). In Ib MNs, OA increased QD by ~40% (mean pre-OA QD = $0.018 \pm 1.4\times10^{-3}$ events/μm^2, mean post-OA QD = $0.025 \pm 2.2\times10^{-3}$ events/μm^2, $p = 0.03$) (**Fig. 3.1G**). In contrast, type Is MNs, which had an ~3-fold higher basal QD than the type Ib MN, as shown previously [19,20], showed no significant change in QD in response to OA (mean pre-OA QD = 0.053 events/μm^2, mean post-OA QD = 0.054 events/μm^2) (**Fig. 3.1H**). These observations show that OA boosts release from Ib but not Is MNs.

Octopamine differentially modulates P_r at Ib synapses

Ib MN synapses show a great diversity in basal presynaptic strength—that is the probability of action potential evoked release (P_r). We wondered if only some synapses are specialized for OA modulation or if this regulation is broad. To measure synaptic transmission at a large number of individual synapses simultaneously, we used our method of Quantal Synaptic Optical Reconstruction (QuaSOR)[20] to augment the spatial resolution with which we identify the site of transmission events by using 2-D Gaussian fitting algorithm to fit each $\Delta F/F$ event (**Figs. 2.1, 3.E,F and Suppl. Fig 3.2C,D**). The map of transmission events was aligned to a map of presynaptic active zone (AZ) locations that was obtained by subsequent antibody staining and 3D Airyscan imaging of the AZ scaffolding protein Bruchpilot (Brp) (**Figs. 3.1D and Suppl. Fig. 3.2A, B**). This function-structure alignment provided a measure of transmission at each AZ [20]. In general, after the addition of OA, the number of transmission events increases per AZ as indicated by the size of the clusters when comparing pre-OA and post-OA functional maps (**Fig. 3.1E vs. Fig. 3.1F**).

Previously, we showed that basal P_r varies widely (0.01–0.62), i.e. by >50-fold (>5,000%), across synapses of a single Ib axon[19–22]. We confirmed this diversity here (**Fig. 3.2A,B,D,E**). We found that synapses with a similar basal P_r, varied widely in response to OA (**Fig. 3.2A-E**). For example, three neighboring AZs with similar Brp content (**Fig. 3.2A)** and similar basal P_r (AZ #148: 0.02, AZ #150: 0.01, AZ #153: 0.02) (**Fig. 3.2B, D**) responded to OA with varying degrees of potentiation of P_r (AZ # 148: 0.02 → 0.04, AZ #150: 0.01→ 0.06, AZ #153: 0.02 → 0.17) (**Fig. 3.2C,D**). The differential effect on neighboring synapses suggests that the determinants of response to OA are functioning locally at individual synapses. Across 519 AZs from 4 Ib NMJs (**Fig. 3.2E**), P_r increased in 76% of the AZs and decreased in 23%, with 1% remaining unchanged.

As shown earlier [20,22,23], we found that the more Brp that is present at a synapse, the higher its basal P_r (**Fig. 3.2F, open circles, and Suppl. Fig. 3.3 A,C**). The entire relationship was shifted to higher P_r values after OA application (**Fig 3.2F, closed circles, and Suppl. Fig. 3.3 B, D**). While Brp explains some of the diversity in P_r that we observe pre and post-OA, we next wondered what were some other proteins that are implicated in modulation by OA.

Modulation by octopamine depends on phospholipase C

Octopamine is the *Drosophila* analog of norepinephrine and ORs are similar to adrenergic receptors[24]. ORs can be divided into two families: α-like (oamb and Octα2R) and β-like adrenergic receptors(Octβ1R, Octβ2R and Octβ3R). Octα2R is the newly discovered OR and activates the G_i pathway, thereby inhibiting neurotransmitter release[25]. Octβ2R has been shown to promote long-term type I and type II outgrowth of boutons through the G_s-coupled cyclic-AMP(cAMP) pathway, thereby chronically increasing synaptic release[14]. Octβ3R also increased cAMP levels when activated[26]. Octβ1R on the other hand is thought to be a brake on Octβ2R function[5]. The other main receptor, oamb, has been shown to be homologous to α1-like adrenergic receptors, which act through the G_q-coupled pathway[8].

The observation that OA increases P_r points to a presynaptic mechanism. This led us to ask which OA receptors are expressed in type I MNs. To answer this, we expressed nuclear-targeted mCherry in all type I MNs (*OK6>Gal4;UAS>NLS-mCherry*), isolated VNCs from 3rd instar larvae, dissociated the cells, FACS sorted the fluorescent cells and isolated pooled RNA for bulk RNAseq analysis (**Fig 3.3A**). We found that all five OA receptors (ORs) are expressed in the type I MNs (**Fig. 3.3B**).

The rapid time-course (minutes) of the modulatory effect of OA led us to consider the G_q pathway, which activates phospholipase C (PLC), which cleaves phosphatidylinositol 4,5-bisphosphate (PIP_2) into inositol trisphosphate (IP_3)—to release Ca^{2+} from intracellular stores—and diacylglycerol (DAG), both of which promote transmitter release[27,28]. We tested the possible involvement of this pathway by blocking PLC. Stimulating at 0.2 Hz, we imaged responses to 50 baseline stimuli, applied the PLC-selective inhibitor U73122 at 2 μM for 10 min, stimulated again for at least 100 trials with just the PLC inhibitor and then applied 10 μM OA for 10 min after which we again stimulated for at least 100 trials. U73122 prevented the OA-induced increase of events per trial (basal mean = $0.016 \pm 6.7\times10^{-4}$ events/μm^2, +PLC Inhibitor mean = $0.015 \pm 1.9\times10^{-3}$ events/μm^2, +PLC Inhibitor / + OA mean = $0.013 \pm 1.6\times10^{-3}$ events/μm^2) (**Fig. 3.3C**) and the increase in quantal density (**Fig. 3.3D**). This observation suggests that the the G_q-mediated pathway is involved in modulation of release by OA. We therefore next turned to test whether DAG is the possible mediator of PLC regulation.

The membrane-permeable DAG analog PdBU mimics OA

We tested a DAG analog, phorbol-12,13-dibutyrate (PdBU), which has been shown to increase the size of excitatory postsynaptic currents (EPSCs) as well as the frequency of spontaneous release at the *Drosophila* larval NMJ indicating a presynaptic mechanism [29]. Following baseline imaging of basal AP-evoked transmission for 100 stimuli at 0.2 Hz, we applied PdBU (1 μM) for 6 min and then imaged evoked transmission for an additional 100 stimuli at 0.2 Hz in the continued presence of PdBU. As seen with OA above, PdBU increased the number of events per trial in type Ib MNs (**Fig. 3.4A**). This boost represented an increase of ~60% in Ib quantal density (mean pre-PdBU QD = $0.028 \pm 3.7\times10^{-3}$ events/μm^2, mean post-PdBU QD = $0.044 \pm 5.1\times10^{-3}$ events/μm^2, n = 15 NMJs; $p = 0.02$, paired student's t test) (**Fig. 3.4G)**.

Similar to OA-treated animals, Ib synapses varied widely in basal P_r (0.04–0.59) (**Fig. 3.4B,C,F**). PdBU boosted evoked release at synapses across the range of basal P_r, (**Fig**. **3.4B-F**), including at synapses with a very high basal P_r (**Fig. 3.4B-D,F**: AZ #131 basal P_r 0.52 → 0.64, AZ #144 basal P_r 0.59→0.93). Out of the 588 AZs in five type Ib NMJs, 90.3% (n = 531 AZs) increased P_r and 9.7% (n = 57 AZs) decreased P_r (**Fig. 3.4E)**. The average PdBU-induced increase in P_r across the synapse population was 57 % and the difference between cumulative distributions before and after PdBU was equally significant ($p = 3.7\times10^{-16}$, two-sample Kolmogorov-Smirnov test) (**Suppl. Fig. 6A**). These observations show that the large majority of Ib synapses, across a wide range of basal presynaptic strength, are potentiated by a DAG analog. Strikingly, the degree of potentiation also varied greatly between Ib synapses (**Fig. 3.4E**).

Potentiation by PdBU and OA depends on Unc13A

One of the mechanisms through which DAG modulates transmitter release is by binding to the presynaptic protein Unc13[28] (**Fig. 3.5A**), which is involved in the priming and localization of synaptic vesicles [30]. To investigate the possible role of Unc13, we knocked it down with RNAi selectively in type I MNs ($OK6>Gal4;UAS\text{-}Unc13^{RNAi}$). Consistent with earlier work[31], knockdown of Unc13 greatly reduced the basal number of transmission events (4.9 ± 0.19 events/trial for *unc13-RNAi* (**Fig 3.5B)** vs. 26.8 ± 0.47 events/trial for in *wt* (**Fig 3.4A**)). In the Unc13 knockdown, PdBU had a reduced effect on the number of transmission events/stimulus (**Fig. 3.5B**).

Drosophila has two splice isoforms of Unc13: Unc13A and Unc13B, which differ in size and effect on transmitter release, and localize at different distances from the core of the AZ [31,32]. To determine the contribution of these Unc13 isoforms to modulation by DAG, we knocked them down individually in type I MNs. Knockdown of Unc13A (**Suppl. Fig. 3.4C**) severely impaired basal evoked release, reducing mean P_r by ~80% (*wt*: basal mean $P_r = 0.1 \pm 4.2 \times 10^{-3}$, n = 1145 AZs from 9 type Ib NMJs vs *unc13A-RNAi*: basal mean $P_r = 0.02 \pm 1.2 \times 10^{-3}$, n = 566 AZs from 4 type Ib NMJs; $p = 9 \times 10^{-53}$, two-sample Kolmogorov-Smirnov test) (**Suppl. Fig. 3.4A,C,D**). In contrast, knockdown of Unc13B *augmented* basal evoked release, increasing mean P_r by ~80% (*wt*: basal mean $P_r = 0.1 \pm 4.2 \times 10^{-3}$, n = 1145 AZs from 9 type Ib NMJs vs *unc13B-RNAi* : basal mean $P_r = 0.18 \pm 9.7 \times 10^{-3}$ n = 492 AZs from 4 type Ib NMJs; $p = 3.78 \times 10^{-16}$, two-sample Kolmogorov-Smirnov test) (**Suppl. Fig. 2.4A,B,D**). Interestingly, knockdown of Unc13B increased the levels of Unc13A at Ib synapses by ~40% (**Suppl. Fig. 3.5B, E**), suggesting that Unc13B influences basal P_r, through a compensatory increase in Unc13A. The average level of Brp across Ib synapses was unchanged by knockdown of either Uc13A or Unc13B (**Suppl. Fig. 3.5D**).

We next asked how each Unc13 isoform contributes to the potentiation of transmitter release by PdBU and OA. In the Unc13A knockdown, PdBU induced an increase of 25% in quantal density (mean pre-PdBU QD = $0.006 \pm 9.6 \times 10^{-4}$, mean post-PdBU QD = $0.0075 \pm 8.9 \times 10^{-4}$) (**Fig. 3.5C**) and P_r of about 20%. Distributions of P_r were also significantly different pre- and post-PdBU (n=344 AZs from 3 NMJs; $p = 1.2 \times 10^{-19}$ by two-sample Kolmogorov-Smirnov test) (**Suppl. Fig. 3.6B**). In the Unc13B knockdown, PdBU induced an increase in quantal density of ~70% (**Fig. 3.5D)** and an increase in average P_r of 88% (n=393 AZs from 3 NMJs; $p = 3.5 \times 10^{-16}$) (**Suppl. Fig. 3.6C**). When comparing all the distributions of change in P_r (post-PdBU P_r – pre-PdBU P_r) across the three genotypes, Unc13A knockdown animals changed the least and Unc13B animals changed the most compared to *wt* (all comparisons statistically significant by a two-sample Kolmogorov-Smirnov test) (**Suppl. Fig. 3.6D**). Thus, compared to *wt* (PdBU potentiation = 57%), the knockdown of Unc13A decreased and the knockdown of Unc13B increased potentiation, suggesting that the level of Unc13A at a synapse determines its degree of PdBU potentiation. Indeed, in *wt* animals, the PdBU-induced increase in P_r was proportional to the quantity of Unc13A (normalized within an NMJ) in the synapse (**Fig. 3.6A**). Moreover, when combined together, these relations formed a continuum of potentiation levels between the low Unc13A levels of the Unc13A knockdown, the middle range seen in *wt*, and the elevated Unc13A levels in Unc13B knockdown animals (**Suppl. Fig. 3.7A,B).**

Similarly to our observations with PdBU, when investigating how each Unc13 isoform contributed to potentiation of transmitter release by OA, OA had little effect (~ 20 %) on Ib MN transmitter release in the Unc13A knockdown (mean pre-OA = 6.3 ± 0.35 events/trial, mean post-OA = 7.7 ± 0.36 events/trial) (**Fig. 3.6C**) but induced a larger potentiation (41%) in the Unc13B knockdown (mean pre-OA = 38.8 ± 0.8 events/trial, mean post-OA = 54.8 ± 0.9 events/trial) (**Fig. 3.6D**). As with PdBU, the OA-induced increase in P_r was proportional to the quantity of Unc13A in the synapse (**Fig. 3.6B**) although the change in P_r was lower overall given that PdBU acts on Unc13A directly. Together, our observations suggest that OA potentiation is mediated by the activation of a G_q-coupled OA receptor on presynaptic Ib MN nerve terminals, which activates PLC to produce DAG, which binds Unc13A and boosts action potential evoked glutamate release (**Fig. 3.7**).

Discussion

Catecholamines regulate the function of neural circuits by modulating neuronal excitability and synaptic transmission. The neuromodulatory actions vary depending on action at multiple receptors for each modulator and on the pre- and postsynaptic localization of the receptors. Typically, synapses between one class of presynaptic cells and one class of postsynaptic cells are expected to be similar and to be modulated in a similar manner. However, recent analyses on large populations of individual synapses have shown that even synapses made by one presynaptic neuron onto a single postsynaptic target can vary by orders of magnitude in basal presynaptic strength. We find here that there is also a large diversity in presynaptic modulation by the neuromodulator OA among the glutamatergic synapses of the model excitatory synapse of the *Drosophila* larval NMJ.

To understand how neuromodulation affects individual synapses, it is important to be able to investigate synaptic transmission at single synapse resolution at a large number of identified synapses simultaneously. As described in Chapter 2, we employed QuaSOR for optical detection of quantal synaptic transmission to resolve transmission events to individual synapses, which we identify by *post-hoc* super-resolution imaging of the molecular components of the presynaptic AZ transmitter release site[20]. We investigated the effects of OA modulation on the two type I MNs that synapse onto the common m4 muscle fiber, the Ib MN4 and the dorsal Is MN. We confirmed our earlier observations, and those of others, that basal P_r varies greatly between synapses of the same Ib MN and that basal P_r is ~3-fold higher at Is MN synapses than it is at Ib MN synapses (**Chapter 2**)[19,21,22].

Acute application of OA had been shown earlier to boost synaptic transmission, but it was not known if this action occurs pre- or postsynaptically[14]. We showed that OA boosts P_r, indicating a presynaptic site of potentiation. RNAseq analysis on type I MNs revealed that all five of the *Drosophila* OA receptors are expressed, consistent with presynaptic modulation. Strikingly, we found the OA boost in P_r occurs only in Ib MNs and not in Is MNs. Our RNAseq did not distinguish between type Ib and Is MNs, and there are no antibodies for the different OA receptors, so we cannot say if the absence of modulation of type Is synapses reflects missing receptor(s).

It is worth noting that type Is synapses differ in several other respects from type Ib synapses. Aside from their ~3-fold higher P_r, described above, Is MN synapses lack several regulatory properties that Ib MNs possess, including presynaptic homeostatic plasticity[19], and, as recently discovered in unpublished work from our laboratory, firing homeostasis (Hoagland et al., in preparation) and presynaptic metabotropic modulation by glutamate (Aghi et al., in preparation).

OA presynaptic potentiation depends on DAG modulation of Unc13A

Confirming earlier work[31] (and Chapter 2), we observed that basal P_r in type Ib MN synapses depends on the quantity of two key proteins of the AZ, the scaffolding protein Brp and the synaptic vesicle priming protein Unc13, specifically on the Unc13A isoform. Importantly, we found that the degree of potentiation of P_r by OA depends on the quantity of Unc13A at the synapse. Generally, Unc13 is involved in the priming and localization of synaptic vesicles [30]. DAG is thought to displace a water molecule at the C1-binding site in Unc13 and thus to bring synaptic vesicles closer to the plasma membrane a process that 'superprimes' them by lowering the energy barrier for synaptic fusion. [33,34] We asked whether this molecular pathway is involved in OA potentiation of type Ib synapses. We found that OA potentiation is mimicked by the membrane permeable DAG analog PdBU and that the actions of both OA and PdBU depend on both PLC and Unc13A.

Our results implicate the G_q coupled pathway in the rapid presynaptic modulation by OA and, by extension, *oamb*, the one OA receptor subtype that is G_q coupled. This rapid system of presynaptic modulation of release complements a slower OA modulated G_s system that regulates outgrowth of both type Ib and type II synaptic boutons[14].

While the average level of Unc13A and, to a lesser extent, Brp, correlated with the amount of potentiation, these two AZ proteins could not account for much of the variance, indicating that other proteins are also involved. Further studies are needed to identify the other determinants and to understand what makes them operate exclusively in Ib synapses. In other words, what is the missing factor(s) in Is synapses that prevents them from being susceptible to metabotropic modulation by glutamate, and homeostatic synaptic and firing plasticity. Together, these differences suggest that the Ib input is designed for plasticity and the Is input for constancy.

Materials and Methods

Drosophila husbandry and genetics

Several flies were obtained from the Bloomington Drosophila Stock Center (BDSC) including; Unc13^{RNAi} (pVALIUM20 vector; inserted into attP2; BDSC line 29312), SynapGCaMP6f (3rd chromosome MHC-CD8-GCaMP6f-Sh) lines were reported previously [19–21], Unc13A^{RNAi} and Unc13B^{RNAi} were also reported on previously[31] and were obtained from the Sigrist lab**.** Flies were raised on standard corn meal and molasses media at 25° C except for Unc13A^{RNAi} and Unc13B^{RNAi} flies which were raised at 27° C. A mix of male and female wandering third instar larvae were used in all experiments and only actively crawling larvae were picked for experiments. When necessary, third instar larvae were screened for balancers. The balancers with larval markers included CyO^{GFP} (3xP3-EGFP variant) and Tm6B. All larvae contained a single copy of SynapGCaMP6f on the third chromosome. The following genotypes were used: *wt* (w^{1118}; +/+; SynapGCaMP6f/+), Unc13A^{RNAi}(w^{1118}; OK6-Gal4/UAS-Unc13A^{RNAi}; SynapGCaMP6f/+), Unc13B^{RNAi}(w^{1118};OK6-Gal4/UAS-Unc13B^{RNAi}; SynapGCaMP6f/+).

Pharmacology

Drugs were diluted according to manufacturer's instructions and stored at -20ºC in small, 20 μL aliquots. Dilutions were made the day of the experiment by thawing the aliquot and diluting it in high-Ca^{2+} HL3. For experiments involving acute application of pharmacological agents the following drugs were used at stated final concentrations (Octopamine 2mM stock diluted into 10μM final concentration; PdBU 2mM stock diluted into 1μM final concentration and PLC inhibitor (U73112) 2mM stock diluted into 2 μM final concentration. Each aliquot only underwent the freeze-thaw cycle once.

SynapGCaMP6f functional imaging

Optical quantal imaging was performed similarly to our previous reports[19,20]. To summarize, third instar larvae were dissected on PDMS (Sylgard 184, Dow Corning, Auburn, MI) pads in ice-cold HL3 solution containing, in mM: 70 NaCl, 5 KCl, 0.45 $CaCl_2 \bullet 2H_2O$, 20 $MgCl_2 \bullet 6H_2O$, 10 $NaHCO_3$, 5 trehalose, 115 sucrose, 5 HEPES, and with pH adjusted to 7.2. Following removal of the brain (VNC), larval fillets were washed and imaged in room temperature HL3 containing 1.5mM Ca^{2+} and 25mM Mg^{2+}. Fluorescence images were acquired at room temperature with a Vivo Spinning Disk Confocal microscope (3i Intelligent Imaging Innovations, Denver, CO), using a 63 × 1.0NA water immersion objective (Zeiss), 1.2X optical adapter, LaserStack 488 nm (50 mW) laser, CSU-X1 A1 spinning disk (Yokogawa Tokyo, Japan), standard GFP filter, and EMCCD camera (Photometrics Evolve512, Tucson, AZ). All live SynapGCaMP6f imaging recordings were done on ventral longitudinal abdominal muscle 4 at segments A3-A5 of third instar larvae. All imaging was performed using 50 ms exposures (20 fps) of the full camera sensor (512 × 512 px).

Nerve stimulation was performed with a suction electrode attached to a Stimulus Isolation Unit (SIU, ISO-Flex, A.M.P.I. Jerusalem, Israel), with 100 us stimulus duration. The intensity of the stimulus was adjusted to recruit both Ib and Is axons (verified through imaging) and kept constant throughout the imaging session. Nerve stimulation and imaging were synchronized using custom-written Matlab scripts (Matlab Version 2015b, MathWorks, Inc., Natick, MA) in order to control the SIU and trigger imaging episodes with SlideBook (v6.0.16, 3i Intelligent Imaging Innovations).

The basal evoked transmission protocol was the following: at each NMJ we collected action potential (AP)-evoked responses during short episodes in which a single stimulus was delivered. The frequency of stimulation was 0.2 Hz. Each episode consisted of 10 frames (50 ms exposure) with 3-4 baseline frames prior to nerve stimulation around frame 5. There was a minimum of 100 episodes collected pre-drug exposure and a minimum of 100 episodes collected post-drug exposure. For the experiments where the PLC inhibitor was added (**Fig. 3.3C-D**) we first collected a 50 episodes to ensure a steady baseline, applied the PLC inhibitor and waited for 10 minutes before collecting another 100 episodes. Afterwards, we added OA, waited 10 minutes and collected at least another 100 episodes. Minor focusing adjustments were made between trials if deemed necessary.

For comparability between experiments, recordings were done on only one NMJ (Ib-Is pair) per larva and recordings were performed within 40 minutes from the start of the dissection, ensuring the animals health. As in our previous report[20], we alternated which segments (A3-A5) we imaged from since no significant difference was found between segments.

Functional registration and bleach correction

The initial quantal image analysis was performed using custom-written MATLAB protocols, same as in our previous work[20]. Individual stimulus episodes were excluded due to out of focus NMJs, moving NMJs or failed axon recruitment. Otherwise, all movies were filtered (Gaussian low-pass filter), to reduce high-frequency noise. Image analysis areas were then separated into Ib and Is NMJ regions. All imaging data were registered using a multi-stage approach, during which all images were registered to a common reference image (usually the first frame of the first image), even when multiple treatment protocols were acquired (pre- and post-drug).

Following area selection and reference image selection, NMJs were tracked relative to this reference image using a rigid subpixel registration method to remove any large movements within the NMJ imaging area[19,20,35]. As in our previous work[20], we corrected for local bouton movements using a custom diffeomorphic implementation of a demons algorirthm[36] Once motion corrected, movies were bleach corrected using a fit for a double exponential bleach correction curve to the mean baseline pre- and post-stimulus fluorescence data for each trial separately. Following bleach correction, both ΔF and ΔF/F movies were generated using the first image as the baseline fluorescence (F0) image for the episodic data.

Quantal event detection

To identify all quantal responses, we fit a single a single ΔF response template to the average temporal profile for all evoked responses at that NMJ. As in our previous report[20], each pixel's temporal response was analyzed independently to determine if it had a high degree of correlation with the template response, as determined by the degree of cross-covariance. These highly correlated pixels and frames were then flagged as active if they had ΔF/F amplitudes that were above a minimum threshold (typically between 0.04 and 0.05 ΔF/F) and at least 1.5–2 times larger than the standard deviation of the values at that pixel. We also maintained a minimum allowable time between subsequent events at each pixel (100 ms) to prevent over-fitting. Coactive pixels were then grouped together into a single response field. This produced a single, isolated, maximal temporal projection image of the response's spatial profile. To eliminate false positives, we applied size, shape, and amplitude thresholds to these response fields. Following detection processing, events were sorted into the appropriate category using the timing of the response relative to the stimulus timing. Only a 200 ms window, following each AP, was used to assign evoked responses.

Quantal synaptic optical reconstruction (QuaSOR)

After event detection, isolation, and verification, we then proceeded to analyze the 2D response profile of each event's maximum ΔF/F spatial profile using the custom QuaSOR algorithm as in our previous work[20]. Briefly, we first looked at all the identified responses from our quantal detection and isolated small ROIs containing individual or small groups of partially overlapping response fields that corresponded to individual or small groups of events. These smaller ROIs were then subjected to independent 2D Gaussian mixture model fitting of the isolated ΔF/F spatial profiles. Following 2D

Gaussian mixture model fitting for all response ROIs, all event functions were then remapped onto a common coordinate space and merged to define a single set of 2D Gaussian functions for each quantal response. The peak positions of each 2D Gaussian component were used to define event locations in a 21.2 nm x 21.2 nm pixel coordinate space. For visualization purposes, maps were generated by applying a normalized 2D Gaussian filter to each event coordinate prior to adding each event to the overall image. In this way each pixel contains an approximation of the event density at that location. To facilitate AZ matching we sometimes reoriented the QuaSOR data by rotating and translating all the coordinates prior to re-rendering the maps to match the structural Airyscan data.

QuaSOR quantification

Local QuaSOR synapse alignments were performed by identifying maximum evoked coordinate density positions for synaptic ROIs within a 350 nm radius. Maintaining their relative organization to nearby events, these QuaSOR event coordinates were averaged together with other synapses to generate a mean density image for synapse groupings. On its own, in absence of molecular imaging of AZ locations, synapse assignment in QuaSOR is not certain and could merge transmission events from neighboring synapses in regions of high synaptic density. We, therefore, focused our study on NMJs where QuaSOR maps were related to molecular structural imaging maps generated in Airy. Linear uniform global transformations in the x and y axes were applied to adjust for stretch of the tissue that occurred after the live optical quantal imaging during fixation and mounting on slides under cover glass for molecular imaging. The result yielded images in which QuaSOR transmission sites could be matched to Airy AZs. Single synapse AP-evoked transmission probability (P_r) was determined by dividing evoked event counts within the single AZ domain by the number of motor nerve stimuli either pre or post-drug (P_r = events per synapses/# of stimuli; ranging from 0 to 1).

Antibodies and immunohistochemistry

Larvae were fixed in room temperature Bouin's fixative (Ricca Chemical Company, Arlington, TX) for 5-6 min, permeabilized in PBS with 0.1% Triton X100 (PBT) and blocked in PBS with 0.1% Triton X100, 2.5% normal goat serum, and 0.02% sodium azide (PBN). All antibody incubations were performed in PBN and all washes were performed in PBT. Mouse anti-Brp (nc82; Developmental Studies Hybridoma Bank, Iowa City, IA) was used at 1:100 for Airyscan imaging. Chicken anti-GFP (Thermo Fisher A10262; Thermo Fisher Scientific Waltham, MA) was used at 1:1000 to label SynapGCaMP6f in fixed samples. Rabbit anti-Unc13a antibody (Sigrist lab) was used at 1:1000. Alexa Fluor 488 goat anti-chicken (Thermo Fisher A11039), Alexa Fluor 555 goat anti-rabbit (Thermo Fisher A32727), and Alexa Fluor 647 goat anti-mouse (Thermo Fisher A21235) secondary antibodies were all used at 1:1000. Antibodies obtained from the Developmental Studies Hybridoma Bank were developed under the auspices of the National Institute of Child Health and Human Development of the National Institutes of Health and maintained by the Department of Biological Sciences of the University of Iowa, Iowa City, IA. We confirmed the specificity of the Unc13A antibody by comparing staining in control animals and in *unc13A-RNAi* animals. To obtain uniformity in antibody staining, we fixed and stained the different genotypes compared within an experiment simultaneously with the same reagents.

Confocal and Airyscan imaging and analysis

Following antibody incubations and washes, larval fillets were mounted in Vectashield (H-1000; Vector Laboratories, Burlingame, CA) or Vectashield HardSet (H-1400). Airyscan imaging was performed on a Zeiss LSM 980 microscope. All samples were imaged with a 63X oil immersion objective (NA 1.4, DIC; Zeiss) using Zen software (Zeiss Zen black 2.3 SP1). All imaging data were collected using identical imaging and processing parameters for a given experiment set. Unless otherwise noted all Airyscan images are displayed as Gaussian filtered maximum intensity projections that were generated using custom-written MATLAB routines. Airyscan imaging data were acquired using a tiling strategy, whereby smaller volumes of each NMJ were acquired sequentially and stitched together. Brp reconstructions for matching to QuaSOR data were acquired on the LSM 880 system. Briefly, each imaging volume was acquired with an additional magnification of 12x with a 5 AU pinhole, 2 µs pixel dwell times, line averaging of 2, an x-y dimension of 1024 by 1024 px (processed to 1000 by 1000 px) at 11 nm/px, and axial z spacing of 159 nm. Each of the three-channel volumes (anti-GFP/Alexa 488, anti-Brp/Alexa 647, and anti-Unc13A/Alexa 555) were scanned sequentially.

Airyscan processing of all channels and z slices was performed in Zen (Zeiss Zen Black v2.3 SP1) using super-resolution settings. We then sequentially stitched each 4D volume together in Fiji (NIH ImageJ Version 2.0.0-rc-43/1.52n) using pairwise stitching with linear blending . Alignments were performed to maximum intensity pixels of Brp puncta in overlapping volumes. AZ locations in stitched Airyscan datasets were calculated by masking the volumetric Brp data. Sites were initially identified using a local 3D Brp intensity maxima with a minimum distance of 150 nm from neighboring maxima. AZ identifications were manually validated and corrected when neighboring sites were misidentified. AZ-specific Brp voxel intensities were calculated by identifying 3D-connected voxels to each AZ maxima for isolated AZs. To avoid artifacts of stitching and bleaching of overlapping regions, pixel quantifications were collected using the original image pixel intensity information, prior to stitching, with intensity values calculated from 3D voxel AZ masks.

Structure-function matching.

QuaSOR data were matched to the corresponding Airyscan data. First, the two datasets were roughly aligned by rotating either the QuaSOR or the Airyscan data to match the orientation of the corresponding map. Once roughly aligned, sites were matched to one another in a pairwise fashion taking care to match each Airyscan AZ to a corresponding location on the QuaSOR map. We used low density areas to match all unambiguous AZ pairs with clear relative orientations and positions. Following these areas, we used the relative positioning of AZs around these pairs to match the denser regions or match AZs with no corresponding QuaSOR activity to an empty region of the QuaSOR map. In the Airyscan matched data, we sorted all QuaSOR event coordinates to their nearest QuaSOR AZ centroid location. All pairs had to minimize the local alignment variance within each bouton as determined by the alignment vector between sites. The quality of the AZ matching was further confirmed by using the paired coordinate positions to generate vectors to transform the QuaSOR coordinates into the matching Airyscan pixel-space. This was done by first converting the relative QuaSOR coordinates into a matched pixel-space image and then using a 2D, locally weighted, mean transformation method, with groupings of 8–14 AZs being used as control points in the local weighting. Successful site pairing generated accurate remapping of QuaSOR events onto the appropriate AZ for either structural imaging technique. However, all quantifications were performed on un-translated data in order to eliminate artifacts of transformations.

RNA-Sequencing:

CNS dissection

Prior to dissection 3rd instar larva were screened for the presence of nuclear mCherry in the VNC with ZEISS Axio Zoom v16 FL epifluorescence microscope. For bulk RNA-sequencing experiments, larvae were rinsed twice in 1X PBS (Gibco), once in 70% ethanol, and again in 1X PBS to sterilize the surface of the animals. Larvae were dissected on a Sylgard pad in a droplet of Schneider's complete media (Gibco) supplemented with 10% FBS (Corning) and 1% PenStrep (Gibco). After removing extraneous tissues, the brain and VNC were transferred to a low-binding 1.5 mL tube containing Schneider's complete media on ice until dissociation. Dissected tissues were kept on ice prior to dissociation no longer than 60 minutes to ensure the viability of the cells during FACS sorting.

CNS dissociation

Tissue samples were washed three times with 500 µL Schneider's media containing 1.5 mM EDTA and 1.5 mM L-Cysteine to remove media containing FBS. Fresh dissociation solution was prepared for each experiment from Schneider's media with the following additives: 1.5 mM EDTA, 1.5 mM L-Cysteine, papain (Worthington), and 1.25 mg/mL collagenase type-I (MilliporeSigma). Tissue samples were transferred into the dissociation solution and incubated at 25°C on a nutator for 5 minutes. Samples were triturated 30 times with a P200 pipette tip. This process of incubation and trituration was repeated before a final step in which tissue was sheared 7 times with a 27G1/2 needle.

The digestion reaction was quenched with the addition of 500 µL Schneider's complete media with 10% FBS and 1% PenStrep. Dissociated cells were passed through a 40 µm cell strainer (Falcon) and transferred to a low-binding 1.5 mL tube. The processed sample was centrifuged at 0.7 x g for 7 minutes, after which the supernatant was replaced with 1 mL of Schneider's complete media containing 5% FBS and 1% PenStrep.

Fluorescence Activated Cell Sorting

Processed cell samples were stained with 0.3 µM Sytox Green (Molecular Probes) to assay cell viability prior to sorting. Cells were sorted on a BD Influx Cell Sorter with 140 µm tubing at pressures < 12 PSI. The sorted population was chosen for high expression of nuclear mCherry (PE-Texas Red) and low Sytox Green fluorescence (GFP). Plots of

FACS data were created using the flowCore (ver 1.52.1)[38] and ggcyto packages (ver 1.14.0)[39].

Low-input RNA-Seq Library Preparation and Sequencing

Cells were sorted into RLT lysis buffer (RNeasy Micro, QIAGEN) supplemented with 3.5 mM BME. Cells were lysed by vortexing for 30 seconds at room temperature. RNA extraction was performed according to RNEasy Micro kit protocol, omitting the DNase digestion step. Extracted RNA was checked for quality by an Agilent 2100 Expert Bioanalyzer with a Eukaryote Total RNA Pico chip.

RNA was annealed to an oligo-dT primer (5' AAGCAGTGGTATCAACGCAGAGTACT$_{30}$VN-3', IDT) in a buffer containing 2.5 mM dNTPs and recombinant RNase Inhibitor (Takara). First-strand synthesis was performed with the SuperScriptII kit using a custom template-switching oligo (5'-/5Me-isodC//iisodG//iMe-isodC/AAGCAGTGGTATCAACGCAGAGTACATrGrGrG-3', IDT) with 5' modifications to avoid the creation of concatemers in low input samples[40]. cDNA preamplification, lambda exonuclease (New England Biolabs) digestion, size-selection with AMPure XP beads (Agencourt) were performed as described previously[41]. Libraries were constructed from preamplified cDNA using the Nextera XT kit (Illumina) and size-selected with AMPure XP beads. Fragments above 700 bps were excluded with Pippin Prep (SAGE Biosciences). Indexed libraries were sequenced on Illumina Hi-Seq 4000 sequencers to produce 100 nt paired-end reads.

RNA-Seq Alignment and Pre-processing

Demultiplexed .fastq files were first analyzed with FastQC (ver 0.11.7)[42] to check for quality and trimmed with Trimmomatic (ver 0.38)[43]. Trimmed reads were aligned to a custom reference genome built from Berkeley Drosophila Genome Project (dm6, release 98) genome assembly and the pUAST-mCherry-NLS vector sequence for the detection of the mCherry mRNA reads. Samples bearing dsRNA constructs were mapped to custom genomes containing the aforementioned transgenes and the sequence of the dsRNA construct. Mapping was performed with HISAT2 (ver 2.1.0)[44] and the counts matrix was generated with the featureCounts function from the Subread package (ver 1.6.4)[45].

Gene Filtering, Normalization and Differential Expression Analysis

Biological analysis was performed in R after using a custom script to import the featureCounts output into a SummarizedExperiment object (ver 1.16.1)[46]. Genes with fewer than 5 counts across 2 libraries were considered undetectable and removed from downstream analysis. Libraries were normalized by calculating a size factors for each sample from the median ratio of gene expression relative to the geometric mean for each gene as implemented in DESeq2 (ver 1.26.0)[47]. Identification of differentially expressed (DE) genes between each knockdown condition was performed with the DESeq2. Visualization of DE analysis was performed with custom scripts built upon ggplot2 (ver 3.2.1)[48].

Statistics and reproducibility.

Student’s paired t-test was used to compare paired Ib QDs pre and post-drug. Two-sample two-sided Kolmogorov–Smirnov tests was used to compare pooled cumulative distributions. One-way ANOVAs NMJ Ib properties for distributions of data between multiple bins. Unless otherwise noted, reported values are mean ± SEM. Sigmoidal and exponential fits were done using custom MATLAB code using nonlinear optimization using a multi-start algorithm to obtain the best fit. The goodness of fit was assessed using the sum squared error of the residuals.

The specific statistical tests as well as the number of replicates including numbers of animals, NMJs or AZs are all provided in the corresponding figures and/or figure legends. For all figures, significance markers are *$p < 0.05$, **$p < 0.01$, ***$p < 0.001$, or n.s. not significant for the comparisons indicated in the figure or figure legend. Representative QuaSOR and Airyscan images presented in figures were all reproduced in multiple animals. To assess reproducibility, recordings were done on only one NMJ per larva (i.e. the number of NMJs = the number of larvae) in recordings that were performed within 40 min of the beginning of the dissection, thereby ensuring health and similar conditions.

Figures

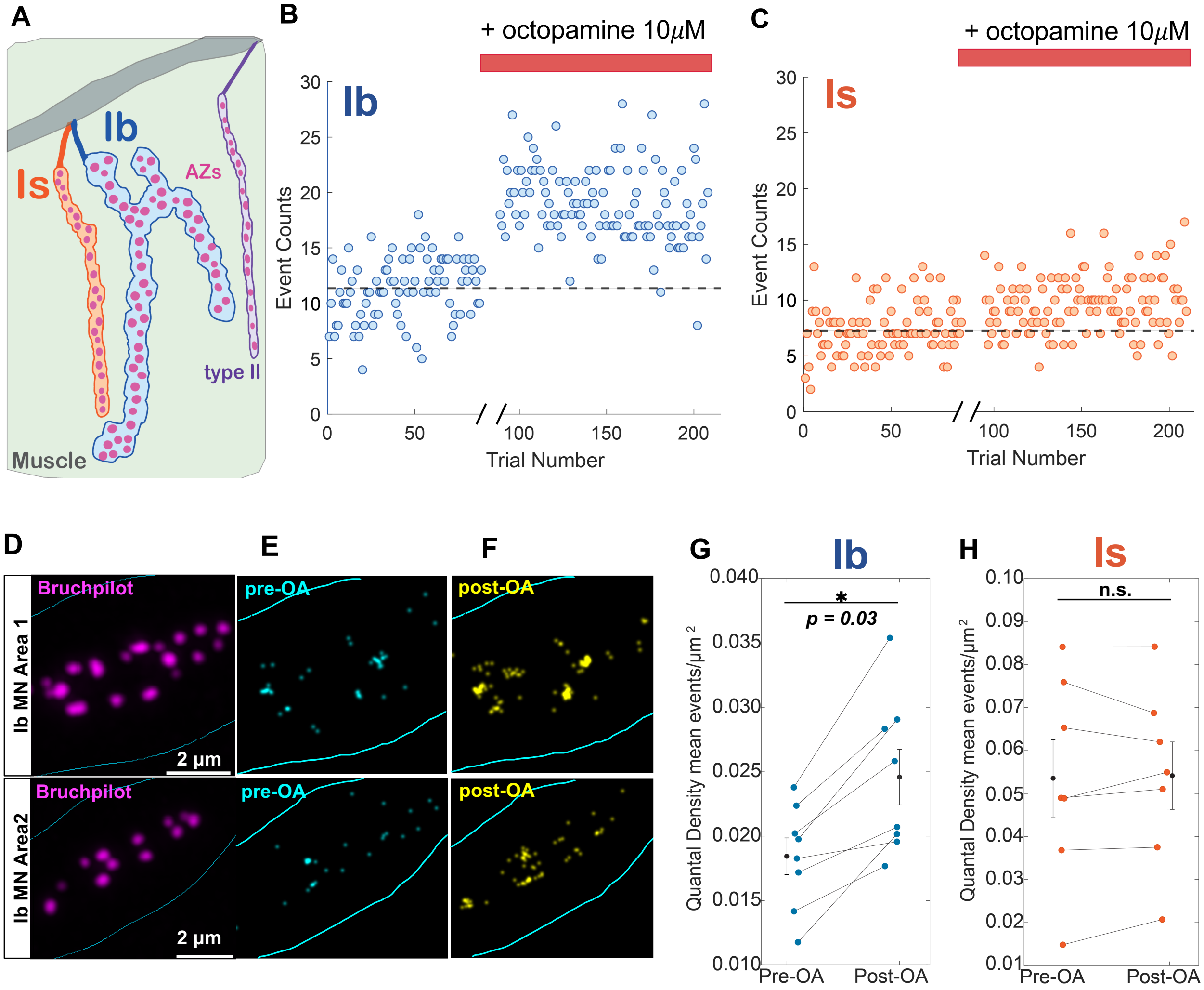

Figure 3.1. Effect of octopamine on type I MNs.

A) Schematic depicting the *Drosophila* NMJ illustrating type II MN (purple), type I MNs: Ib (blue) and Is MN (orange) synapsing onto the same muscle. Individual Active Zones (AZs) are shown in magenta.

B) Event counts per trial for an example Ib MN. Break in the axis shows addition of octopamine (OA: 10μM) followed by a 10min incubation period. Red bar is the incubation period + trials with OA. Dashed black line is the mean number of events per trial before OA.

C) Event counts per trial for the Is of the same NMJ as in (B). Break in the axis shows addition of octopamine (OA: 10μM) followed by a 10min incubation period. Red bar is the incubation period + trials with OA. Dashed black line is the mean number of events per trial before OA.

D) Two example Ib boutons (top and bottom) stained for the AZ scaffolding protein Bruchpilot (Brp) shown in magenta. Every magenta cluster is an individual AZ. Scale bar = 2 μm.

E) Same boutons as in (D) before the addition of OA during 0.2Hz evoked stimulation. Every cyan cluster has a corresponding AZ shown in (D).

F) Same boutons as in (D) and (E) after the addition of OA during 0.2Hz evoked stimulation.

G) Quantal densities (mean events per trial/ μm^2) for Ib MNs before and after OA (n = 8 *wt* NMJs).

H) Quantal densities (mean events per trial/ μm^2) for Is MNs before and after OA (n = 7 of the 8 *wt* NMJs from (G)).

Error bars on the sides are mean ± SEM. (n.s., not significant by Student's paired t-test). Blue line in (D)–(F) is the Ib MN boundary

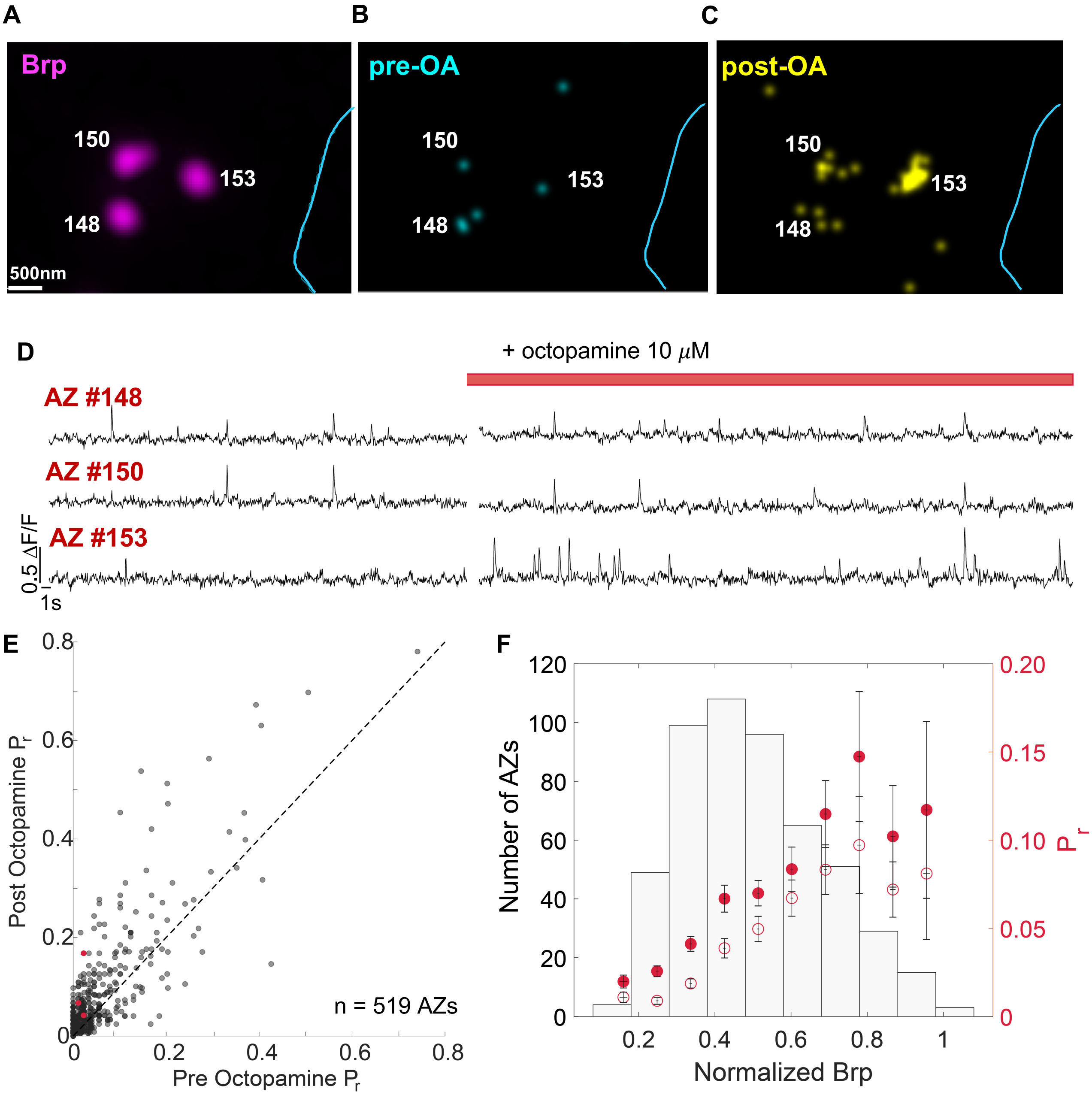

Figure 3.2. Acute application of octopamine (OA) increases the P_r of most synapses in Ib MNs but modulates each synapse differently.

A) Three neighboring active zones (AZs) in the Ib MN stained for Brp (magenta). Scale bar = 500 nm.

B) Activity during evoked 0.2Hz stimulation of neighboring AZs in (A) before the addition of OA.

C) Activity during evoked 0.2Hz stimulation of neighboring AZs in (A) after the addition of OA.

D) Individual ΔF/F traces for AZs shown in (A)-(C). Red bar shows addition OA (10μM) followed by a 10min incubation period. All trials below red bar are post-OA

E) P_r before and after OA for individual wildtype Ib MN AZs (n = 519 AZs from 4 NMJs). Dashed black line is y = x.

F) AZs from (E) binned by normalized Brp amounts. Left axis: number of AZs per bin. Right axis: pre-OA P_r open circles and post-OA P_r is filled circles. Vertical error bars are mean P_r ± SEM. Horizontal error bars are mean normalized Brp ± SEM. (n = 519 AZs from 4 NMJs)

Blue line in (A)–(C) is the Ib MN boundary

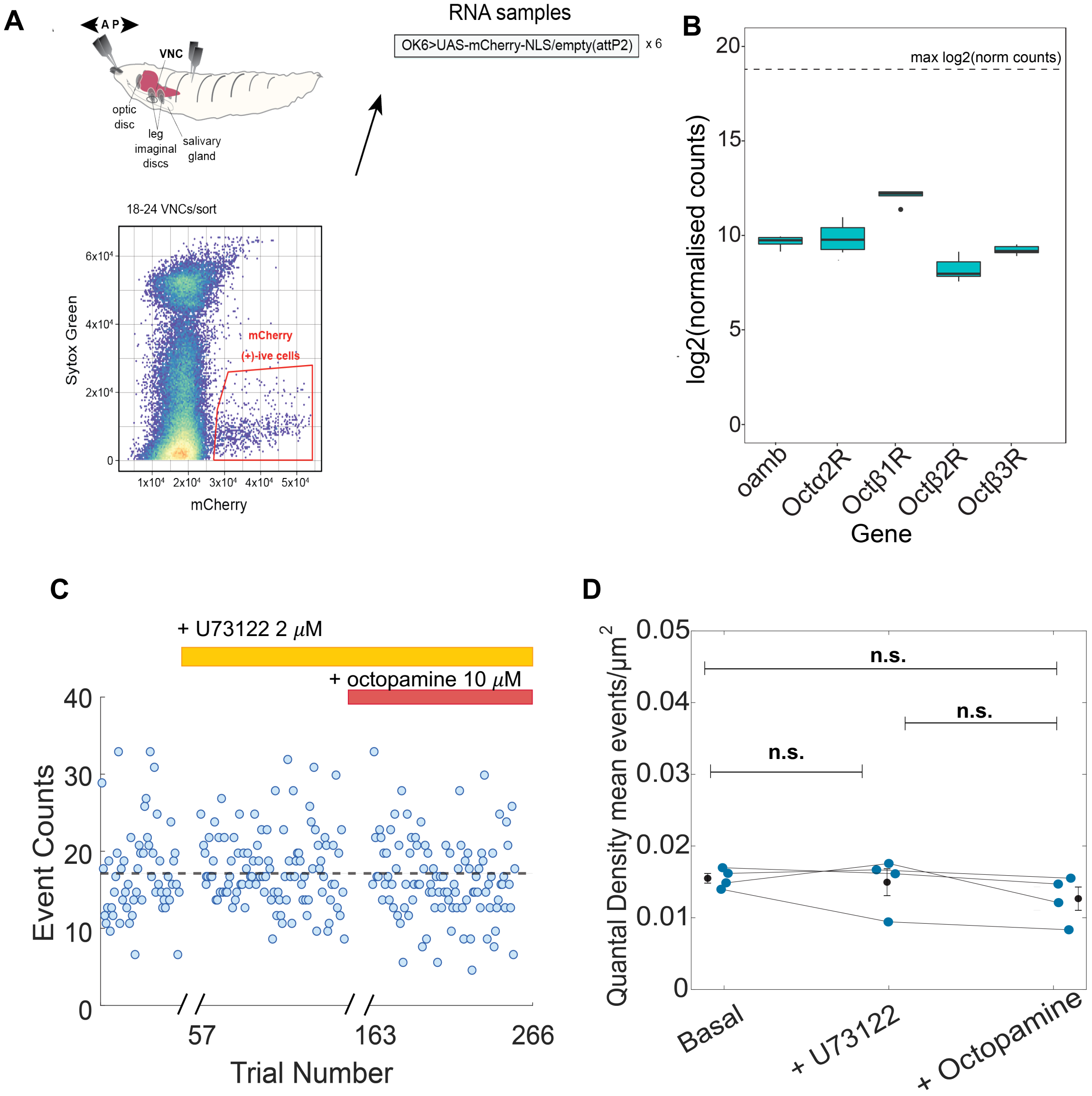

Figure 3.3. Expression of OA receptors in type I MNs. Blocking PLC blocks facilitation of release by OA.

A) Schematic showing procedure for RNA-sequencing (RNA-seq) experiment. mCherry is expressed in type I MNs which are then selected to be sequenced.

B) RNAseq data showing the normalized expression of OA receptors in type I MNs. Dashed line shows the maximum norm counts observed in attp2 controls. Error bars are mean expression ± SEM

C) Event counts per trial for a *wt* Ib MN. First break in the axis shows 10min incubation with U73122, a selective PLC inhibitor, (2 µM). Trials below the yellow bar indicate trials with PLC inhibitor. Second break in the axis shows 10min incubation with OA (10 µM). Trials under the red bar indicate trials with OA.

D) Quantal densities (mean events per trial/ μm^2) for Ib MNs (n = 4 *wt* NMJs) incubated with U73122 (2 µM) followed by addition of OA (10 µM). Points in black with error bars mean QDs ± SEM. (n.s., not significant by Student's paired t-test)

(A)-(B) by Caroline Cypranowska

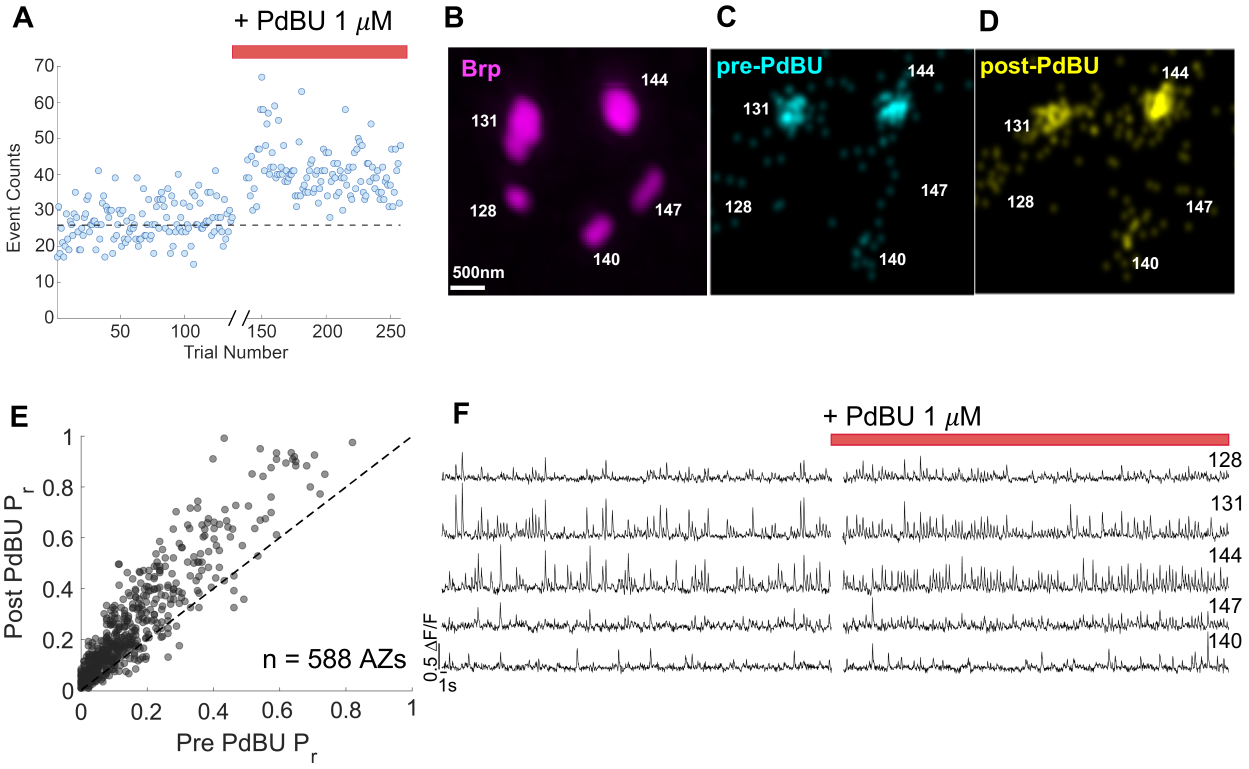

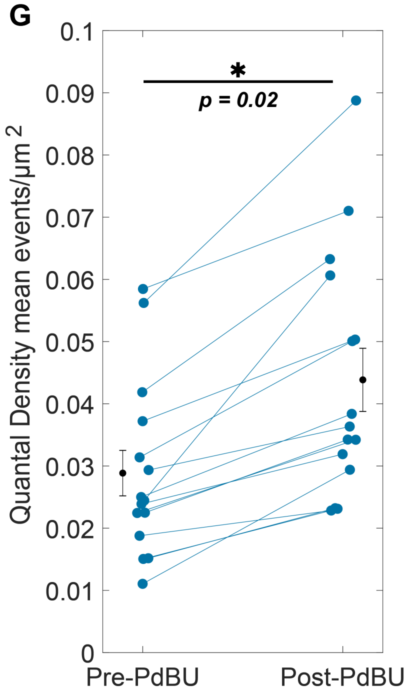

Figure 3.4. Acute application of PdBU increases the number of events across Ib MNs but affects each synapse differently.
A) Event counts per trial for Ib MN in a *wt* NMJ. Break in the axis shows 6 min incubation with PdBU (1 μM). Trials under the red bar indicate trials with PdBU.
B) Neighboring active zones (AZs) in the Ib MN stained for Brp (magenta).
Scale bar = 500 nm
C) Activity during evoked 0.2Hz stimulation of neighboring AZs in (B) before the addition of PdBU (1 μM).
D) Activity during evoked 0.2Hz stimulation of neighboring AZs in (B) after the addition of PdBU (1 μM).
E) P_r before and after OA for individual *wt* Ib MN AZs (n = 588, from 5 NMJs). Dashed black line is y = x.
F) ΔF/F traces for AZs shown in (B)-(D). Red bar shows addition of PdBU (1 μM) followed by a 6min incubation period. All trials below red bar are post-PdBU. Vertical scale bar = 0.5 ΔF/F. Horizontal scale bar is 1s
G) Quantal densities (mean events per trial/ μm^2) for Ib MNs before and after PdBU (1 μM) (n = 15 *wt* NMJs).
Error bars on the sides in black are mean QDs ± SEM. (p = 0.02 by Student's paired t-test)

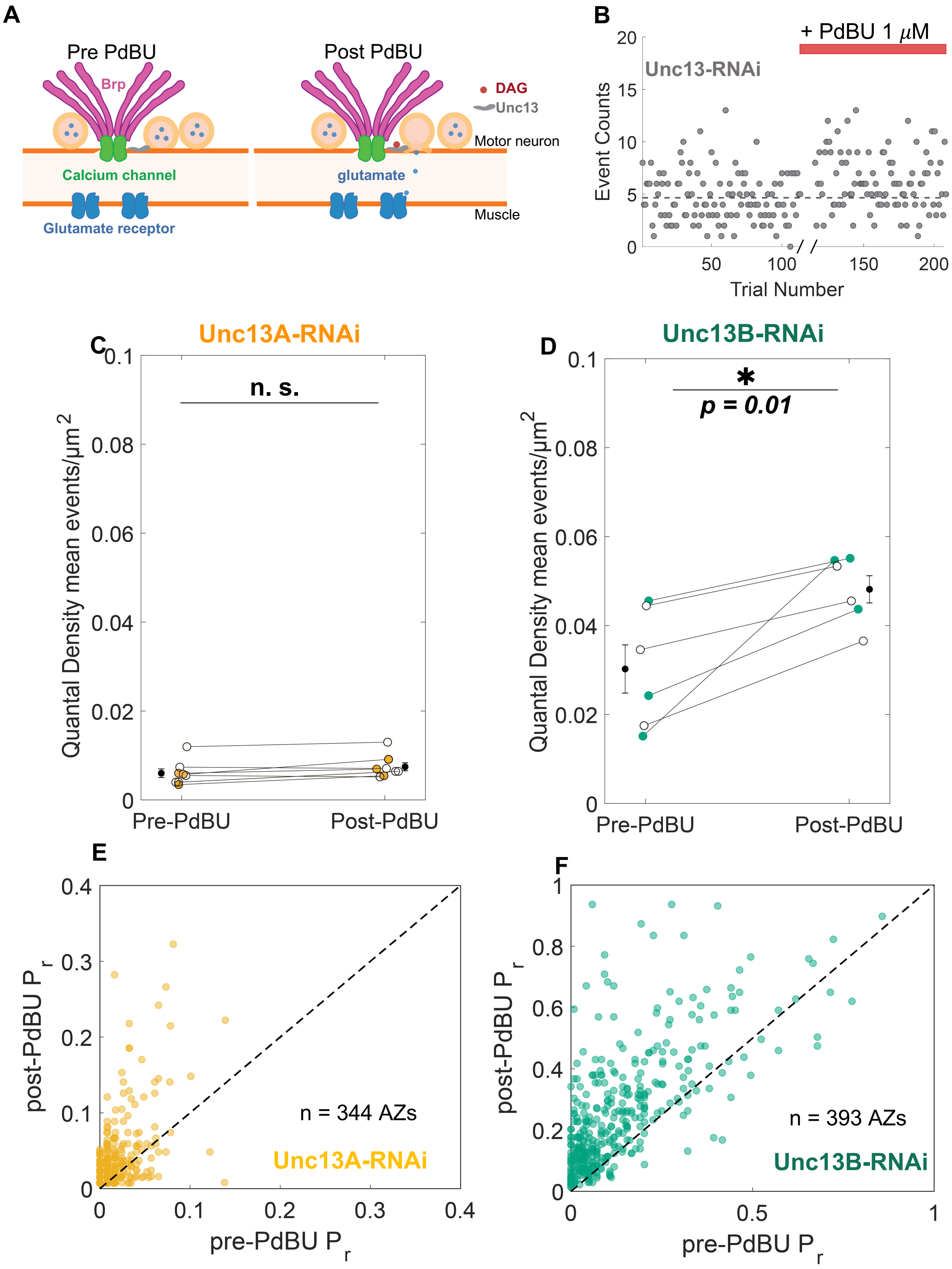
A
Pre PdBU
Post PdBU
Brp
DAG
Unc13
Motor neuron
Calcium channel
glutamate
Glutamate receptor
Muscle
B
+ PdBU 1 μM
Unc13-RNAi
Event Counts
Trial Number
0
5
10
15
20
50
100
150
200
C
Unc13A-RNAi
n. s.
Quantal Density mean events/μm2
0
0.02
0.04
0.06
0.08
0.1
Pre-PdBU
Post-PdBU
D
Unc13B-RNAi
*
p = 0.01
Quantal Density mean events/μm2
0
0.02
0.04
0.06
0.08
0.1
Pre-PdBU
Post-PdBU
E
post-PdBU P r
pre-PdBU P r
0
0.1
0.2
0.3
0.4
n = 344 AZs
Unc13A-RNAi
F
post-PdBU P r
pre-PdBU P r
0
0.2
0.4
0.6
0.8
1
0.5
n = 393 AZs
Unc13B-RNAi

Figure 3.5. **Effect of PdBU is Unc13-dependent, specifically Unc13A.**
A) Schematic depicting an Active Zone (AZ). Left is pre-PdBU (Unc13 is not bound to DAG; PdBU analog). Right is post-PdBU (Unc13 bound to DAG).
B) Event counts per trial for Ib MN in an *unc13-RNAi* animal. Break in the axis shows 6min incubation with PdBU (1 μM). Trials under the red bar indicate trials with PdBU.
C) Quantal densities (mean events per trial/ μm2) for Ib MNs in *unc13A-RNAi* animals before and after PdBU (1 μM) (n = 8 NMJs). 3 of the 8 have individual AZ analysis and are shown in (E). Error bars on the sides are mean QDs ± SEM. (n.s. is not significant by Student's paired t- test)
D) Quantal densities (mean events per trial/ μm2) for Ib MNs in *unc13B-RNAi* animals before and after PdBU (1 μM) (n = 6 NMJs). 3 of the 6 have individual AZ analysis and are shown in (E)Error bars on the sides are mean QDs ± SEM. (* $p < 0.05$ by Student's paired t-test)
E) P_r before and after PdBU for individual *unc13A-RNAi* Ib MN AZs (n = 344, from 3 NMJs). The three NMJs are filled in yellow circles from QD plot in (C). Dashed black line is y = x.
F) P_r before and after PdBU for individual *unc13B-RNAi* Ib MN AZs (n = 393, from 3 NMJs). Dashed black line is y = x. The three NMJs are filled in yellow circles from QD plot in (D). Dashed black line is y = x.

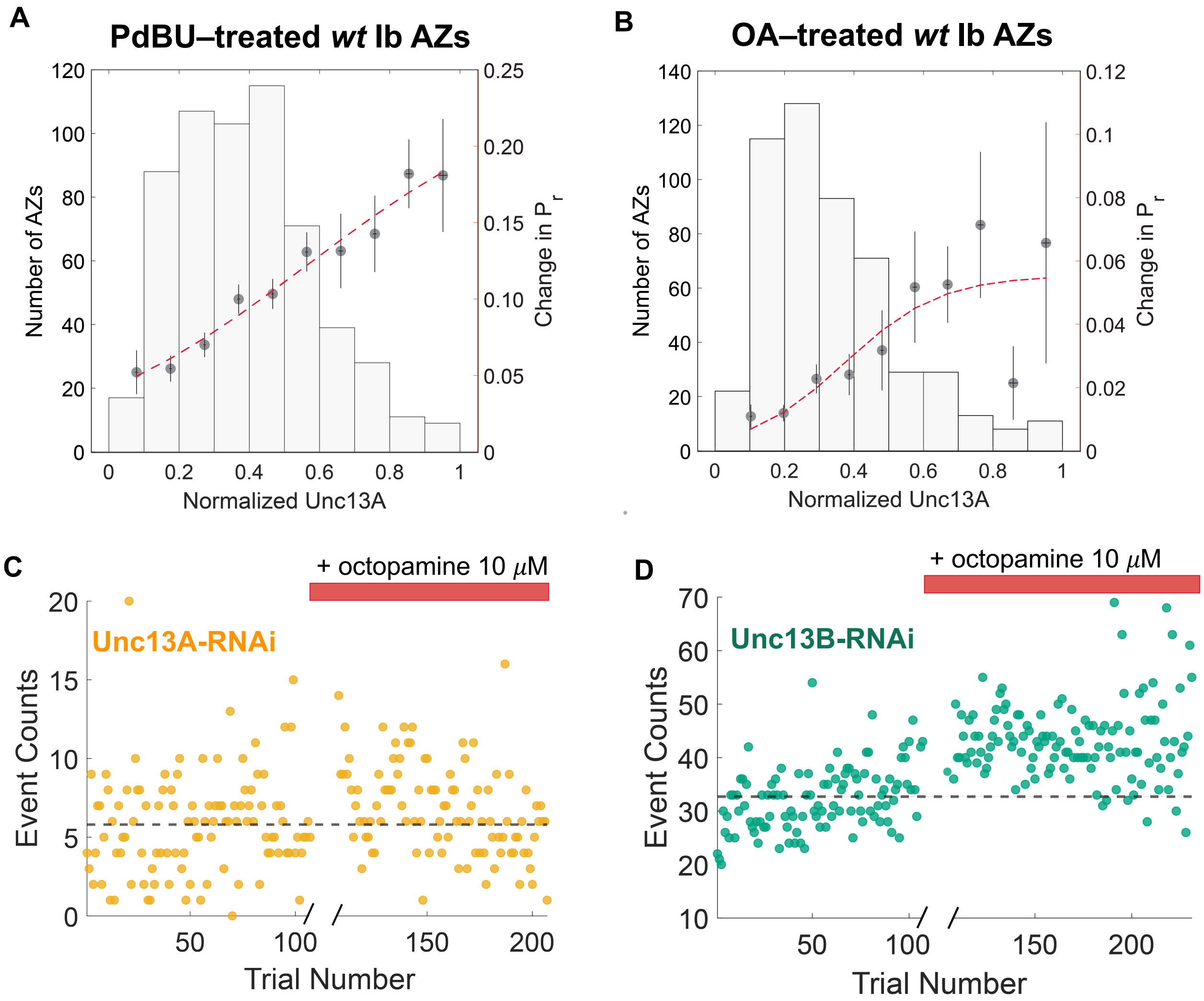

Figure 3.6. Effect of PdBU and OA depends on Unc13A amounts in *wt* type Ib MN AZs.

A) *wt* Ib MN AZs from **3.4E** binned by normalized Unc13A amounts. Left axis: number of AZs per bin. Right axis: change in P_r (post-OA P_r - pre-OA P_r) filled circles. Vertical error bars are mean P_r ± SEM. Horizontal error bars are mean normalized Unc13A ± SEM. (n = 588 AZs from 5 NMJs). Red line is sigmoidal fit: $y = 0.24/(1 + e^{-(x-0.56)*2.8})$. S.S.E. = 6.16×10^{-4}

B) *wt* Ib MN AZs from **3.2E** binned by normalized Unc13A amounts. Left axis: number of AZs per bin. Right axis: change in P_r (post-OA P_r - pre-OA P_r) filled circles. Vertical error bars are mean P_r ± SEM. Horizontal error bars are mean normalized Unc13A ± SEM. (n = 588 AZs from 5 NMJs). Red line is sigmoidal fit: $y = 0.05/(1 + e^{-(x-0.37)*7.2})$. S.S.E. = 1.7×10^{-3}

C) Raw event counts per trial for an example *unc13A-RNAi* Ib MN. Break in the axis shows addition of OA (10 μM) followed by a 10min incubation period. Red bar is the incubation period + trials with OA. Dashed black line is the mean number of events per trial before OA.

D) Raw event counts per trial for an example *unc13B-RNAi* Ib MN. Break in the axis shows addition of OA (10 μM) followed by a 10min incubation period. Red bar is the incubation period + trials with OA. Dashed black line is the mean number of events per trial before OA.

S.S.E sum of squared estimate of errors

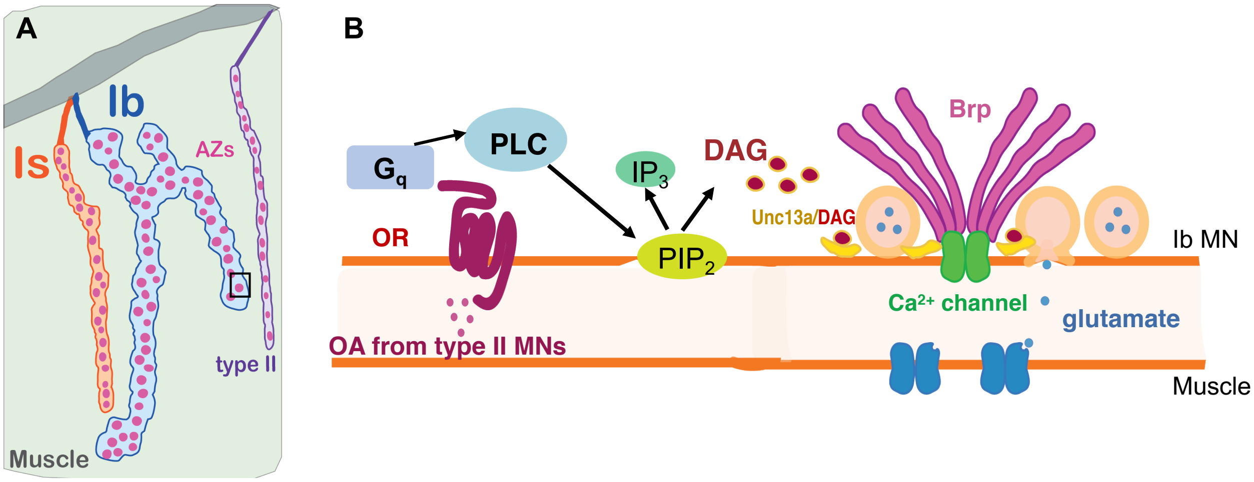

Figure 3.7. Proposed model of how octopamine(OA) affects release in type Ib MNs.

A) Schematic showing type Ib and Is MNs synapsing on the same muscle cell as a type II neuron. Both types of neurons have individual AZs shown in magenta. Black box is indicates a single AZ which is depicted in (B).

B) Side-view of a Ib MN AZ. Proposed model: OA released from type II MNs binds to an octopamine receptor (OR) which activates a G_q pathway eventually leading to more DAG at the synapse which then binds to Unc13A leading to an increased release of glutamate from the AZ.

Supplementary Figures

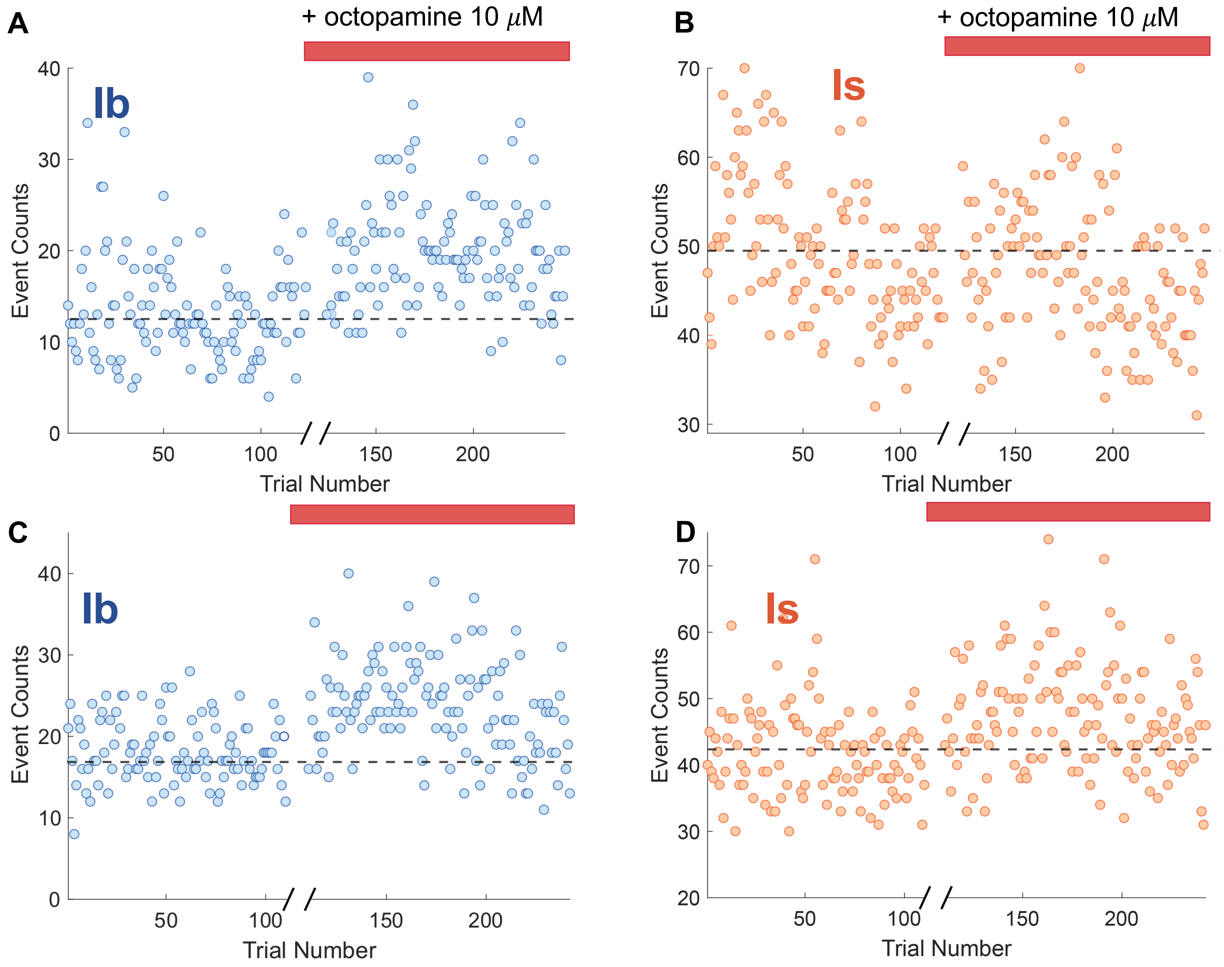

Supplementary Figure 3.1. Effect of octopamine on Ib-Is pairs, related to Figure 3.1
A) Event counts per trial for an example Ib MN. Break in the axis shows addition of octopamine (OA: 10μM) followed by a 10min incubation period. Red bar is the incubation period + trials with OA. Dashed black line is the mean number of events per trial before OA.
B) Event counts per trial for the Is of the same NMJ as in (A). Break in the axis shows addition of octopamine (OA: 10μM) followed by a 10min incubation period. Red bar is the incubation period + trials with OA. Dashed black line is the mean number of events per trial before OA.
C) Event counts per trial for another example Ib MN. Break in the axis shows addition of octopamine (OA: 10μM) followed by a 10min incubation period. Red bar is the incubation period + trials with OA. Dashed black line is the mean number of events per trial before OA.
D) Event counts per trial for the Is of the same NMJ as in (B). Break in the axis shows addition of octopamine (OA: 10μM) followed by a 10min incubation period. Red bar is the incubation period + trials with OA. Dashed black line is the mean number of events per trial before OA.

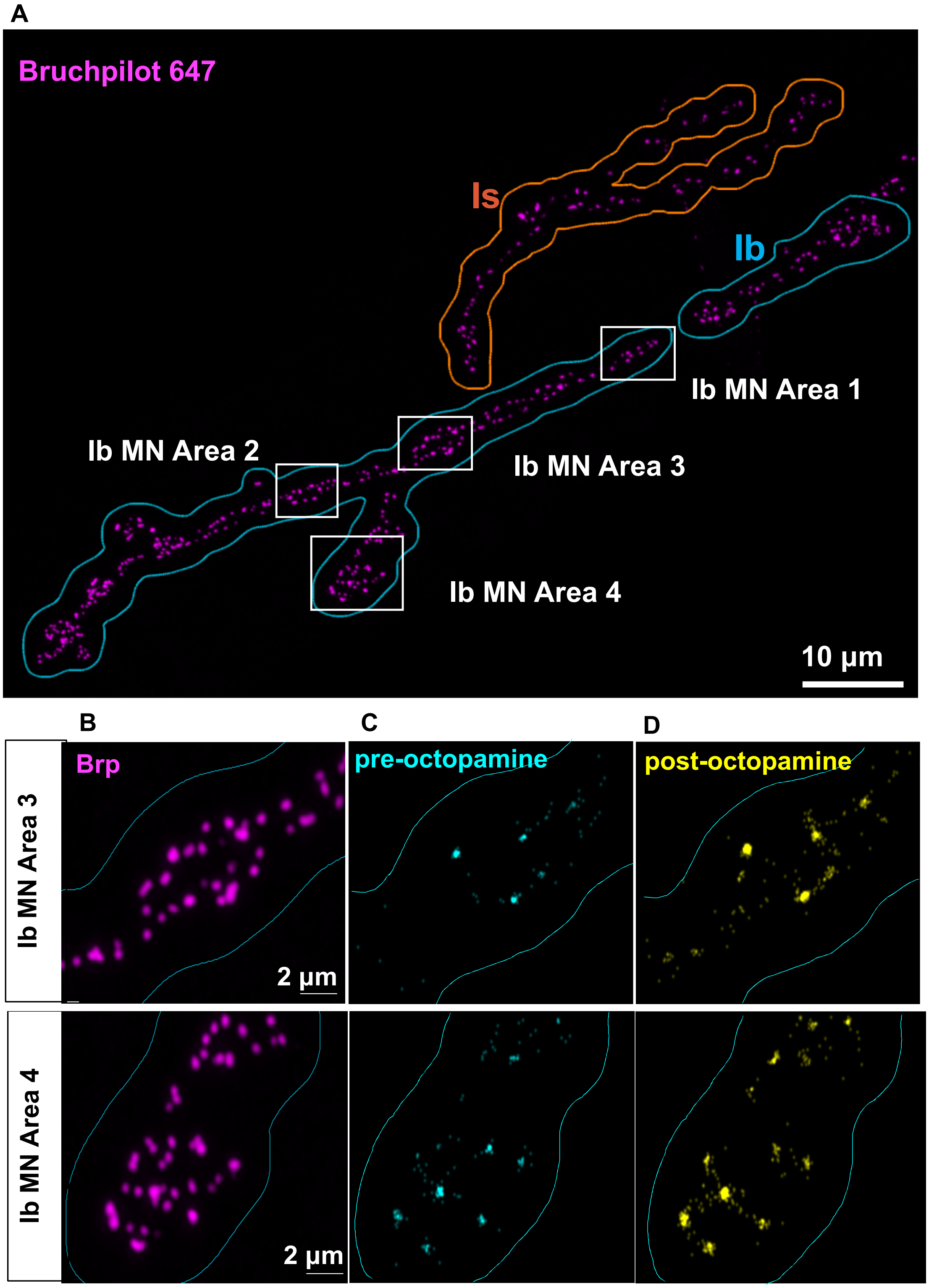
A
Bruchpilot 647
Is
Ib
Ib MN Area 1
Ib MN Area 2
Ib MN Area 3
Ib MN Area 4
10 µm
B
C
D
Brp
pre-octopamine
post-octopamine
Ib MN Area 3
2 µm
Ib MN Area 4
2 µm

Supplementary Figure 3.2 More regions showing examples of OA effect on Ib , related to Figure 3.1
A) Ib/Is pair stained for the AZ scaffolding proteins Bruchpilot (Brp). Ib MN Area 1 and 2 are shown in more detail **Fig. 3.1** (D)–(F). Ib MN Area 3 and 4 are showin in greater detail in (B)–(C) of this figure. Blue outline is the Ib MN boundary. Orange outline is the Is MN boundary. Scale bar = 10 μm.
B) Two example Ib boutons (top and bottom) stained for the AZ scaffolding protein Bruchpilot (Brp) shown in magenta. Every magenta cluster is an individual AZ. Scale bar = 2 μm.
C) Same boutons as in (B) before the addition of OA during 0.2Hz evoked stimulation. Every cyan cluster has a corresponding AZ shown in (D).
D) Same boutons as in (B) and (C) after the addition of OA during 0.2Hz evoked stimulation.
Blue line in (B)–(D) is the Ib MN boundary

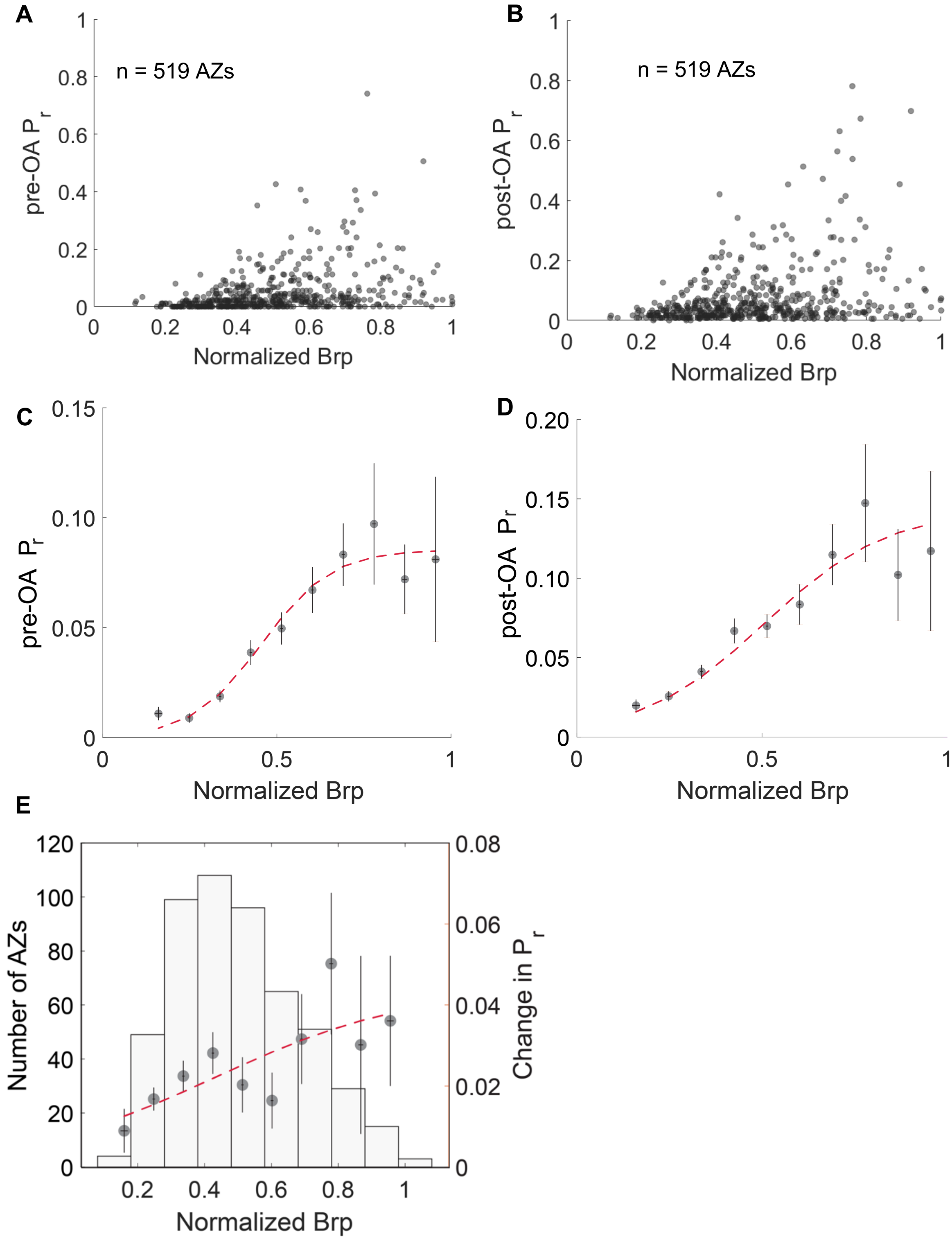
A
n = 519 AZs
pre-OA P_r
Normalized Brp
B
n = 519 AZs
post-OA P_r
Normalized Brp
C
pre-OA P_r
0.15
0.10
0.05
0
0.5
1
Normalized Brp
D
post-OA P_r
0.20
0.15
0.10
0.05
0
0.5
1
Normalized Brp
E
Number of AZs
120
100
80
60
40
20
0
Change in P_r
0.08
0.06
0.04
0.02
0
0.2
0.4
0.6
0.8
1
Normalized Brp

Supplementary Figure 3.3. Relationship of Brp to pre-, post-OA *P_r* and change in *P_r* in Ib MNs, related to 3.2

A) pre-OA P_r vs. normalized Brp amount for individual AZs, also shown in Fig 2.2. (n = 519 AZs from 4 NMJs).

B) post-OA P_r vs. normalized Brp amount for individual AZs, also shown in Fig 2.2. (n = 519 AZs from 4 NMJs)

C) pre-OA AZs from (A) sorted and binned by the normalized Brp amounts (as in **3.2F)**. Vertical error bars are mean pre-OA P_r ± SEM. Horizontal error bars are mean normalized Brp ± SEM. Red line is sigmoidal fit: $y = 0.09/(1+e^{-(x-0.46)*9.9})$. S.S.E. = 4.95×10^{-4}

D) post-OA AZs from (B) sorted and binned by the normalized Brp amounts (as in **3.2F)**. Vertical error bars are mean post-OA P_r ± SEM. Horizontal error bars are mean normalized Brp ± SEM. Red line is sigmoidal fit: $y = 0.13/(1+e^{-(x-0.44)*6.9})$. S.S.E. = 1.7×10^{-3}

E) change in P_r (post-OA P_r – pre-OA P_r) sorted and binned by normalized Brp amounts. Vertical error bars are mean change in P_r ± SEM. Horizontal error bars are mean normalized Brp ± SEM. Red line is sigmoidal fit: $y = 0.04/(1+e^{-(x-0.43)*3.4})$. S.S.E. = 5.4×10^{-4}

S.S.E sum of squared estimate of errors

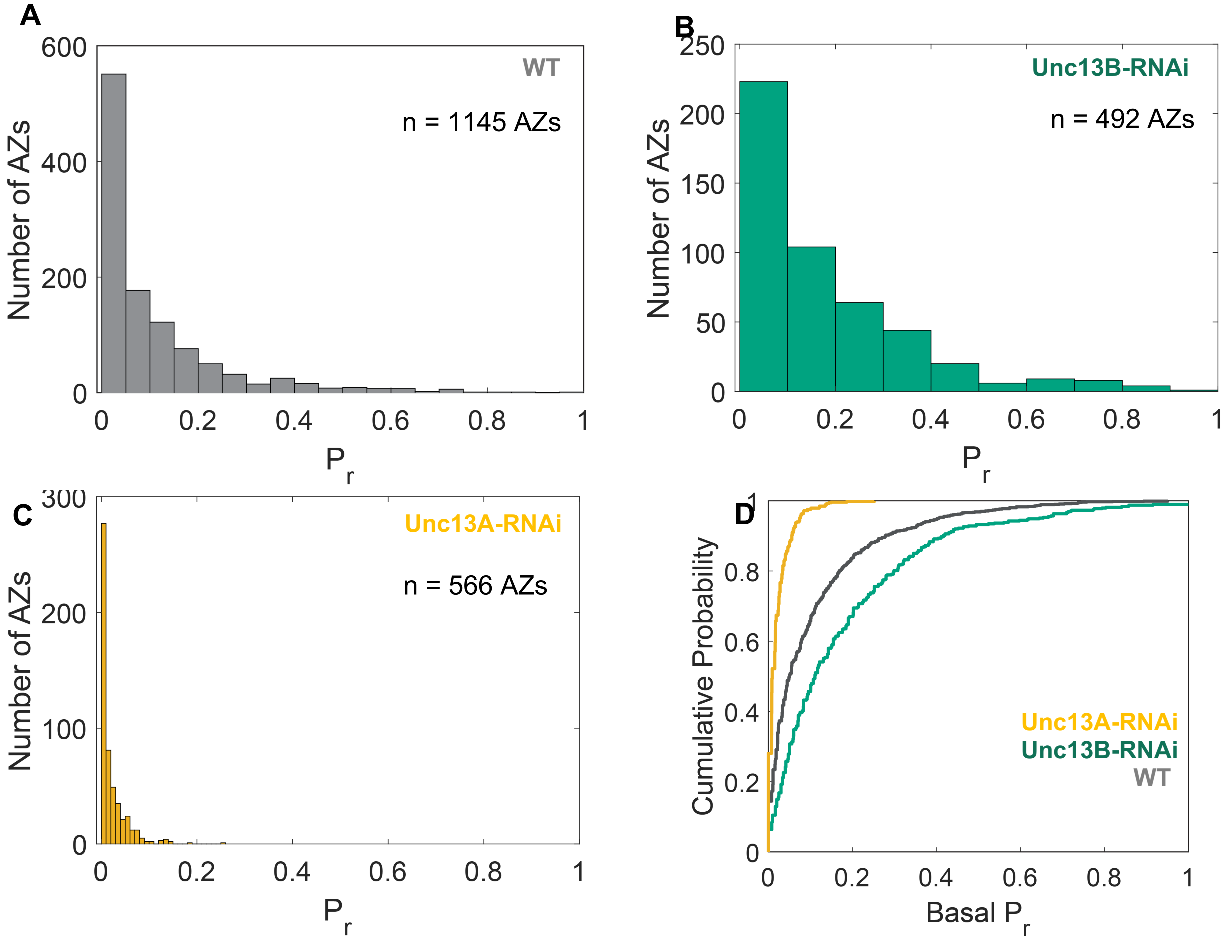

Supplementary Figure 3.4. Basal evoked P_r distributions for different genotypes in Ib MNs
A) P_r distributions for basal AP-evoked release in *wt* AZs from Ib MNs (n = 1145 AZs from 9 NMJs)
B) P_r distributions for basal AP-evoked release in *unc13B-RNAi* AZs from Ib MNs (n = 492 AZs from 4 NMJs)
C) P_r distributions for basal AP-evoked release in *unc13A-RNAi* AZs from Ib MNs (n = 566 AZs from 4 NMJs)
D) Cumulative probability of basal P_r distributions for individual Ib AZs in all genotypes. All distributions are significantly different by a two-sample Kolmogorov-Smirnov test; $p = 3.78 \times 10^{-16}$ for WT(gray) vs Unc13B-RNAi(green), $p = 9.31 \times 10^{-53}$ for WT(gray) vs Unc13A-RNAi(yellow) and $p = 4.19 \times 10^{-83}$ for Unc13B-RNAi (green) vs Unc13A-RNAi (yellow).

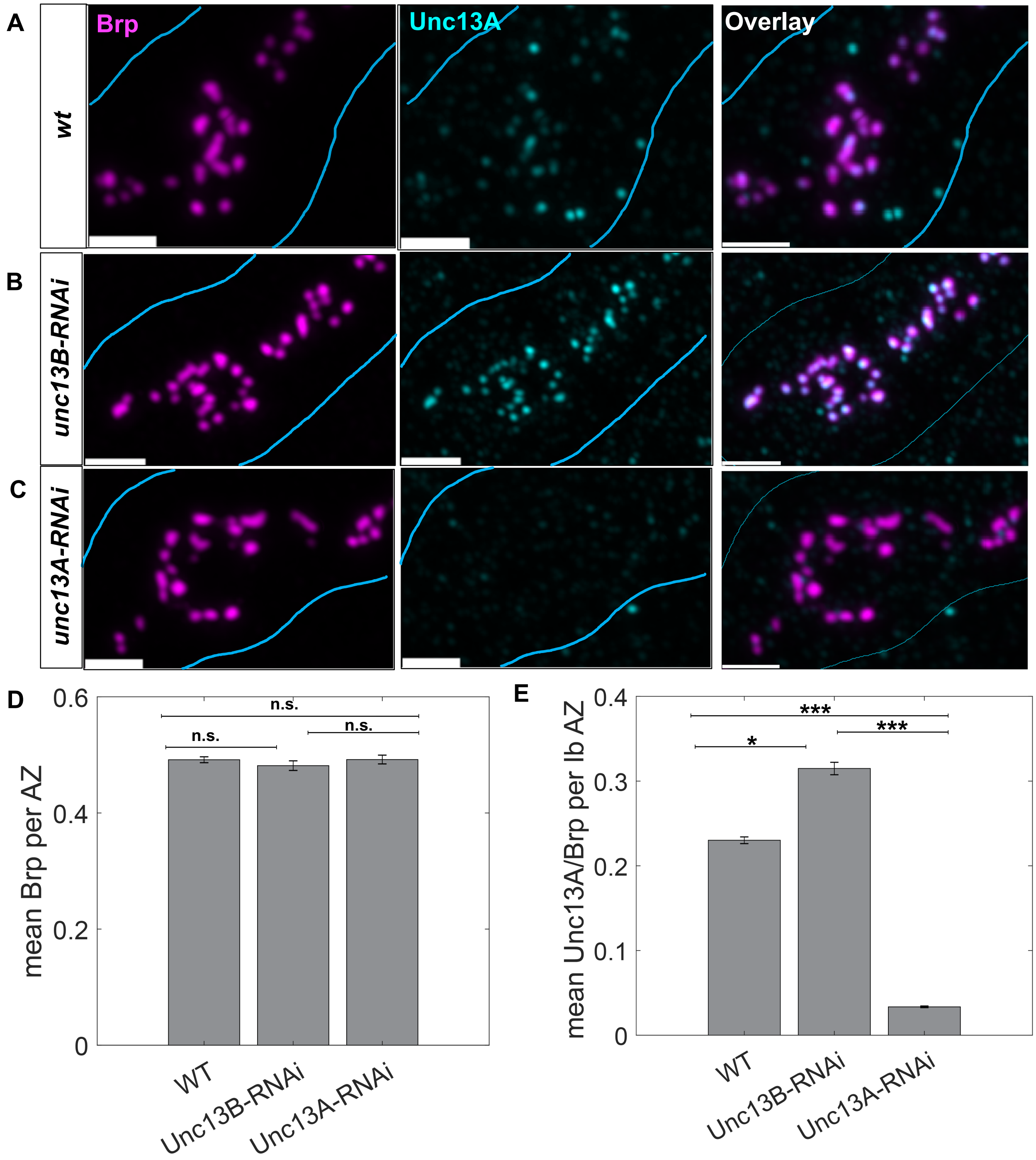

Supplementary Figure 3.5. **Airyscan confocal staining for different genotypes in Ib MNs**
A) An example bouton from a *wt* Ib MN stained for Brp (left), Unc13A (middle), and overlay (right).
B) An example bouton from an *unc13B-RNAi* Ib MN stained for Brp (left), Unc13A (middle), and overlay (right).
C) An example bouton from an *unc13A-RNAi* Ib MN stained for Brp (left), Unc13A (middle), and overlay (right).
D) Mean normalized Brp amounts per AZ in different genotypes. Error bars are mean normalized Brp ± SEM.
E) Mean Unc13A to Brp ratio per AZ in different genotypes. Error bars are mean Unc/Brp ratio ± SEM.
(* $p < 0.05$, *** $p < 0.001$, n.s. is not significant by Student's paired t-test).

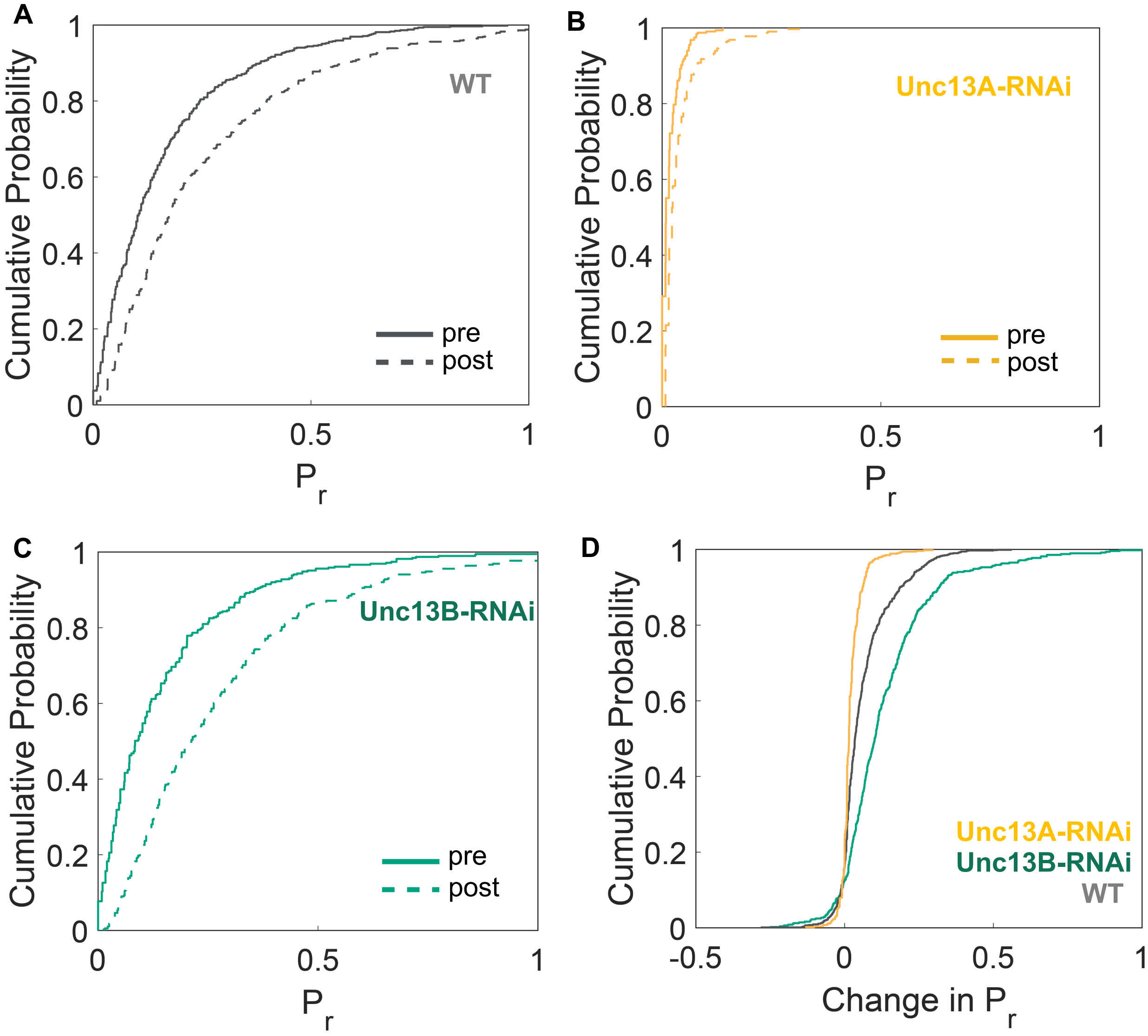

Supplementary Figure 3.6. Distributions pre and post-PdBU for all the genotypes, related to 3.4F (*wt*), 3.5E (*unc13A-RNAi*), and 3.5F(*unc13B-RNAi*)

A) Distribution of P_r before and after PdBU for individual *wt* Ib MN AZs (n = 588, from 5 NMJs,) from **Fig. 3.4F**. Significantly different by a two-sample K.S. test; $p = 3.78 \times 10^{-16}$

B) Distribution of P_r before and after PdBU for individual *unc13A-RNAi* Ib MN AZs (n = 344, from 3 NMJs) from **Fig. 3.5E**. Significantly different by a two-sample K.S. test; $p = 1.2 \times 10^{-19}$

C) Distribution of P_r before and after PdBU for individual *unc13B-RNAi* Ib MN AZs (n = 393, from 3 NMJs) from **Fig 3.5F**. Significantly different by a two sample K.S. test; $p = 3.5 \times 10^{-16}$

C) Distribution showing change in P_r (post-PdBU P_r – pre-PdBU P_r) for individual AZs from Ib MNs in different genotypes: *unc13A-RNAi* (yellow), *unc13B-RNAi* (green), *wt* (gray). All distributions different amongst each other by a two sample K.S. test. $p = 2.5 \times 10^{-4}$ for *wt* vs *unc13B-RNAi*, $p = 4.97 \times 10^{-54}$ for wt(gray) vs *unc13A-RNAi*(yellow) and $p = 5.54 \times 10^{-49}$ for *unc13B-RNAi* (green) vs *unc13A-RNAi* (yellow).

KS – Kolmogorov-Smirnov

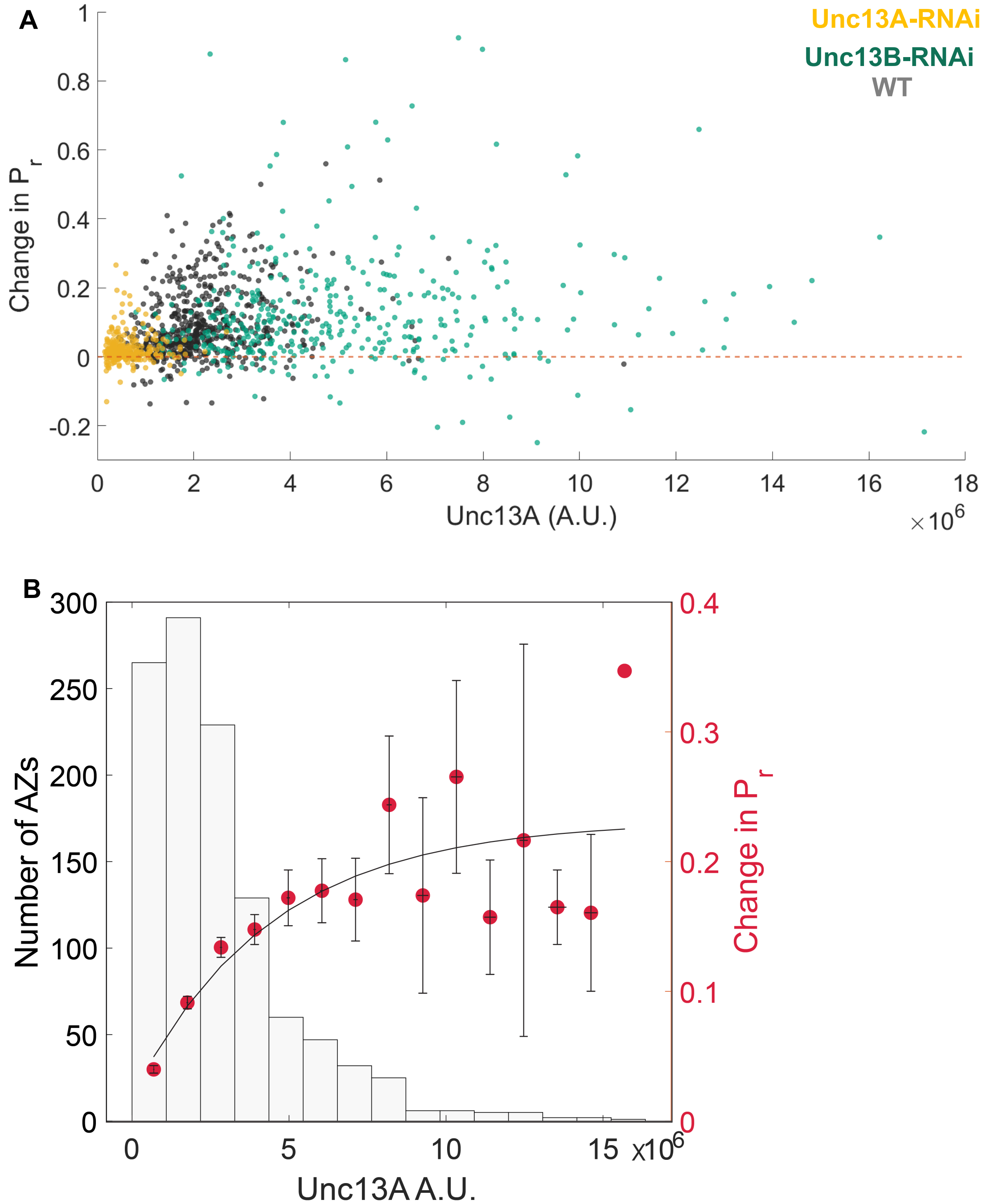

Supplementary Figure 3.7. Response of individual Ib AZs to PdBU in *wt, unc13A-RNAi* and *unc13B-RNAi*

A) Scatter showing change in P_r (post-PdBU P_r – pre-PdBU P_r) and Unc13A amounts (A.U., arbitrary units) for Individual AZs from Ib MNs in different genotypes: *unc13A-RNAi* (yellow, same AZs, *unc13B-RNAi* (green), *wt* (gray). Dashed orange line is at y = 0 and represent no change.

B) Only facilitated individual AZs from the 3 different genotypes from (A) (n = 1137 facilitated AZs from 11 NMJs (5 *wt,* 3 *unc13B-RNAi*, 3 *unc13A-RNAi* NMJs) binned by their Unc13A amounts at the synapse. Left axis: number of AZs per bin. Right axis: change in P_r (post-PdBU P_r - pre-OA P_r) filled circles. Vertical error bars are mean P_r ± SEM. Horizontal error bars are mean normalized Unc13A ± SEM. (n = 588 AZs from 5 NMJs). Red line is an exponential fit: $y = (0.21 * (1 + e^{-(x-2.2*10^{-7})})$+0.01). S.S.E. = 0.032
S.S.E sum of squared estimate of errors

References

1. Ranjbar-Slamloo Y, Fazlali Z. Dopamine and Noradrenaline in the Brain; Overlapping or Dissociate Functions? *Front Mol Neurosci*. 2020;12. Accessed July 23, 2023. https://www.frontiersin.org/articles/10.3389/fnmol.2019.00334

2. O'Donnell J, Zeppenfeld D, McConnell E, Pena S, Nedergaard M. Norepinephrine: A Neuromodulator That Boosts the Function of Multiple Cell Types to Optimize CNS Performance. *Neurochem Res*. 2012;37(11):2496-2512. doi:10.1007/s11064-012-0818-x

3. Hartenstein V, Cruz L, Lovick JK, Guo M. Developmental analysis of the dopamine-containing neurons of the Drosophila brain. *J Comp Neurol*. 2017;525(2):363-379. doi:10.1002/cne.24069

4. Selcho M, Pauls D, Huser A, Stocker RF, Thum AS. Characterization of the octopaminergic and tyraminergic neurons in the central brain of Drosophila larvae. *J Comp Neurol*. 2014;522(15):3485-3500. doi:10.1002/cne.23616

5. Koon AC, Budnik V. Inhibitory Control of Synaptic and Behavioral Plasticity by Octopaminergic Signaling. *J Neurosci*. 2012;32(18):6312-6322. doi:10.1523/JNEUROSCI.6517-11.2012

6. Zhou C, Huang H, Kim SM, et al. Molecular Genetic Analysis of Sexual Rejection: Roles of Octopamine and Its Receptor OAMB in Drosophila Courtship Conditioning. *J Neurosci*. 2012;32(41):14281-14287. doi:10.1523/JNEUROSCI.0517-12.2012

7. Crocker A, Sehgal A. Octopamine Regulates Sleep in Drosophila through Protein Kinase A-Dependent Mechanisms. *J Neurosci*. 2008;28(38):9377-9385. doi:10.1523/JNEUROSCI.3072-08a.2008

8. Sabandal JM, Sabandal PR, Kim YC, Han KA. Concerted Actions of Octopamine and Dopamine Receptors Drive Olfactory Learning. *J Neurosci*. 2020;40(21):4240-4250. doi:10.1523/JNEUROSCI.1756-19.2020

9. Schroll C, Riemensperger T, Bucher D, et al. Light-Induced Activation of Distinct Modulatory Neurons Triggers Appetitive or Aversive Learning in Drosophila Larvae. *Curr Biol*. 2006;16(17):1741-1747. doi:10.1016/j.cub.2006.07.023

10. Cheng KY, Frye MA. Neuromodulation of insect motion vision. *J Comp Physiol A*. 2020;206(2):125-137. doi:10.1007/s00359-019-01383-9

11. Ruiz-Cañada C, Budnik V. Introduction on The Use of The Drosophila Embryonic/Larval Neuromuscular Junction as A Model System to Study Synapse Development and Function, and A Brief Summary of Pathfinding and Target Recognition. In: *International Review of Neurobiology*. Vol 75. The Fly Neuromuscular Junction: Structure and Function Second Edition. Academic Press; 2006:1-31. doi:10.1016/S0074-7742(06)75001-2

12. Ormerod KG, Hadden JK, Deady LD, Mercier AJ, Krans JL. Action of octopamine and tyramine on muscles of Drosophila melanogaster larvae. *J Neurophysiol*. 2013;110(8):1984-1996. doi:10.1152/jn.00431.2013

13. Steinert JR, Kuromi H, Hellwig A, et al. Experience-Dependent Formation and Recruitment of Large Vesicles from Reserve Pool. *Neuron*. 2006;50(5):723-733. doi:10.1016/j.neuron.2006.04.025

14. Koon AC, Ashley J, Barria R, et al. Autoregulatory and paracrine control of synaptic and behavioral plasticity by octopaminergic signaling. *Nat Neurosci*. 2011;14(2):190-199. doi:10.1038/nn.2716

15. Rao S, Lang C, Levitan ES, Deitcher DL. Visualization of neuropeptide expression, transport, and exocytosis in Drosophila melanogaster. *J Neurobiol*. 2001;49(3):159-172. doi:10.1002/neu.1072

16. Ding K, Han Y, Seid TW, et al. Imaging neuropeptide release at synapses with a genetically engineered reporter. Griffith LC, Marder E, Griffith LC, Taghert P, eds. *eLife*. 2019;8:e46421. doi:10.7554/eLife.46421

17. Atwood HL, Govind CK, Wu CF. Differential ultrastructure of synaptic terminals on ventral longitudinal abdominal muscles inDrosophila larvae. *J Neurobiol*. 1993;24(8):1008-1024. doi:10.1002/neu.480240803

18. Stocker B, Bochow C, Damrau C, et al. Structural and Molecular Properties of Insect Type II Motor Axon Terminals. *Front Syst Neurosci*. 2018;12:5. doi:10.3389/fnsys.2018.00005

19. Newman ZL, Hoagland A, Aghi K, et al. Input-Specific Plasticity and Homeostasis at the Drosophila Larval Neuromuscular Junction. *Neuron*. 2017;93(6):1388-1404.e10. doi:10.1016/j.neuron.2017.02.028

20. Newman ZL, Bakshinskaya D, Schultz R, et al. Determinants of synapse diversity revealed by super-resolution quantal transmission and active zone imaging. *Nat Commun*. 2022;13(1):229. doi:10.1038/s41467-021-27815-2

21. Peled ES, Newman ZL, Isacoff EY. Evoked and Spontaneous Transmission Favored by Distinct Sets of Synapses. *Curr Biol*. 2014;24(5):484-493. doi:10.1016/j.cub.2014.01.022

22. Peled ES, Isacoff EY. Optical quantal analysis of synaptic transmission in wild-type and rab3-mutant Drosophila motor axons. *Nat Neurosci*. 2011;14(4):519-526. doi:10.1038/nn.2767

23. Frank CA, Wang X, Collins CA, et al. New Approaches for Studying Synaptic Development, Function, and Plasticity Using *Drosophila* as a Model System. *J Neurosci*. 2013;33(45):17560-17568. doi:10.1523/JNEUROSCI.3261-13.2013

24. Balfanz S, Strünker T, Frings S, Baumann A. A family of octapamine receptors that specifically induce cyclic AMP production or Ca2+ release in Drosophila melanogaster. *J Neurochem*. 2005;93(2):440-451. doi:10.1111/j.1471-4159.2005.03034.x

25. Qi Y xiang, Xu G, Gu G xiang, et al. A new Drosophila octopamine receptor responds to serotonin. *Insect Biochem Mol Biol*. 2017;90:61-70. doi:10.1016/j.ibmb.2017.09.010

26. Maqueira B, Chatwin H, Evans PD. Identification and characterization of a novel family of Drosophilaβ-adrenergic-like octopamine G-protein coupled receptors: Insect β-adrenergic-

like octopamine receptors. *J Neurochem*. 2005;94(2):547-560. doi:10.1111/j.1471-4159.2005.03251.x

27. James TD, Zwiefelhofer DJ, Frank CA. Maintenance of homeostatic plasticity at the Drosophila neuromuscular synapse requires continuous IP3-directed signaling. VijayRaghavan K, ed. *eLife*. 2019;8:e39643. doi:10.7554/eLife.39643
28. Rhee JS, Betz A, Pyott S, Reim K, Varoqueaux F, Augustin I. Phorbol Ester- and Diacylglycerol-Induced Augmentation of Transmitter Release Is Mediated by Munc13s and Not by PKCs.
29. Lou X, Scheuss V, Schneggenburger R. Allosteric modulation of the presynaptic Ca2+ sensor for vesicle fusion. *Nature*. 2005;435(7041):497-501. doi:10.1038/nature03568
30. Palfreyman MT, Jorgensen EM. Unc13 Aligns SNAREs and Superprimes Synaptic Vesicles. *Neuron*. 2017;95(3):473-475. doi:10.1016/j.neuron.2017.07.017
31. Böhme MA, Beis C, Reddy-Alla S, et al. Active zone scaffolds differentially accumulate Unc13 isoforms to tune Ca2+ channel–vesicle coupling. *Nat Neurosci*. 2016;19(10):1311-1320. doi:10.1038/nn.4364
32. Reddy-Alla S, Böhme MA, Reynolds E, et al. Stable Positioning of Unc13 Restricts Synaptic Vesicle Fusion to Defined Release Sites to Promote Synchronous Neurotransmission. *Neuron*. 2017;95(6):1350-1364.e12. doi:10.1016/j.neuron.2017.08.016
33. Basu J, Betz A, Brose N, Rosenmund C. Munc13-1 C1 Domain Activation Lowers the Energy Barrier for Synaptic Vesicle Fusion. *J Neurosci*. 2007;27(5):1200-1210. doi:10.1523/JNEUROSCI.4908-06.2007
34. Lee JS, Ho WK, Neher E, Lee SH. Superpriming of synaptic vesicles after their recruitment to the readily releasable pool. *Proc Natl Acad Sci*. 2013;110(37):15079-15084. doi:10.1073/pnas.1314427110
35. Guizar-Sicairos M, Thurman ST, Fienup JR. Efficient subpixel image registration algorithms. *Opt Lett*. 2008;33(2):156. doi:10.1364/OL.33.000156
36. Vercauteren T, Pennec X, Perchant A, Ayache N. Diffeomorphic demons: Efficient non-parametric image registration. *NeuroImage*. 2009;45(1, Supplement 1):S61-S72. doi:10.1016/j.neuroimage.2008.10.040
37. Preibisch S, Saalfeld S, Tomancak P. Globally optimal stitching of tiled 3D microscopic image acquisitions. *Bioinformatics*. 2009;25(11):1463-1465. doi:10.1093/bioinformatics/btp184
38. Hahne F, LeMeur N, Brinkman RR, et al. flowCore: a Bioconductor package for high throughput flow cytometry. *BMC Bioinformatics*. 2009;10(1):1-8. doi:10.1186/1471-2105-10-106
39. Van P, Jiang W, Gottardo R, Finak G. ggCyto: next generation open-source visualization software for cytometry. *Bioinformatics*. 2018;34(22):3951-3953. doi:10.1093/bioinformatics/bty441

40. Kapteyn J, He R, McDowell ET, Gang DR. Incorporation of non-natural nucleotides into template-switching oligonucleotides reduces background and improves cDNA synthesis from very small RNA samples. *BMC Genomics*. 2010;11(1):413. doi:10.1186/1471-2164-11-413

41. Li H, Horns F, Wu B, et al. Classifying Drosophila Olfactory Projection Neuron Subtypes by Single-Cell RNA Sequencing. *Cell*. 2017;171(5):1206-1220.e22. doi:10.1016/j.cell.2017.10.019

42. Andrews S. FastQC: A Quality Control Tool for High Throughput Sequence Data. Published online 2010. http://www.bioinformatics.babraham.ac.uk/projects/fastqc

43. Bolger AM, Lohse M, Usadel B. Trimmomatic: a flexible trimmer for Illumina sequence data. *Bioinformatics*. 2014;30(15):2114-2120. doi:10.1093/bioinformatics/btu170

44. Kim D, Paggi JM, Park C, Bennett C, Salzberg SL. Graph-based genome alignment and genotyping with HISAT2 and HISAT-genotype. *Nat Biotechnol*. 2019;37(8):907-915. doi:10.1038/s41587-019-0201-4

45. Liao Y, Smyth GK, Shi W. featureCounts: an efficient general purpose program for assigning sequence reads to genomic features. *Bioinformatics*. 2014;30(7):923-930. doi:10.1093/bioinformatics/btt656

46. Huber W, Carey VJ, Gentleman R, et al. Orchestrating high-throughput genomic analysis with Bioconductor. *Nat Methods*. 2015;12(2):115-121. doi:10.1038/nmeth.3252

47. Love MI, Huber W, Anders S. Moderated estimation of fold change and dispersion for RNA-seq data with DESeq2. *Genome Biol*. 2014;15(12):550. doi:10.1186/s13059-014-0550-8

48. Wickham, Hadley. *Ggplot2: Elegant Graphics for Data Analysis*. Springer-Verlag; 2016. Accessed August 1, 2021. https://ggplot2.tidyverse.org/

Summary and concluding remarks

My dissertation was motivated by a central question: what underlies synaptic heterogeneity. Previous studies in our lab and others have highlighted the incredible diversity between synapses within single neurons which led us to the hypothesis that synaptic diversity is set by a very precise, local distribution of proteins. In order to determine the molecular determinants underlying synaptic heterogeneity, it's important to be able to study them from both functional and structural perspectives and at a single synapse resolution.

Chapter 2 overview and future directions

Despite making discoveries in synaptic heterogeneity using older OQA methods, we were often limited by resolution of both functional and structural methods. In Chapter 2 of this thesis work, we tackle this problem by developing a novel optical quantal analysis method called Quantal Synaptic Optical Reconstruction (QuaSOR), which through a 2D-Gaussian fitting method allowed us to improve the resolution of our previous OQA methods 5-10x (Chapter 2). Using a combination of both super-resolution structural and functional methods at the same synapses, we found that two key AZ proteins (Brp and the Ca^{2+}-channel Cacophony) varied greatly amongst synapses, correlated to P_r but accounted only for 31% of the variance in P_r. We also observed that complexin, which acts as a break on release, suppressed both spontaneous and evoked transmission but in different ways.

Even though we have now increased our spatial resolution of both function and structure, we are still limited in the temporal domain. SynapGCaMP6f, the sensor we used to develop QuaSOR has a very slow rise time (~100 ms). In result, while we are able to spatially resolve neighboring events, we can't resolve sites of release that happen at the same time. To improve the QuaSOR analysis even further, we need to use the newest version of the GCaMP sensor targeted to the synapse. In fact our lab has already developed SynapGCaMP8 variants and has found that SynapGCaMP8f allows us to distinguish events happening within 50ms of one another, which means that we can stimulate the MNs at frequencies more analogous to native behavior.

Chapter 3 overview and future directions

In chapter 3 of my dissertation I implement our super-resolution functional (QuaSOR) and structural method to investigate modulation at the synapse by the essential invertebrate neuromodulator, octopamine (OA). Surprisingly, we find that acute increase in transmission through OA is input specific. Namely, OA has an effect on Ib MN but not Is MN which synapse onto the same muscle cell (m4). We also find that this effect is at least partially due to PLC and the amount of modulation is dependent on local Unc13A amounts at the synapse.

Chapter 3 opens up a path to investigate other neuromodulators as well. In addition to OA, which is released from type II MNs at all frequencies, we know that there are neuropeptides, such as FMRFamide which are released at much higher frequencies (~40-70Hz) from type III MNs. Our RNAseq data shows that the FMRFamide receptor is present in the type I MNs (**Fig. 4.1A**). Interestingly, our preliminary data shows that FMRFmide has an effect on both type Is and type Ib MNs. In a Ib MN FMRFamide increased events/trial by 87% (mean pre-FMRFamide = 13.5 ± 0.4 events/trial, mean post-FMRFamide = 25.4 ± 1.2 events/trial) (**Fig 4.1B**). In the Is MN of the same pair, the effect of FMRFamide was a 47% increase in events/trial (mean pre-FMRFamide = 18.9 ± 0.3 events/trial, mean post-FMRFamide = 27.8 ± 0.5 events/trial) (**Fig 4.1C**).

In addition to their differing modulation through OA (Chapter 3), we have previously observed that Is synapses differ from Ib synapses. For example, Is synapses have about a ~3-fold higher P_r and they don't have presynaptic homeostatic plasticity when compared to Ib synapses. Understanding what mechanism FMRFamide acts through could potentially help us further pinpoint the molecular differences between Ib and Is MN synapses.

To conclude, the combination of super-resolution functional and structural methods along with the *Drosophila* larval NMJ as a model system, allows us to ask a myriad of questions and investigate local synaptic effects, at hundreds of synapses in parallel.

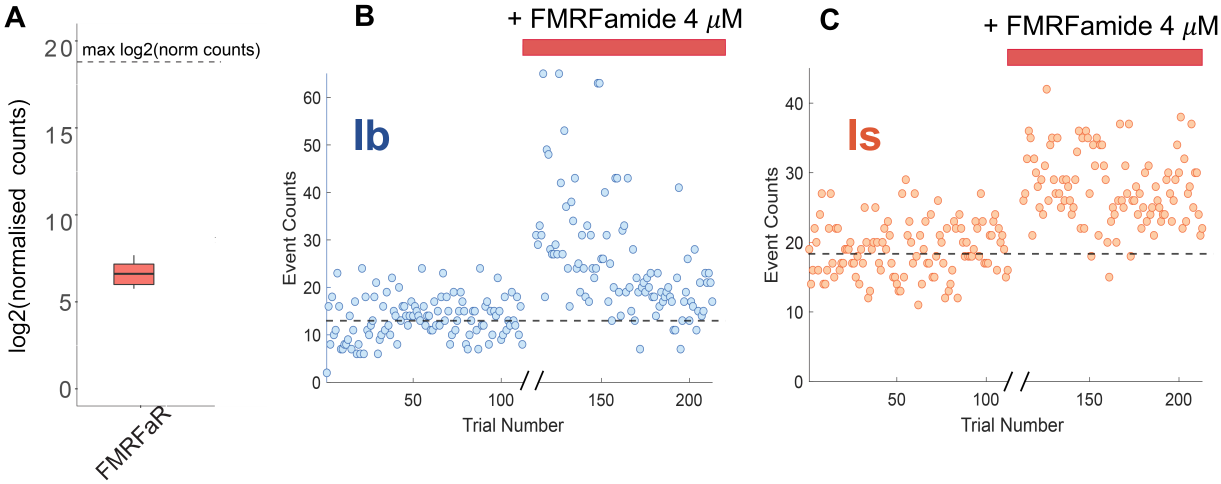

Figure 4.1. Preliminary results showing the effect of FMRFamide on Ib-Is pairs

A) RNAseq data showing the normalized expression of FMRFamide receptor in type I MNs. Dashed line shows the maximum norm counts observed in attp2 controls. Error bars are mean expression ± SEM

B) Event counts per trial for an example Ib MN. Break in the axis shows addition of FMRFamide(4 μM) followed by a 10min incubation period. Red bar is the incubation period + trials with FMRFamide. Dashed black line is the mean number of events per trial before FMRFamide

C) Event counts per trial for the Is of the same NMJ as in (A). Break in the axis shows addition of FMRFamide(4 μM) followed by a 10min incubation period. Red bar is the incubation period + trials with FMRFamide. Dashed black line is the mean number of events per trial before FMRFamide